

EDITORIAL OFFICE

EDITOR-IN-CHIEF
Malcolm J. Crocker

MANAGING EDITOR
Marek Pawelczyk

ASSOCIATE EDITORS
Dariusz Bismor
Nickolay Ivanov
Zhuang Li

ASSISTANT EDITORS
Teresa Glowka
Sebastian Kurczyk

EDITORIAL ASSISTANT
Lauren Harris

EDITORIAL BOARD

Jorge P. Arenas
Valdivia, Chile

Jonathan D. Blotter
Provo, USA

Leonid Gelman
Cranfield, UK

Samir Gerges
Florianópolis, Brazil

Victor T. Grinchenko
Kiev, Ukraine

Colin H. Hansen
Adelaide, Australia

Hanno Heller
Braunschweig, Germany

Hugh Hunt
Cambridge, England

Dan Marghitu
Auburn, USA

Manohar Lal Munjal
Bangalore, India

David E. Newland
Cambridge, England

Kazuhide Ohta
Fukuoka, Japan

Goran Pavic
Villeurbanne, France

Subhash Sinha
Auburn, USA



International Journal of Acoustics and Vibration

A quarterly publication of the International Institute of Acoustics and Vibration

Volume 19, Number 4, December 2014

EDITORIAL

Challenges in the Design of Quiet Marine Propellers

Roger Kinns 222

ARTICLES

Adaptive Resonant Vibration Control of a Piezoelectric Flexible Plate Implementing Filtered-X LMS Algorithm

Zhi-cheng Qiu and Biao Ma 224

Control of MR Damper Connected Buildings by Output Feedback

Gokarna Bahadur Motra and Naresh K. Chandiramani 240

Use of a New Modified Acoustic Model to Investigate Mean Flow Effects on Underwater Sound Sources

Mohammad Riahi, Norouz M. Nouri and Ali Valipour 252

A Note on the Influence of Intermediate Restraints and Hinges in Frequencies and Mode Shapes of Beams

Javier L. Raffo and Ricardo O. Grossi 261

Passive Vibration Isolation by Compliant Mechanism Using Topology Optimization

V. Vijayan, T. Karthikeyan, M. Udayakumar and K. Chellamuthu 269

Blind Source Separation Research Based on the Feature Distance Using Evolutionary Algorithms

Yang Yang, Xiuqin Wang and Di Zhang 276

About the Authors 287

INFORMATION

Leo Beranek's 100th Anniversary 223

Book Reviews 292



Challenges in the Design of Quiet Marine Propellers

Ship propellers have been at the forefront of acoustical design challenges for more than a century. Before aircraft dominated the passenger routes between continents, people had to be transported by ship. The factors that influence propeller noise and vibration were poorly understood and paying passengers had to be positioned a long way from intense propeller acoustical sources. The same could not be said of the crew, who had to endure noise and vibration near the stern that would nowadays be regarded as horrendous. The speeds of the fastest ocean liners, such as SS Mauretania, were over 25 knots before 1910. The faster they went, the more intense the propeller noise sources became. Ocean liners declined in numbers when air travel became affordable, only to be replaced by cruise ships and ferries of ever-increasing size. Operators now have to be concerned with ship impact on marine wildlife as well as with passengers who have reducing tolerance for noise and vibration. The acoustical design of ship propellers is again a front-line challenge.

The big problem in surface ships is cavitation, where the pressure in the flow over the rotating propeller drops below the vapour pressure of water. The propeller operates in the turbulent ship wake, so each blade experiences changes in angle of attack as it rotates and regions of cavitation wax and wane. The formation and collapse of cavitation volumes with many different length scales causes pressure fluctuations over a wide frequency spectrum, supplemented by nearly-periodic components at multiples of propeller blade passing frequency. The tip vortex usually cavitates first, because it develops in the region of highest flow speed. When it occurs, the underwater noise can increase by 5 dB or more for a one knot increase in speed. Overall noise then increases progressively with speed, with changes in the spectral shape that bias the content to lower frequencies. The maximum speed of a surface ship is often more than twice the speed at which cavitation first appears. The problem of propeller design for low cavitation noise is further complicated by the need to operate in different sea states with varying displacement, while hull fouling can itself increase the required thrust by 50% or even more.

Naval surface ships and submarines require better knowledge of the acoustical properties of propellers, since underwater radiated noise is the principal means of detection. The ability of sonar systems to detect other vessels depends critically on levels of “self-noise” which tend to be governed by the propellers over much of the speed range. The ship speed at which cavitation first occurs often imposes an upper limit on the speed at which search operations can be carried out. When a submarine is operating at depth, cavitation is suppressed by static water pressure, but that is not the end of the problem. The sound power radiated by a propeller increases rapidly with speed. The precise rate of change depends on the combination of noise generation mechanisms. Many sources are dipole-like, with frequencies proportional to speed and fluctuating force levels that are proportional to speed squared, so the sound power increases as the sixth power of speed. Other sources, such as those associated with the flow of turbulence over propeller blade trailing edges, increase at the fifth power of speed. Submarine hulls and propellers have to be designed to ensure that the intensity of those sources is controlled to match underwater noise requirements. Factors such as the propeller diameter, the number of propeller blades, the shaft speed and the radial distribution of load are all important.

Below cavitation inception, the phenomena that control ship propeller noise can be explored using aeroacoustic technology, with wind tunnels for experimental investigation. Reynolds, Mach and Strouhal numbers are key parameters. The entry flow into the propeller can be simulated in experiments, but not the free surface of the sea. It is however possible to examine the effect of the air/water interface by introducing a notional “pressure release surface” that reflects sound emanating from the propeller. This leads to so-called Lloyds Mirror effects, where the reflected sound interferes with the direct radiation below the surface of the sea.

The experimental and theoretical problems become even more demanding when cavitation is present. The cavitation number then becomes a key parameter. However the very different physical properties of air and water make it impossible to match values of Reynolds number and cavitation number at

the same time, never mind the Froude number that governs free surface effects. One of several added complications is the effect of air content on cavitation. Cavitation test facilities are expensive to build and run, but they remain essential for propeller evaluation. The flow over the complete hull and the wake field at entry to the propeller can be simulated, albeit at a reduced Reynolds number. Even a 1/20 scale model of a 300 m long ship requires a large facility, but the Reynolds number is still two orders of magnitude too low for exact scaling. The main complication is in the scaling of tip vortex cavitation, where the reduced model-scale Reynolds number causes an increase in the effects of viscosity and delays cavitation inception to higher speeds. Results are corrected to full-scale using the McCormick index, established for a given test facility by comparing model-scale predictions with full-scale results.

Close correlation between visible cavitation at model and full scale has been achieved, but another large step is required

to predict spectra of underwater noise radiation. The principal focus has been on the fluctuating pressure field on the hull surface in the frequency range up to 100 Hz at full scale, because vibration velocity in this frequency range is a key determinant of passenger comfort. Computational fluid dynamics (CFD) techniques can, in principle, be used to predict propeller noise as well as fluid flow. Progress is being made, but fundamental studies of propeller noise generation mechanisms, with and without cavitation, are still essential. Cavitation test facilities and empirical data will not be replaced easily by computer simulation.

Roger Kinns

Senior Visiting Research Fellow

School of Mechanical and Manufacturing Engineering

UNSW Australia

Leo Beranek's 100th Anniversary



The officers, directors and members of the International Institute of Acoustics (IIAV) are honored to recognize one of the giants of acoustics, noise and vibration in our time, Dr. Leo Beranek. He celebrated his 100th birthday on September 15, 2014. Leo Beranek has made so many scientific contributions that they are almost too many to count, but include numerous ones concerning psychoacoustics, community noise assessment and concert hall acoustics. An excellent summary of his contributions is provided in the Fall 2014 issue (Volume 10, Issue 4) of *Acoustics Today* published by the Acoustical Society of America. Dr. Beranek's autobiography *Riding the Waves* published in 2008 by The MIT Press and reviewed in the March 2008 issue of this journal (Volume 13, Issue 1) provides spell-binding insight into his many lifetime contributions and achievements. To recognize Dr. Beranek's contributions in acoustics, noise and vibration, Leo Beranek was named as Honorary Fellow by our Institute in the year 2000 and was given the award at the 7th International Congress on Sound and Vibration (ICSV7) in Garmisch-Partenkirchen, Germany at which he presented a special lecture.

Malcolm J. Crocker,

Executive Director, IIAV

Adaptive Resonant Vibration Control of a Piezoelectric Flexible Plate Implementing Filtered-X LMS Algorithm

Zhi-cheng Qiu and Biao Ma

School of Mechanical and Automotive Engineering, South China University of Technology, Guangzhou 510641, PR China

(Received 3 July 2013; revised: 15 November 2013; accepted: 2 December 2013)

Vibration in aerospace structures can lead to structural damage. To solve this problem, the implementation of active vibration control must be considered. This paper investigates active vibration control under the persistent resonant excitation of a clamped-clamped piezoelectric plate system. The finite element method (FEM) and ANSYS modal analysis methods are utilized to obtain the dynamics model and mode shapes of the plate. A two-norm criterion is used for optimal placement of piezoelectric sensors and actuators, taking into account the non-controlled modes to reduce spillover problems. A genetic algorithm (GA) is used to search the optimal locations of actuators/sensors. Then, a proportional derivative (PD) control algorithm and a filtered-X least mean square (filtered-X LMS) feed-forward control algorithm are designed for the system. Subsequently, numerical simulations with optimal placement of actuators and sensors are carried out to compare the performance of the controllers. Finally, experiments are conducted. The experimental results demonstrate that the designed filtered-X LMS control algorithms can suppress the resonant vibration better than that of the PD control.

1. INTRODUCTION

Flexible structures are widely used in industrial applications and aerospace structures.^{1,2} Flexible structures have the advantages of light weight and low energy consumption. Nowadays flexible space structures are developing towards the direction of large scale, flexibility, and low stiffness. However, vibration is easily caused by external disturbance due to the low stiffness and small damping of the material.^{3,4} Moreover, a dynamic aeroelastic instability phenomenon results from the interactions between motions of an aircraft panel and aerodynamic loads exerted on that panel by air flowing past one of the faces, which is called panel flutter.^{5,6} Vibration and flutter will lead to unwanted displacements, positioning errors, and even worse, lead to the destructive damage of the structure.² Especially, when the structure vibrates at its resonance frequencies, the structural working life will be greatly shortened. Therefore, active vibration control must be applied to guarantee the normal working of flexible structures.

The vibration problem has motivated a huge amount of research in the vibration control of flexible structures, and a great amount of work has been conducted in the field of smart structures by many researchers. Forward first used the piezoelectric ceramics in the vibration control of an end-supported mast.⁷ Bailey and Hubbard designed an active vibration damper for a cantilever beam using polyvinylidene fluoride (PVDF) film as a distributed-parameter actuator.⁸ An optimal control design is presented by Zhou et al. to actively suppress large-amplitude, limited-cycle flutter motions of rectangular isotropic plates at supersonic speeds using piezoelectric actuators.⁶ The results demonstrate that the piezoelectric materials show good performance in panel flutter suppression. Li used the piezoelectric material to improve the flutter characteristics of the supersonic plates.⁹ The numerical results showed that the aeroelastic flutter properties can be greatly improved by introducing active

stiffness and active mass into the supersonic plate with piezoelectric patches.

At present, researches on vibration control mainly lie in modelling methods of the mathematical model, optimal placement of actuators/sensors, and control algorithms.¹⁰⁻¹² The locations of the actuators/sensors have a significant influence on the performance of the control system. Misplaced actuators/sensors may lead to problems such as lack of observability and controllability. Researchers have used many optimization criteria and techniques to find the optimal location of actuators/sensors. Arbel first proposed the concept of controllability/observability in the optimal placement of actuators/sensors.¹³ Bruant and Proslie proposed a modified optimization criterion in consideration of the spillover effects.¹⁴ Some researchers have also suggested other optimization criterion based on H_2 or H_∞ norms.¹⁵⁻¹⁷ There are also many other optimization criterion such as the minimization of the linear quadratic regulator cost¹⁸ and the maximization of the harvested strain energy in piezoceramic materials.¹⁹ In addition, the genetic algorithm (GA) has been extensively used in finding the optimal places of the actuators/sensors.^{20,21}

There are many control algorithms utilized to suppress the vibration of flexible structures. Warminski et al. studied four types of control algorithms for the vibration suppression of a large, flexible composite beam structure.²² Shin et al. designed an acceleration feedback (AF) controller for a clamped-clamped beam.²³ Lin and Liu presented a novel resonant fuzzy logic controller (FLC) to minimize structural vibration using collocated piezoelectric actuator/sensor pairs.²⁴ The experimental results demonstrated the effectiveness of the FLC in active vibration control. Qiu et al. studied a kind of discrete-time sliding mode variable structure control (VSC) algorithm to suppress vibration of a flexible plate.²⁵ The experiments demonstrated that the proposed control algorithm is feasible

and efficient in active vibration control. Time delay exists in active control systems, instability may occur if the time delay is neglected in controller design. Kun et al. presented a theoretical and experimental study of the delayed positive feedback control technique using a flexible plate as the research object.²⁶ Tong et al. designed an H_∞ time-delay controller for a flexible plate.²⁷ The feasibility and effectiveness of the time-delay controller are demonstrated by numerical simulations and experiments. Ji et al. proposed an adaptive semi-active SSDV (Synchronized Switch Damping on Voltage) method based on the LMS algorithm and applied the algorithm to the vibration control of a composite beam.²⁸

Currently, adaptive control methods in active vibration and noise are widely used. The adaptive feed-forward control algorithm²⁹ is widely used in active resonance vibration control under persistent excitation, which was first presented by Widrow and Stearns.³⁰ A reference signal is needed in the operation process of a filtered-X LMS algorithm. Unfortunately, it is hard to get in a practical application. Model errors of the control path may lead to unstable systems or an increased signal error. However, the algorithm is particularly effective in suppressing harmonic vibration and is easy to be realized despite the above-mentioned shortcomings. Anderson and How applied the combined filtered-X LMS feed-forward and feedback control algorithm to the spacecraft vibration isolation platform.³¹ Zhu et al. used the multi-input multi-output (MIMO) filtered-U least mean square (filtered-U LMS) algorithm to control the vibration of a cantilever smart beam.³² Ma implemented a novel adaptive filtering algorithm in a cantilever beam bonded with piezoelectric patches and compared with the least mean square algorithm; satisfactory vibration reduction was achieved in different situations.³³ Carra et al. applied the filtered-X LMS algorithm in a rectangular aluminium plate vibrating in air or in contact with water.³⁴ Satisfactory reductions of the error signals were obtained in the experiments in the case of an empty tank. The control action produced lower effects while introducing water to the tank. Oh et al. presented the active vibration control of a flexible cantilever beam using one piezoceramic actuator bonded on the beam and an adaptive controller based on the filtered-X LMS algorithm.³⁵ The control results indicated that a considerable vibration reduction could be achieved in a few seconds. The performance of the filtered-X LMS algorithm for suppressing wing vibration and flutter was investigated by Carnahan and Richards.³⁶ The control method showed good performance in suppressing wing vibration and flutter.

In industrial applications, it is hard to get an accurate dynamical model of controlled systems. Both the filtered-X LMS and the filtered-U LMS control algorithms are effective in suppressing the vibration of these systems. Das et al. proposed a new virtual FXLMS algorithm for a virtual microphone.³⁷ The comparison of the FXLMS algorithm with FULMS is theoretically analysed and experimentally validated using a cantilever beam by Huang et al.³⁸ The difference between the two algorithms mainly lies in the structure of the filters. The filtered-X LMS algorithm is based on the finite impulse response (FIR) filter; while the filtered-U LMS algorithm is based on the infinite impulse response (IIR) filter. The influence on the reference signal caused by control output feedback will be reflected by poles in transfer function. Since the transfer function of the FIR filter is a full zeros expression, the FIR filter could not

eliminate the influence to the reference signal caused by control output feedback. Therefore, the FIR model is suitable for the adaptive filtering feed-forward control method. Compared with the FIR filter, the IIR filter with zeros and poles could compensate the feedback effect.

The filtered-X LMS algorithm has the merits of a high-controlling correction rate, good robustness to uncertainties, and fast speed of tracking external disturbance. Moreover, this algorithm is easy to implement with its simple structure. Therefore, it is suitable to implement the filtered-X LMS algorithm to the clamped-clamped piezoelectric plate system in this paper. However, the interference source in the filtered-X LMS is supposed to be measurable and used as the reference signal, and this is not unrealistic in some applications. As a comparison, the filtered-U LMS control algorithm is more suitable for applications in which the interference source cannot be measured directly. It has better convergence and control performance than the filtered-X LMS algorithm when feedback is present. The control performance for the clamped-clamped plate of the filtered-U LMS control algorithm will be studied in our future work for comparison with the filtered-X LMS algorithm.

This paper aims at suppressing the resonance vibration of a clamped-clamped plate under resonant sinusoidal excitation. Optimal placement of the actuators and sensors is processed based on the finite element mathematical model using an H_2 norm criterion. Then the PD controller and filtered-X LMS controller are designed. Both simulations and experiments are carried out to compare the performance of the two designed control algorithms.

The contributions of this paper are as follows: (a) the model of a piezoelectric clamped-clamped plate used to simulate panel flutter analysis is obtained by FEM. The FEM model is used for the optimization of piezoelectric sensors/actuators and simulations of control algorithms. (b) A kind of actuators/sensors optimal placement method based on the genetic algorithm is investigated. The waste time for searching the optimal positions is very short when the index of the maximal controlled modes and the index of minimal non-controlled modes are obtained. (c) Simulations and experiments are conducted to validate the effectiveness of the filtered-X LMS controller in suppressing the resonant vibration of a clamped-clamped plate under persistent excitation. A PD controller is also designed as a comparison. The results show that both the designed controllers could suppress resonant vibration effectively; the filtered-X LMS controller shows a better performance.

The rest of the paper is organized as follows. In Section 2, the finite element model of a clamped-clamped plate bonded with piezoelectric actuators and sensors is derived. In Section 3, the optimal criterion used for the placement of the actuators and sensors and the GA used for searching for a globally optimal solution are described. A numerical simulation of a clamped-clamped plate is performed. In Section 4, the filtered-X LMS control algorithm is employed. The numerical simulation results of PD control and filtered-X LMS control are provided. In Section 5, a clamped-clamped plate setup is constructed. Experiments are conducted by using the designed PD control and the filtered-X LMS control algorithms. Finally, the conclusion is drawn in Section 6.

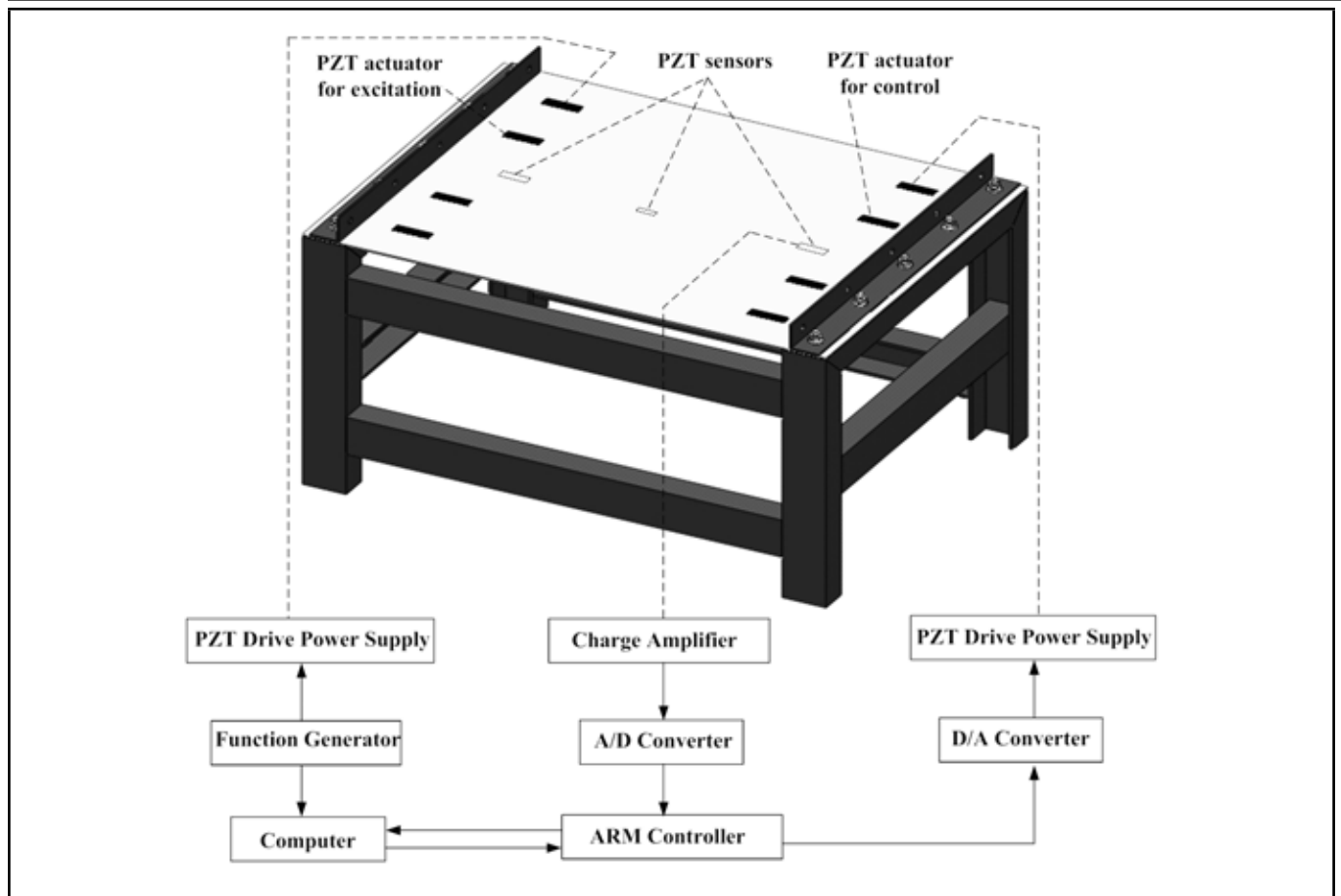


Figure 1. Three-dimensional model and schematic diagram of the system.

2. SYSTEM DESCRIPTION AND FINITE ELEMENT MODELLING

2.1. Description of a Clamped-Clamped Flexible Plate System

Figure 1 shows the three-dimensional model and the schematic diagram of the system. It should be emphasized that the PZT actuators/sensors are glued after the optimization analysis in Section 3.3. Furthermore, PZT actuators are surface-bonded symmetrically on the top and bottom surfaces of the plate. The working principle of the system can be described as follows. Firstly, the disturbance is measured by the PZT sensor in the control side. The signal from the sensor is converted into the voltage signal by using a charge amplifier. Through an A/D converter circuit, the analogue signal is transformed to the digital signal and then transferred into the ARM controller. The ARM controller will transmit the signal to the computer. By running the algorithm, the computer calculates a control output, which will be sent to the ARM controller, D/A converter, and PZT drive power supply in sequence.

A four-node rectangular element is used to build up the model of the system. The element meshing and node are numbered for the clamped-clamped plate, as shown in Fig. 2. The plate is modelled using the finite element method (FEM). It is discretized by using a four-node rectangular element based on the Kirchhoff plate theory. Each node has three degrees of freedom, corresponding to the transverse displacement w , rotation angles $\theta_x = \partial w / \partial y$ and $\theta_y = -\partial w / \partial x$.

2.2. Piezoelectric Plate Model Derived by using FEM

Since the investigated piezoelectric clamped-clamped flexible plate is excited by PZT actuators, there is no external force applied to the plate system in the present case. The element dynamics equation is

$$m\ddot{q}_e + kq_e = k_{ave} \cdot V^{ac} + k_{avc} \cdot V^{ac}; \quad (1)$$

where m is the mass matrix of a piezoelectric plate element; k is the stiffness matrix of a piezoelectric plate element; V^{ac} is the excited voltage applied to the PZT actuator used for excitation; V^{ac} is the control voltage applied to the PZT actuator used for control; k_{ave} and k_{avc} are the coefficient vectors of the internal excitation force and control force, respectively.

From the element meshing and node numbering of the clamped-clamped plate illustrated in Fig. 2, the plate is divided into 816 elements. There are 25 nodes in the length direction and 35 nodes in the width direction. Each node has three degrees of freedom. As shown in Fig. 2, the boundary condition of the plate is clamped-free-clamped-free (CFCF). By applying the boundary condition to the plate system, one should constrain all the degrees of freedom of nodes on the two edges of the plate along the Y direction, i.e., nodes from 1 to 35 and 841 to 875 are constrained.

Assembling all the plate elements and the piezoelectric elements under the consideration of the boundary condition, one can obtain the dynamics equation of the piezoelectric clamped-clamped plate as

$$M\ddot{q} + C\dot{q} + Kq = F_{AE} + F_{AC}; \quad (2)$$

3. OPTIMIZATION OF PIEZOELECTRIC SENSORS/ACTUATORS

3.1. H_2 Norm Optimal Placement Criterion

Assuming the state space representation of a system is $(\mathbf{A}, \mathbf{B}, \mathbf{C})$, when the damping ratio of the system meets the condition $\zeta \ll 1$, the norm of the i th mode can be approximately written as

$$\|G_i\|_2 = \frac{\|\mathbf{B}_i\|_2 \|\mathbf{C}_i\|_2}{2\sqrt{\zeta_i \omega_i}}; \quad (9)$$

where G_i is the transfer function of the system for the i th mode; \mathbf{B}, \mathbf{C} are equal to $\mathbf{B}_{ac}, \mathbf{C}_s$ expressed in Eq. (8).³⁹

From Eq. (9), one can conclude that the norm of the i th mode is related to its modal frequency, damping ratio, control coefficients, and sensor coefficients of the i th mode. The norm of the j th actuator for the i th mode is

$$\|G_{ij}\|_2 = \frac{\|\mathbf{B}_{ij}\|_2 \|\mathbf{C}_i\|_2}{2\sqrt{\zeta_i \omega_i}}. \quad (10)$$

Obviously, the denominator in Eq. (10) is proportional to the i th modal frequency. With the natural frequency increasing, the norms of higher modes are getting smaller and smaller compared with those of the lower modes. However, this may cause spillover problems, which are disadvantageous to the controlling of the system. Therefore, the H_2 norm can not be used as the optimization criterion directly.

Normalization processing of the H_2 norm is necessary. Normalization for the j th actuator for the i th mode is expressed as

$$\delta_{2,ij} = \frac{\|G_{ij}\|_2^2}{\max(\|G_{ij}\|_2^2)}; \quad (11)$$

where $i = 1, 2, \dots, n$; $j = 1, 2, \dots, n_s$; n_s denotes the number of actuators.¹⁵

In Eq. (11), $\delta_{2,ij}$ can be explained as: the ratio between the norm of the j th actuator and the maximum norm among all the candidate actuators for the i th mode. The optimization criterion for the j th actuator is defined as

$$\delta_{2,j} = \sum_{i=1}^n w_i \delta_{2,ij}; \quad (12)$$

where w_i is the selected weight of the i th mode.

The weight w_i can be positive or negative values. For the controlled modes, w_i is usually set as positive. The greater the weight is, the more important of the mode is. However, in order to reduce spillover problems and minimum energy for non-controlled modes, the weights should be set negative for the non-controlled modes. Therefore, the algorithm would search for a position where not only the norms of the controlled modes are high, but also the norms of the non-controlled modes are low.

3.2. Genetic Algorithm (GA)

Genetic algorithm (GA) is a stochastic optimization algorithm. It was formally presented by J. Holland in 1975.⁴⁰ Originating from Darwin's biological theory of evolution, GA combines computer science with the biological theory of evolution. The algorithm simulates the rule of survival-of-the-fittest

in nature and has the merits of global, parallelism, rapidity, and adaptability.

In view of the above-mentioned merits, GA is applied to find the optimal locations of actuators. The genetic operations of GA include selection, crossover, and mutation.²¹ Selection is an operation that chooses superior individuals from the initial population as parents of next generation. The selection operation is based on the fitness values of individuals. Those who have bigger fitness values have bigger chances to be survived.

One should know that selection only selects superior individuals but does not produce new individuals. To generate new individuals, crossover and mutation are utilized. By selecting two individuals from the current population and interchanging part of the genes from the crossover points, two new individuals are obtained. There are several crossover operations including one-point crossover, uniform crossover, and arithmetic crossover. By crossover operation, the GA can move in a desirable direction. However, the probability of a crossover should not be too big or too small. Generally, the probability of a crossover usually ranges from 0.59 to 0.99.

Selection and crossover operations complete most of the searching work of the GA. Sometimes the GA may trap in a local optimum when only selection and crossover operations are used. To prevent the GA from getting trapped in a local optimum, a mutation operation is necessary. Mutation is an operation that changes one gene of an individual according to a specific probability of mutation. Similar to the selected probability of a crossover operation, the probability of a mutation operation should also be appropriately specified. If the probability of mutation selected is bigger than 0.5, the GA will degrade to a random search method.

The coordinates of an actuator (x_j, y_j) are chosen as the optimization variables. The binary encoded method is used for GA. The length of the binary string depends on the searching scope. The following operations describe how GA works in this presentation. (a) The GA iteration firstly starts with a randomly selected population. Each individual consists of several chromosomes corresponding to the actuators. Each chromosome represents an actuator's location, and it is encoded in the binary form. In this investigation, each individual only has one chromosome. (b) Two members of the current population are selected as parents. The selected operation probability is determined by member's fitness value. Those who have bigger fitness values have a bigger chance to be selected. (c) New offsprings are generated by the crossover operation between the two selected parents. (d) In order to improve the GA's search ability, some genes of a child are changed randomly with a rate, called mutation.

The GA stops if the iteration reaches the predefined value. Generally speaking, the result obtained from a limited number of iterations may be a local optimum. Therefore, to get a result with a high confidence, one has either to run the GA process several times, each with randomly selected initial condition, or with an increasing number of iterations.

3.3. Numerical Results of Optimal Placement for Piezoelectric Patches

In this section, the optimal placement of a clamped-clamped plate is studied. The length of the plate between the two clamped edges is 600 mm; the width of the plate is 510 mm;

Table 1. Material properties of the plate and piezoelectric patch.

Symbol	Parameter	Unit	Piezoelectric patch	Plate
E	Young's modulus	GPa	63	34.64
ρ	Density	kg/m ³	7650	1840
ν	Poisson ratio	—	0.3	0.33
d_{31}	Piezoelectric strain constant	m/V	-166×10^{-12}	—

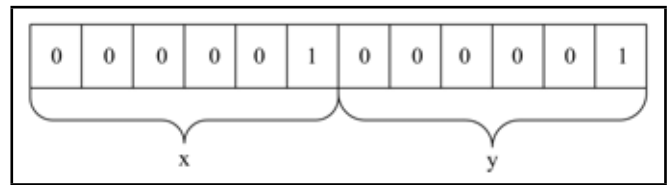


Figure 4. Typical encoding of actuator/sensor location.

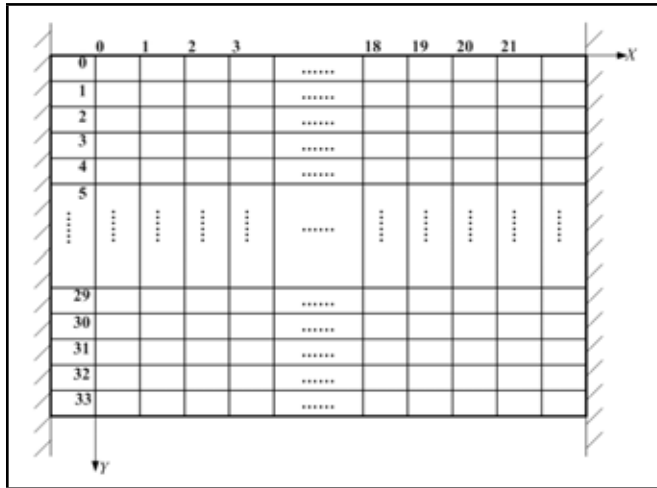


Figure 3. Coordinates used for optimal placement.

and its thickness is 2 mm. Material properties of the plate and piezoelectric patch are listed in Table 1. Three different sizes of the piezoelectric patch are employed as sensors and actuators. The size of actuators is of the same size as 50 mm×15 mm×1 mm. The sizes of sensors are 40 mm×10 mm×1 mm and 20 mm×6 mm×0.5 mm.

Since the piezoelectric patches break easily when placed in the clamped edges in practical applications, the 68 elements in the two clamped edges are not suitable to place PZT patches. When the piezoelectric patch is the same as that of the meshing element size as meshed in Fig. 2, there are 740 candidate elements that can be used to place the sensors and the actuators excluding the 68 elements in the two clamped edges. These 740 elements define the searching space for the GA. The variables are defined as the numbers of the two nodes decided by the location of a piezoelectric patch. The nodes are numbered from 0 to 21 in X direction, and numbered from 0 to 33 in Y direction, as shown in Fig. 3. Then, they are encoded in a binary string. The string length is 6 bits, i.e., the location of a piezoelectric patch is expressed by a 12 bit binary string. The first six binary strings and the rest of the binary strings correspond to the coordinate of actuator/sensor in x direction and y direction, respectively. Figure 4 shows the typical encoding of an actuator/sensor.

When the optimization criterion expressed in Eq. (12) is used, only the first three modes of vibration are considered. Only the first mode of vibration is selected as the control mode, and the other two modes as the non-controlled ones. In view of minimum energy, the weights of the non-controlled modes should be negative, while the weight of the first bending mode is positive.

In the GA operation, the parameters are selected as: the population size is 20; the probability of crossover is 0.8; the probability of mutation is set as 0.02; the maximum number of generations is 100. The genetic operation process stops at the predefined generation.

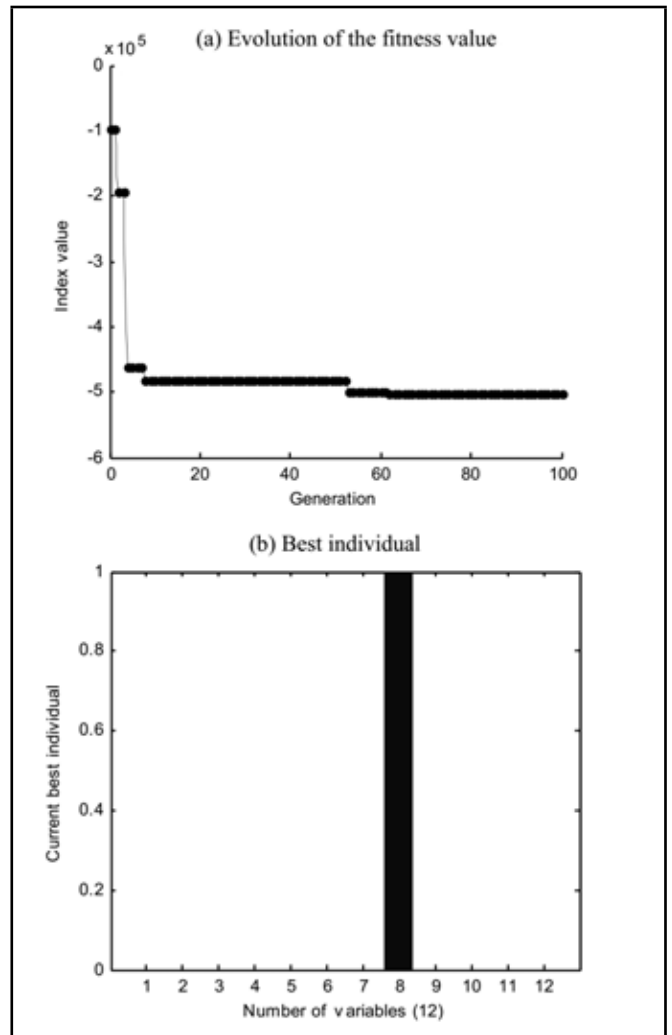


Figure 5. GA results for optimal displacement.

From Fig. 5(a), it can be seen that the performance index value converges to a constant value after 62 generations. The GA can always find the optimal solution despite the existences of suboptimal solutions. The optimal solution that the GA works out shown in Fig. 5(b) is 000000010000, i.e., the coordinates of the optimal solution are $x = 0$ and $y = 16$. Since GA only searches one optimal solution each time. By running GA for several times, one can get different optimal solutions due to the symmetry of the system.

In order to verify the validity of the GA, the enumeration method is used to calculate the performance index value of every candidate location. The results are displayed in Fig. 6. In Fig. 6, these elements that have negative performance index values are unsuitable to place the actuators. Those who have positive performance index values are more suitable to place the actuators. Moreover, the bigger the performance index value is, the more suitable the piezoelectric actuator can be

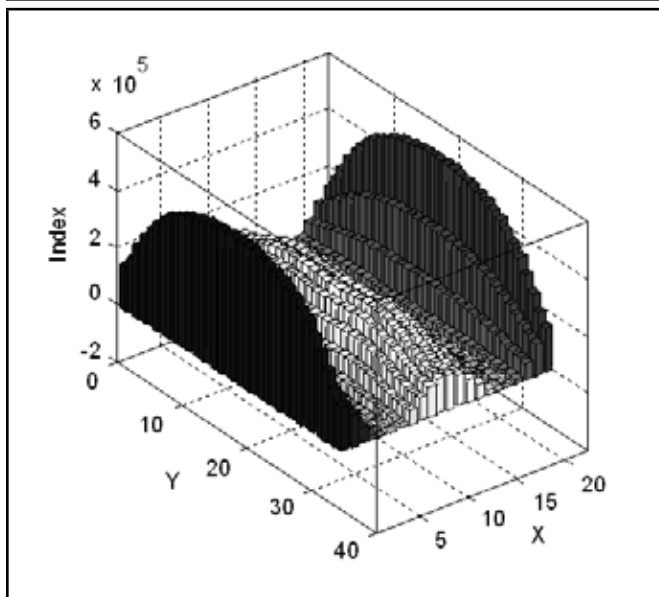


Figure 6. Performance index values using the enumeration method.

bonded. Obviously, the roots of the clamped-clamped plate in X direction have bigger performance index values, and these values that near the middle of Y direction are almost the same. However, the numbers of the elements with the best indices values are located in 51, 52, 765, and 766.

By comparing the optimal solution in the GA with the values in Fig. 6, it can be seen that the two methods get the same optimization result. Although there are many suboptimal solutions in this system, the GA still finds the optimal location of the piezoelectric patch effectively. Furthermore, the GA can easily get global optimization results while solving complex problems in comparison with other optimization techniques.

There are some points that need to be emphasized to guarantee the robustness of the GA used to search the optimal locations of actuators/sensors. The GA has good robustness for solving global optimal problems commonly, while in solving complex optimization problems, both early maturity and poor stability may occur in the GA. The GA is likely to converge to a local optimum in the case of an inappropriate fitness function. Here, the fitness function is the same as that of equation of Eq. (12) to achieve the global optimum quickly. The number of the initial population is also very important. If the initial population selected is too big, the GA will take a lot of time to get the global optimum; otherwise if the initial population is too small, the algorithm is likely to ignore the global optimum. To meet this condition, the initial population size is set as 20 in this section.

For any specific optimization problems, the GA may converge much faster with the appropriate parameters. These parameters include the crossover rate and the mutation rate. Too big of a mutation rate will lead to the loss of the optimal solution, and too small of a mutation rate can cause premature convergence to the local optimal point. For the selection of these parameters, there are no practical limits. The crossover rate is set as 0.8, and the mutation rate is set as 0.02, in this case. With the appropriate crossover rate and mutation rate, the GA can always converge to the global optimum in this section.

The piezoelectric patches should be placed at the roots of the two clamped edges in the length direction and close to the

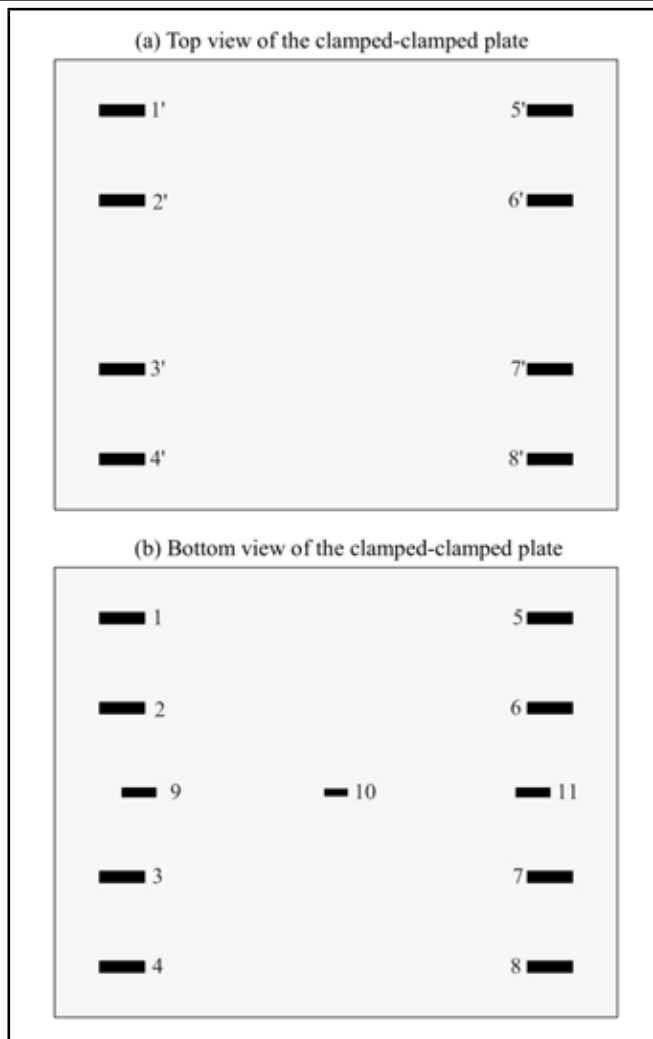


Figure 7. Top and bottom view of the clamped-clamped plate system.

middle in the width direction. Except for the optimal position, the middle of the clamped-clamped plate in X direction is the suboptimal position for bonding piezoelectric patches. Figure 7(a) and Fig. 7(b) show the top view and the bottom view of the clamped-clamped plate system, respectively.

As shown in Fig. 7, one edge of the clamped end is used as the primary exciter, and the other is used for control. Actuators 1–4 and 1’–4’ are connected in parallel as a one-channel piezoelectric actuator is used as the excited actuator to excite the vibration of the flexible plate. Actuators 5–8 and 5’–8’ in the right clamped edge are connected in parallel as a one-channel piezoelectric actuator is used as the control actuator to suppress the excited vibration. Meanwhile, signals of the top and bottom actuators are reversed-phase connected to get a bigger control force or excitation force. Also, the two different sizes of sensors are placed in the plate. Sensors 9–11 are only bonded on the bottom surface. Sensors 9 and 11 are of the dimension $40\text{ mm} \times 10\text{ mm} \times 1\text{ mm}$. The dimension of sensor 10 is $20\text{ mm} \times 6\text{ mm} \times 0.5\text{ mm}$. In this investigation, only the sensor 11 in the control end is used.

To simplify the building of the model, only the $50\text{ mm} \times 15\text{ mm} \times 1\text{ mm}$ piezoelectric patch is used in the finite element method. Since the element meshing size shown in Fig. 2 is $25\text{ mm} \times 15\text{ mm}$, the piezoelectric patches are placed in two elements side-by-side in length and direction, and they occupy one element in the width direction. When bonding the

Table 2. Comparison of the first four modal frequencies with PZT patches.

Order	Frequencies (Hz) (MATLAB)	Frequencies (Hz) (ANSYS)	Relative Error
1	25.9038	25.710	0.754%
2	32.5087	32.371	0.425%
3	60.0309	59.462	0.957%
4	71.1375	71.006	0.185%

PZT patches, modal frequencies of the flexible plate system may be changed slightly. Therefore, the modal analysis and the modal frequencies calculation for the flexible plate with the PZT patches are performed.

The model of the clamped-clamped plate is built by using a calculated program. When the commercial ANSYS software is applied to build the model, the SHELL 63 element is used to build the plate element, and the three dimensional SOLID45 element is used to build the piezoelectric element. The calculated natural frequencies of the first four modes of the plate with bonded PZT patches are listed in Table 2, respectively, by using program calculation and ANSYS software. There are many factors such as the differences of the mesh dividing method and element types used for PZT patches between the two methods; the relative errors of a plate with PZT patches is bigger than a plate without PZT patches. However, the relative errors are less than 1%.

The comparison results indicate that the relative errors between the two analysis methods are rather small. Therefore, the fidelity of the obtained model by finite element calculation is accurate to a great degree. Thus, it can be used for simulation analysis of the designed control algorithms.

The piezoelectric driving force, sensor output, and the dynamical equation of the system are needed in the follow-up simulation. However, these equations cannot be obtained by using ANSYS. Therefore, it is necessary to write a program to get the model of the system.

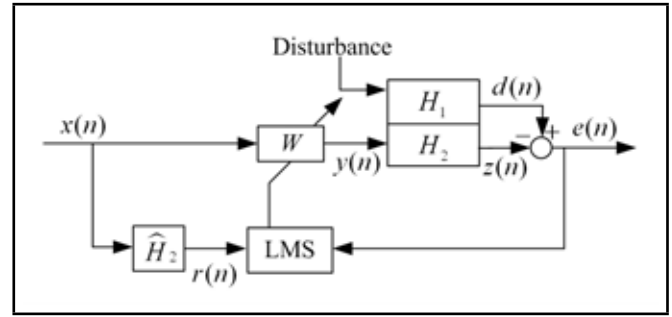
By using the finite element modelling method, \mathbf{A} , \mathbf{B}_f , \mathbf{B}_u , and \mathbf{C} , the state space equation can be obtained. The sampling period is specified as $T_s = 3$ ms. By converting the continuous-time model to the discrete-time one, the coefficient matrices of the discrete-time system are obtained and used in the subsequent simulation.

4. LMS AND FILTERED-X LMS FEEDFORWARD CONTROL ALGORITHM

4.1. LMS Algorithm

The adaptive filter is composed of a digital filter and an adaptive algorithm; $x(n)$, $d(n)$, $e(n)$ and $y(n)$ are the reference signal, desired response, error signal, and control output of the filter at the n th sampling instant, respectively. The coefficients of the digital filter are adjusted according to the adaptive algorithm so as to minimize the mean square of the error signal.

The transversal finite impulse response (FIR) adaptive filter is widely used due to its stability. The property of the transversal filter is determined by the weights $w_i(n)$. The input signals are multiplied by the weights and summed to form an output that will be equal to a desired response $d(n)$. The input signal vector, also called the reference signal at the n th step, is $\mathbf{X}(n) = [x(n), x(n-1), \dots, x(n-N+1)]^T$. The weights are written in a vector form $\mathbf{W}(n) =$


Figure 8. Scheme of the feedforward control.

$[w_1(n), w_2(n), \dots, w_N(n)]^T$ of length N . It is the kernel of the algorithm.

Therefore, the so-called Widrow-Hoff LMS can be summarized as follows

$$\begin{cases} y(n) = \mathbf{X}^T(n)\mathbf{W}(n) \\ e(n) = d(n) - \mathbf{X}^T(n)\mathbf{W}(n) \\ \mathbf{W}(n+1) = \mathbf{W}(n) + 2\mu e(n)\mathbf{X}(n) \end{cases}; \quad (13)$$

where the bounds of the convergence parameter μ is $0 < \mu < 1/\lambda_{\max}$; λ_{\max} is the largest eigenvalue of the autocorrelation matrix of the input signal.^{29,30}

4.2. Filtered-X LMS Feedforward Control Algorithm

The filtered-X LMS feedforward control is an algorithm that aims to minimize the mean square value of the vibration at a measuring point. Figure 8 shows the scheme of the feedforward control based on the LMS algorithm. In Fig. 8, $z(n)$ is assumed as the control response of the controlled structure at the n th sampling instant. H_1 and H_2 are the primary (error) path and secondary (control) path of the controlled structure, respectively. \hat{H}_2 is the estimation of H_2 , and it is written as $\hat{H}_2 = [h_1, h_2, \dots, h_P]^T$, where P is the order.

Let $\mathbf{X}_r(n)$ be the reference signal vector; $\mathbf{Y}(n)$ is the output vector of the controller. The so-called filtered-X signal vector $\mathbf{R}(n)$ is $\mathbf{R}(n) = [r(n), r(n-1), \dots, r(n-N+1)]^T$.

The filtered-X signal at the n th time is expressed by^{29,41}

$$r(n) = \hat{\mathbf{H}}_2^T \mathbf{X}_r(n) = \sum_{k=1}^P h_k x(n-k+1). \quad (14)$$

The iterative process of the filtered-X LMS control algorithm can be summarized as follows:^{29,41}

$$\begin{cases} y(n) = \mathbf{X}^T(n)\mathbf{W}(n) \\ e(n) = d(n) - \mathbf{R}^T(n)\mathbf{W}(n) \\ \mathbf{W}(n+1) = \mathbf{W}(n) + 2\mu e(n)\mathbf{R}(n) \end{cases}. \quad (15)$$

Comparing Eq. (15) with Eq. (13), one can easily find that in the filtered-X LMS algorithm, the reference signal $\mathbf{X}(n)$ is replaced with the filtered-X signal $\mathbf{R}(n)$. There should be a measure to compensate for the time delay that is caused by the secondary path due to the existence of the secondary (control) path. Therefore, the reference signals should be first taken a convolution operation with the control path's estimation \hat{H}_2 , and the result is used to update the weight vector.

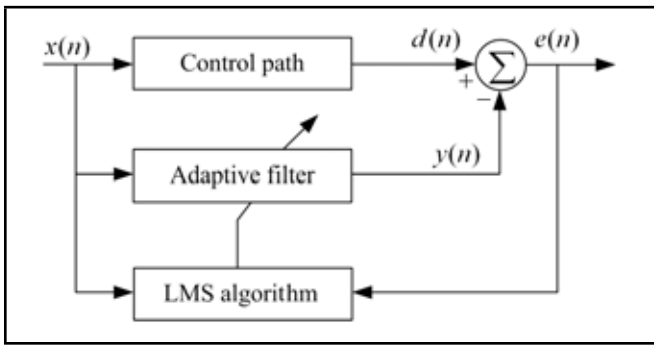


Figure 9. Schematic diagram of control path identification.

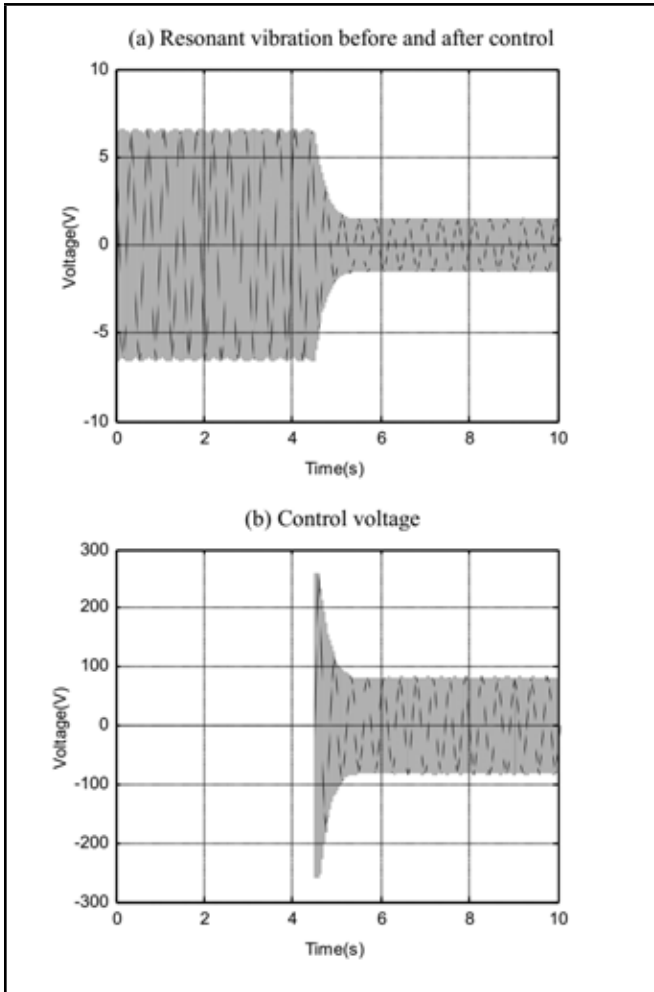


Figure 10. The time-domain response of vibration control under resonant excitation using PD control.

The filtered-X filtering algorithm is based on the FIR filter to guarantee the stability of the system. Although the algorithm has the merits of a simple structure and easy implementation, it also has to satisfy the following assumptions: a) the reference signals are highly related to the vibration signal, which correlates with the control effect of the algorithm; b) the control output of the controller has no influence on the reference, otherwise the stability of the system may be reduced. Therefore, the filtered-X LMS algorithm may have limitations to some extent.

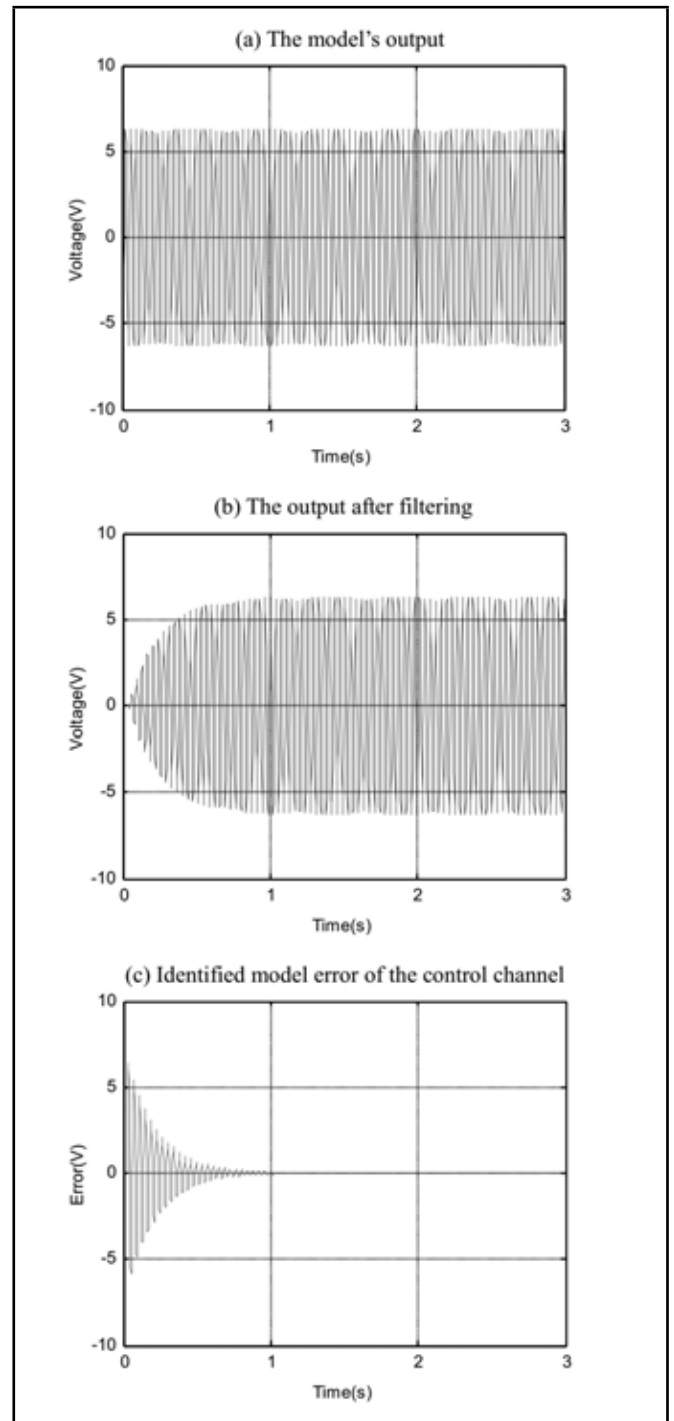


Figure 11. Simulating identification of control channel transfer parameters.

4.3. Control Path Identification

As shown in Fig. 9, an estimation model \hat{H}_2 of the control path H_2 has to be obtained while using the filtered-X LMS control method. There are mainly two kinds of system identification methods: adaptive online identification and adaptive offline modelling. The model obtained by adaptive online identification is more accurate than that of offline modelling. However, the realization of online identification is more complicated than that of offline modelling. The characteristic of the plate system is almost invariant in the following experiment. Therefore, an adaptive offline modelling method for system identification is adopted for estimating the model subsequently.

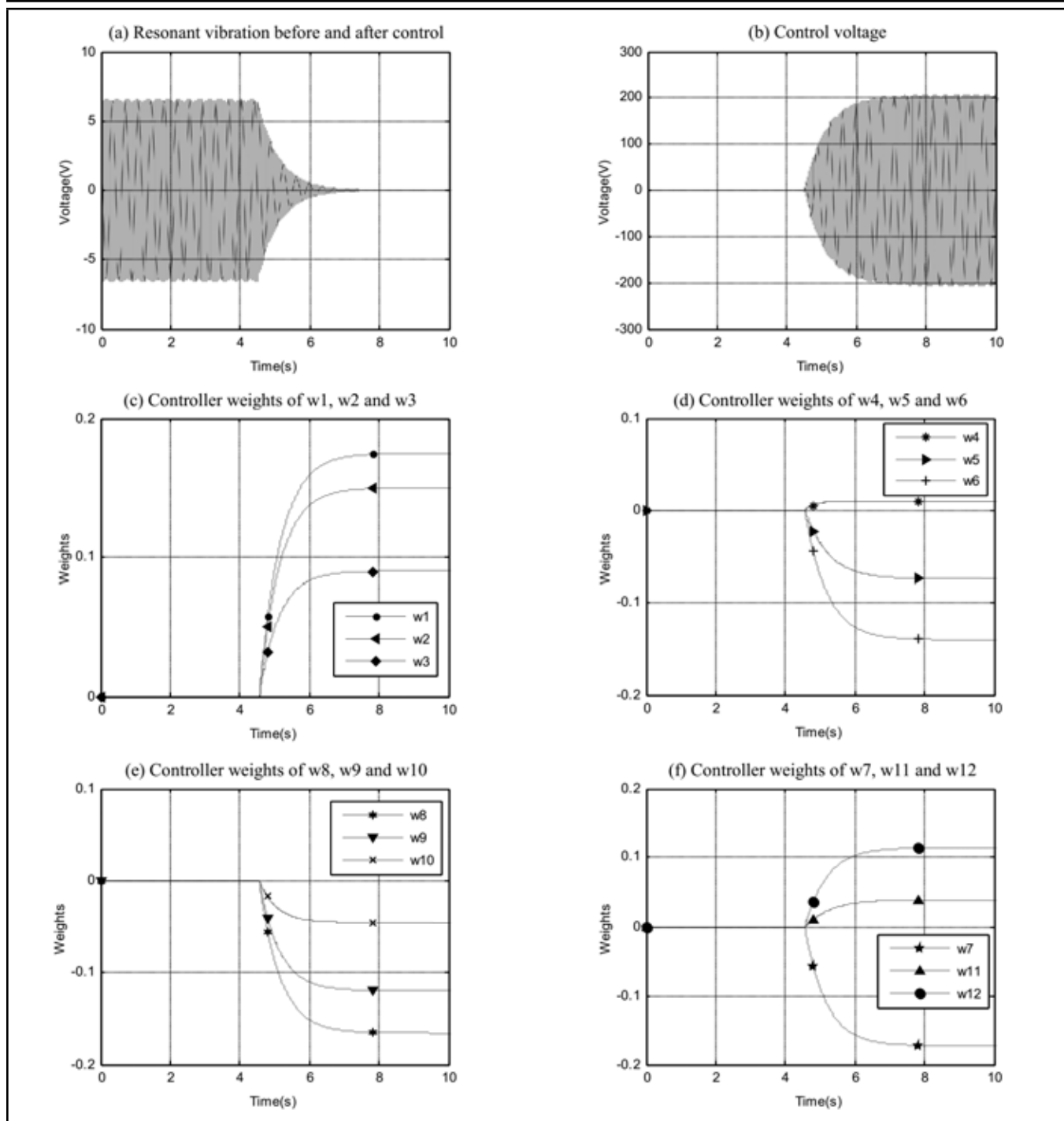


Figure 12. The time-domain response of vibration control under resonant excitation using filtered-X LMS control.

The working principle of Fig. 9 can be explained as following: the system to be identified and the adaptive filter are excited by the same input $x(n)$. Then, one can get an error signal between the actual output and the filter's output. The error signal is used by the LMS algorithm to adjust the weights of the filter. Then the control output of the filter gradually gets closer to the actual output of the system. As soon as the error signal approaches zero, the filter's output is almost the same as that of the actual output. At that time, the model of the adaptive filter can be used as the estimation model of the identified system.

In the process of system identification, an adaptive FIR filter is defined as the estimation model of the control path. Accordingly, the adaptive FIR filter works on the basis of the LMS algorithm. During the identification process, the selection of the

FIR filter's order is important. If the order is selected too low, the precision of the obtained model will be decreased. Otherwise, if the order selected is too high, phase difference between the estimation model and the actual model will be very large. Thus, the stability of the closed-loop system will be affected.

4.4. Control Simulation

In this section, numerical simulation is carried out to evaluate the effectiveness of two algorithms. The first one is the PD controller, and the second one is adaptive feedforward control algorithm with an adaptive FIR controller based on the LMS algorithm. The model obtained by using the finite element modelling method in Section 3.3 is used for simulation inves-

tigation. The excited signal actuated on the actuators is a sinusoidal signal with the frequency of 25.9 Hz and the amplitude of 4 V. The control gains of the applied PD control algorithm are specified as $K_p = 1.0$, $K_d = 0.001$. The control action is applied at the moment of $t = 4.5$ s.

The time-domain responses of vibration suppression and control voltage are shown in Fig. 10(a) and Fig. 10(b), respectively. As depicted in Fig. 10(a), the vibration amplitude attenuates more than 70% after the active control is applied.

When using the filtered-X LMS control algorithm, the adaptive FIR filter estimation model of the control path has to be obtained beforehand. The system identification is carried out by using the LMS algorithm. The sinusoidal signal is implemented in the control path of the model built by FEM, and then an adaptive FIR filter estimation model can be eventually obtained. The order of the adaptive FIR filter is specified as 12.

Figure 11(a) and Fig. 11(b) are the model's output and the filter's output, respectively. Figure 11(c) shows the identified model error of the control channel. It can be seen that the error is almost equal to zero after one second. This means that the output of the adaptive filter is almost the same as that of the model's output. The estimation adaptive FIR filter model of the control path is obtained.

The estimation model of the control path in the FIR adaptive filter using in simulation is $\hat{H}_2 = [0.2636 \ 0.2404 \ 0.1536 \ 0.0261 \ -0.1082 \ -0.2139 \ -0.2630 \ -0.2425 \ -0.1579 \ -0.0314 \ 0.1034 \ 0.2108]$.

The convergence factor used in the simulation is $\mu = 0.00002$. The order of the adaptive filter is specified as 12. Once the estimation model of the control path is obtained, the simulation results of the filtered-X LMS control method are shown in Fig. 12.

Figure 12(a) depicts the time-domain resonant vibration response before and after control using the filtered-X LMS algorithm. Figure 12(b) shows the control voltage applied to the PZT actuators. The controller weights of the adaptive filter are shown in Figs. 12(c), 12(d), 12(e), and 12(f).

From Figs. 12(c)–12(f), it can be seen that the controller voltage is small at first due to the initial small weights values. As time goes by, the weights are adjusted according to the reference signal and the vibration signal. It can be seen that the control voltage is gradually increasing, as shown in Fig. 12(b). The voltage is stable after 8 s, as shown in Fig. 12(b). The vibration amplitude is almost suppressed to zero after 8 s, as shown in Fig. 12(a).

From the simulation results, one can conclude that the filtered-X LMS algorithm can suppress the resonant vibration effectively. Although the PD controller attenuates the vibration in a shorter time, the vibration no longer attenuates after 5.2 s, as shown in Fig. 10(a). Therefore, the filtered-X LMS algorithm shows a better performance in controlling the vibration under resonant excitation.

5. EXPERIMENTAL RESULTS

5.1. Experimental Set-up

To validate the feasibility and the performance of the optimal placement of sensors/actuators and the applied adaptive feedforward control algorithms, an active vibration control

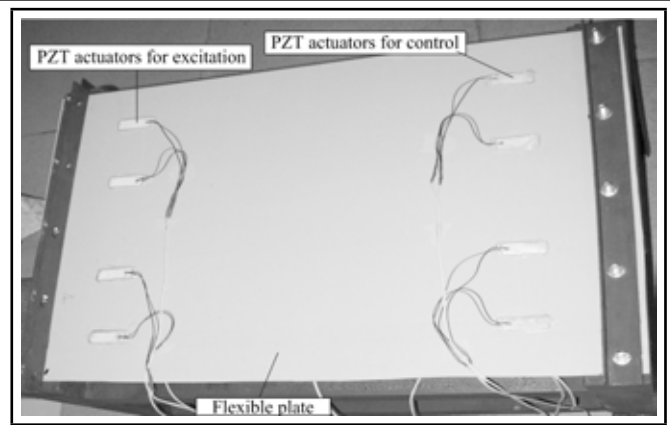


Figure 13. Photograph of the experimental setup.

system of a clamped-clamped flexible plate was developed according to the previous analyses. Experiments on the resonant vibration suppression of the piezoelectric flexible plate were conducted.

The experimental setup mainly consisted of a piezoelectric flexible clamped-clamped plate, the resonant excitation system, and the measurement and the control system. The photograph of the clamped-clamped plate setup is shown in Fig. 13. The plate is made up of epoxy resin. The dimensions and material properties of the plate and piezoelectric patches are given in Section 3.3.

A signal generator is used to generate sinusoidal signals. The measured signal of the PZT sensor is amplified by a charger amplifier (YE5850). One piezoelectric amplifier (PA-I) is used to amplify the output control voltages. The output signal after the D/A converter ranges from -5 V to $+5$ V, and after amplifying, the driving voltage for the control actuator ranges from -260 V to $+260$ V. The other piezoelectric amplifier (PA-II) is used to amplify the generated signal by the generator in order to excite the resonant vibration of the plate. It can amplify the excitation sinusoidal signal (from -5 V to $+5$ V) to a high voltage (from -130 V to $+130$ V). An ARM board and a personal computer (PC) are used as the signal processing and the control system with the corresponding A/D (analog to digital) and D/A (digital to analog) peripheral expander circuit. The control code is written in C++ language. The sampling interval is chosen as 3 ms.

5.2. Experimental Identification and Filters Design

Since there are many factors such as the unknown physical properties of epoxy resin material, the modal frequencies of the system have to be identified. A swept sine (chirp) signal is generated by the signal generator. The starting frequency is 0.5 Hz, and the stop frequency is 50 Hz. The swept time is 50 s.

Figure 14(a) shows the excited swept sinusoidal signal and the time-domain response signal measured by the PZT sensor when excited by PZT excitation actuators by amplifying the swept signal using the piezoelectric amplifier (PA-II). Figure 14(b) depicts the frequency response of the plate by using FFT for the time domain signal plotted in Fig. 14(a). From Fig. 14(b), it can be known that the first modal frequency of the plate is 21.6 Hz.

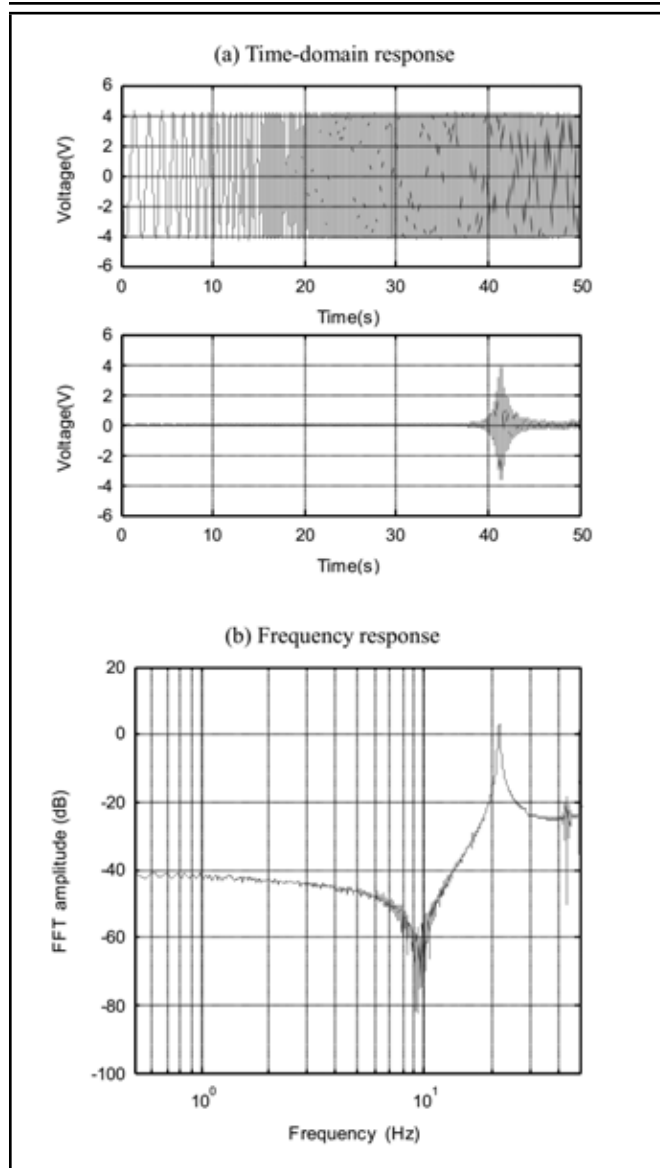


Figure 14. Measured swept sine vibration response excited by PZT actuators.

The natural frequency of the first mode obtained from the FEM model is 25.9 Hz; while in the experiments, the identified modal frequency is 21.6 Hz. The possible reasons which may lead to the difference of modal frequencies between the calculated and the experimental are listed as follow: (a) The clamped-clamped boundary condition in the simulation is ideal; while in the experiments, the boundaries may not be totally clamped. (b) The physical parameters of the flexible plate cannot be known accurately, such as the material density, Young's modulus, uniformity, etc. These parameters used in the simulation are not precisely consistent with those of the flexible plate used in the experimental material perfectly. This factor may also lead to the difference between the two modal frequencies. (c) Moreover, the mass of the glue and the connected signal wires of the PZT patches are not considered in the calculation. These factors will decrease the modal frequency in the experimental system. Since the calculated modal frequency is used to get an approximate value in order to verify the feasibility of the control algorithms, the difference of modal frequencies between the calculated and the experimental can be acceptable for this verification.

When the vibration of the first mode of the clamped-

clamped plate is excited, some harmonic frequency components are easily excited. High-frequency noise also exists in the measured signal. Those harmonic frequency components and high-frequency noises will affect the control performance of the experiments and sometimes even make the system unstable. Therefore, the actual vibration signal should be processed by predefined filters before conducting active vibration control experiments.

In the experiments, Chebyshev filters are designed to process the measured vibration signal by the PZT sensor. The Chebyshev filter attenuates fast in the transitional zone. Though amplitude fluctuates in its passband, the Chebyshev filter has the minimum error with an ideal filter frequency response curve. There are two kinds of Chebyshev filters. One is named the Type I Chebyshev filter, with a ripple in the passband; the other is the Type II Chebyshev filter, with a ripple in the stopband.

The Type I Chebyshev filter is used here. Since only the vibration of the first mode is considered, a fourth order Chebyshev band-pass filter is designed for signal processing. The central frequency is equal to the first modal frequency of 21.6 Hz. The bandwidth of the passband is set as 30 rad/s. The ripple of the passband is less than 1 dB.

5.3. Experiments on Resonant Vibration Suppression using PD Control

The sinusoidal signal is generated by a signal generator. Its amplitude and frequency are 4 V and 21.6 Hz, respectively. The frequency is the same as that of the first vibration mode. The time-domain response of vibration suppression under resonant excitation is shown in Fig. 15(a), using PD control. Figure 15(b) shows the control voltage. The proportional and derivative control gains are specified as $K_p = 0.95$, $K_d = 0.001$, respectively

It can be seen from Fig. 15(b) that once the control action is applied, the control voltage reaches saturation abruptly. The large amplitude vibration is suppressed to a small amplitude vibration in Fig. 15(a) quickly, and the control voltage is decreased due to the fact that the control value under the PD control is equal to the sum of the vibration signal and its derivative by multiplying the corresponding control gains.

From Fig. 15(a), it can be seen that the vibration amplitude is constant after 8 s. The amplitude of the control voltage will not change after 8 s, as shown in Fig. 15(b). The experimental results demonstrate the effectiveness of the PD controller. The PD control experiment results are in good accordance with the simulation results to some degree.

5.4. Experiments on Resonant Vibration Suppression using Filtered-X LMS Algorithm

Similar to the simulation research, an offline identification of the control path between the actuator and the sensor is performed. The dimension for the identified model on the experiment is set as 12. It is required that the dimension of the identified model should describe the characteristics of the system accurately. Generally, the dimension should be set as small as possible provided that it could meet the control requirements. Because the higher the dimension of the

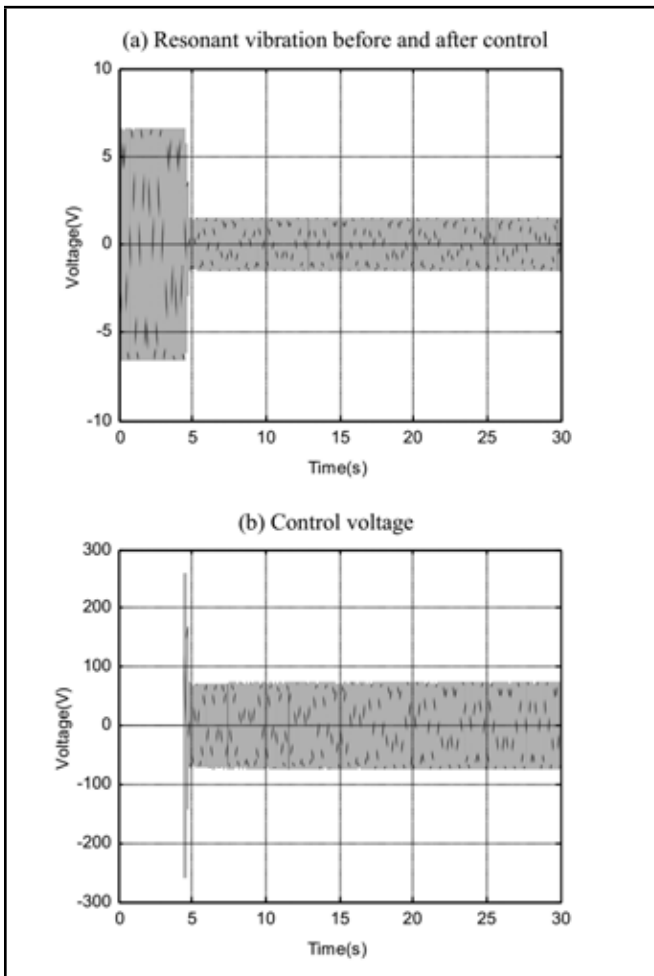


Figure 15. The time-domain response of vibration control under resonant excitation using PD control.

identified model is, the greater the amount of calculation is required. Then real-time control will be much more difficult due to the computational burden. Therefore, the dimension for the identified model should be set appropriately to meet the experimental conditions. The dimension of 12 is chosen after many times of experimental testing. It could not only satisfy the accuracy of the model but also meet the real-time requirements. The data acquisition of the input sinusoidal signal and the output signal measured by the PZT sensor is carried out by using the ARM controller with the expander circuit at a sampling frequency of 333 Hz. Figure 16(a) and Fig. 16(b) are the actual outputs measured by the PZT sensor and the adaptive filter's output, respectively. Figure 16(c) shows that the identified model error is almost zero after 1 s. The estimated model of the control path is $\hat{H}_2 = [-0.5128 \ -0.2873 \ -0.0149 \ 0.2600 \ 0.4924 \ 0.6443 \ 0.6908 \ 0.6243 \ 0.4558 \ 0.2127 \ -0.0652 \ -0.3324]$.

The convergence factor used in the experiment is chosen as $\mu = 0.000018$. The order of the adaptive filter is specified as 12. The results of the filtered-X LMS control method are shown in Fig. 17.

By comparing Fig. 17(a) with Fig. 15(a), one can find that the transient response time of the designed filtered-X LMS algorithm is longer than that of the applied PD control. This is the reason why the corresponding weights are adaptively adjusted online. In the process of dynamic adjusting, the control weights arrive to the best values gradually. Therefore, the con-

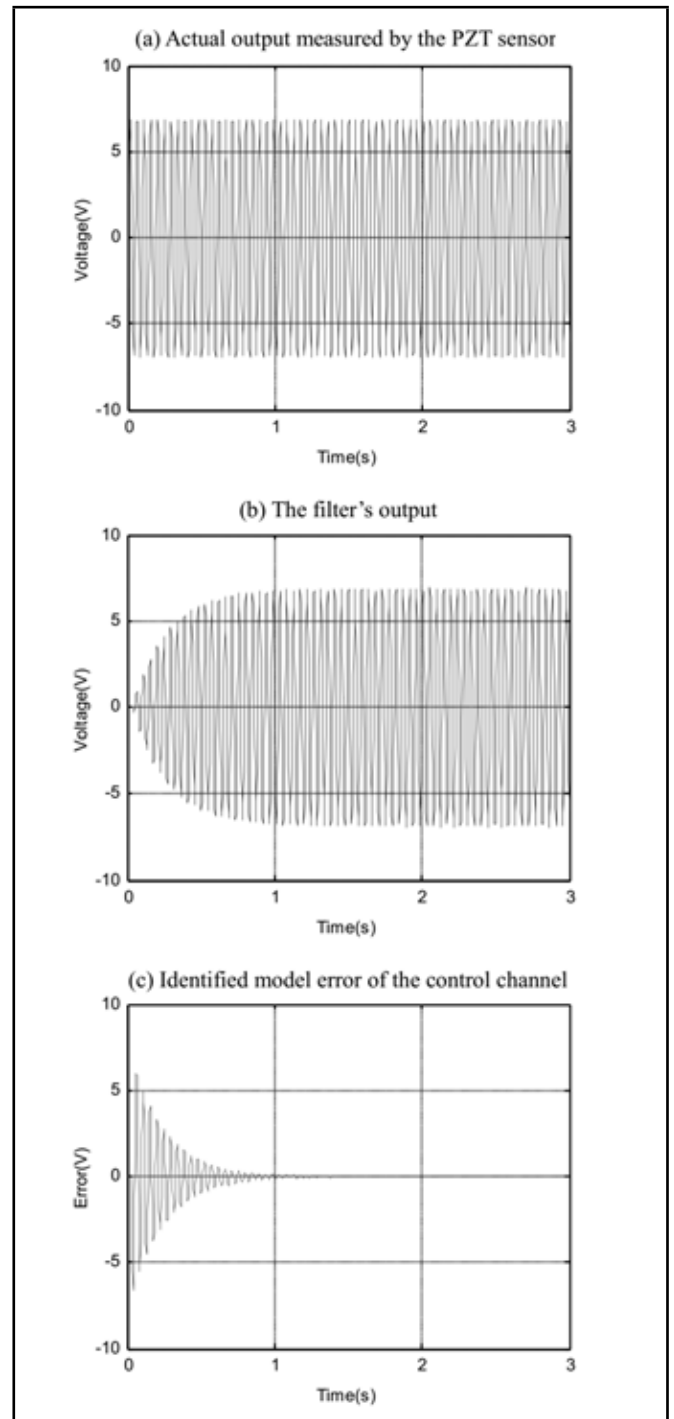


Figure 16. Experimental identification of the control channel transfer parameters.

trol performance of this process is not good enough. However, the vibration attenuates to a smaller value eventually with the weights reaching the best scope, as in Fig. 17(a). The vibration amplitude plotted in Fig. 17(a) is less than 1 V while the vibration amplitude illustrated in Fig. 15(a) is about 1.5 V. Therefore, the control performance of the filtered-X LMS is better than that of PD algorithm in the long run.

Moreover, the control voltage doesn't reach over saturation, as depicted in Fig. 17(b). This will not cause damage to the experimental apparatus. Figures 17(c)–17(f) show the self-regulating process of the corresponding weights. It should be emphasized that to view all control weights clearly, the serial number of control weights in one picture may be discontinu-

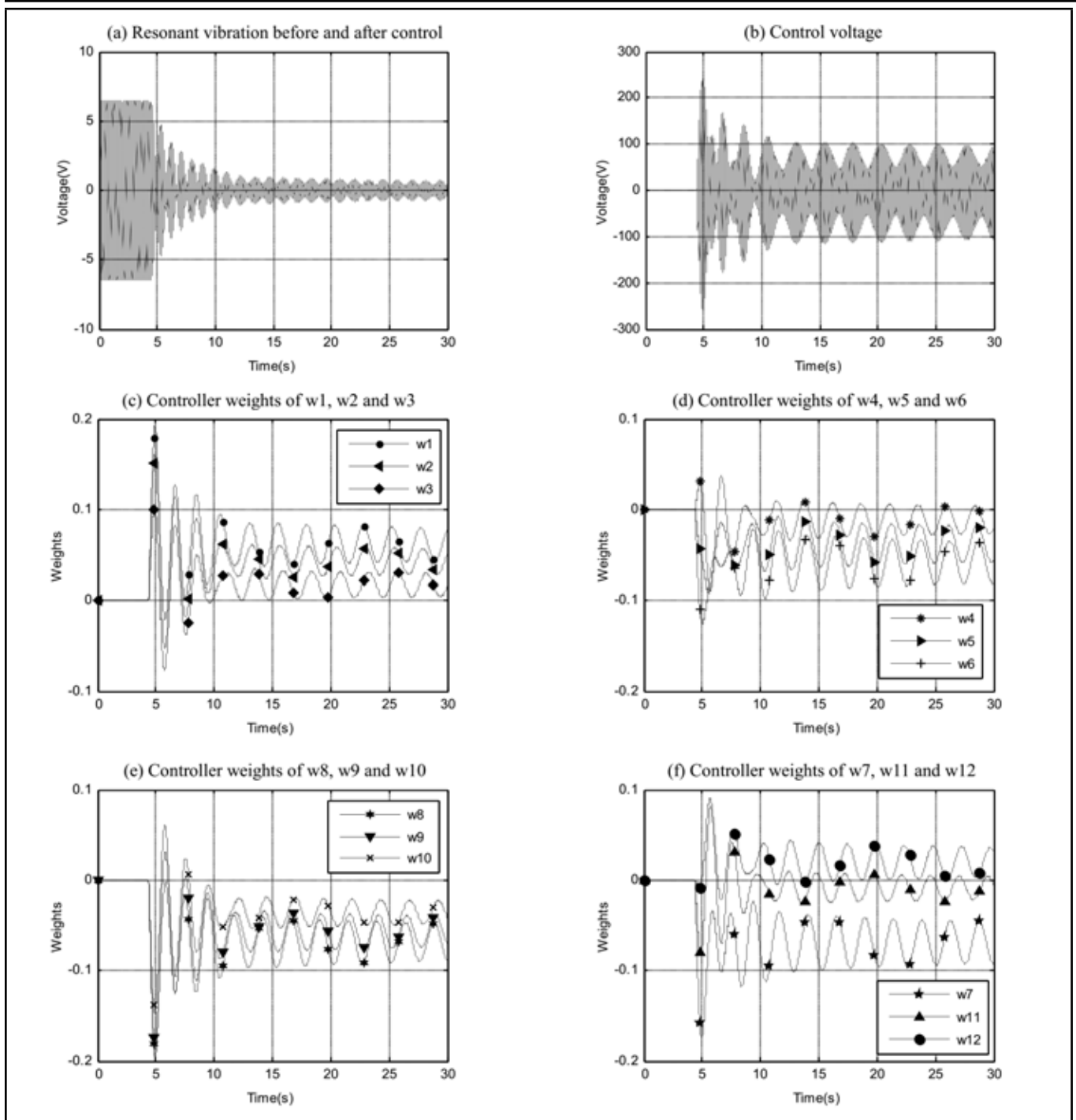


Figure 17. The time-domain response of vibration control under resonant excitation using filtered-X LMS control.

ous. The control voltage in Fig. 17(b) is tuned according to the controller weights, while the controller weights in Figs. 17(c), 17(d), 17(e), and 17(f) are adjusted according to the reference signal and the vibration signal.

The actual vibration control result shown in Fig. 17(a) is not as good as that of the simulation in Fig. 12(a). Actually, the experimental phenomenon plotted in Fig. 17(a) is caused due to the inconformity between the physical control path and the identified control path. Gain error and phase error exist between the physical control path and the identified control path. Gain error can be neglected by adjusting gain of the control path, while the phase error cannot be diminished. The phase error is first transmitted to the filtered-X signal according to Eq. (14), and then it is transmitted to the control weights. The

phase errors are accumulated to the control output.

The resonant vibration can still be attenuated to a very small value due to the robustness to uncertainties of filtered-X LMS algorithm. From Fig. 17(a), one can see that the vibration reaches the dynamic balance after several times of adjustment. The vibration amplitude alternates from a little larger to even smaller. When the vibration amplitude gets bigger in Fig. 17(a), the controller weights are tuned online according to the current sensor signal and the latest reference signal, thus the control voltage becomes larger.

The control performance of the filtered-X LMS algorithm is related with the selections of the convergence factor μ , the dimension for the identified model of the control path, and the order of adaptive filter. The value of μ is based on the autocor-

relation matrix eigenvalue of the input signal. The convergence and convergence rate of the filtered-X LMS algorithm should be guaranteed. The value range of μ should meet the inequality: $0 < \mu < 1/\lambda_{\max}$. Actually, the optimal value can be selected through experimental tests. The larger value of μ will lead to a faster convergence rate. However, a value of μ that is too large should not be chosen in order to avoid divergence in the control process. The dimension for the identified model of the control path and the order of the adaptive filter will also affect the control performance. A higher dimension will lead to better performance. However, a larger amount of calculations will also be necessary. Therefore, the dimension for the identified model of the control path and the order of the adaptive filter should be specified appropriately, considering both the control performance and the real-time requirements.

From the experimental results, it can be concluded that the resonant vibration of the clamped-clamped plate can be suppressed effectively by using the PD controller and the filtered-X LMS feedforward controller. In addition, control over saturation is prevented by using the filtered-X LMS control algorithm. Moreover, the control performance is also improved by using the designed filter-X LMS algorithm.

6. CONCLUSIONS

This paper presents the numerical and experimental results for resonant vibration control of a piezoelectric clamped-clamped plate excited by piezoelectric actuators. The dynamics model of the system is obtained by using the finite element method. Locations of the PZT sensors and actuators are optimized by optimal placement criteria and GA search methods. A fourth order Chebyshev band-pass filter is designed to eliminate the noises from the vibration signal measured by the PZT sensor. Numerical simulations and experiments are carried out to verify the effectiveness and feasibility of the optimal placement of piezoelectric sensors/actuators and the designed control algorithms, including PD control and filtered-X LMS feedforward control method. Simulation and experimental results demonstrated that excited resonant vibration can be suppressed effectively by the proposed two control methods and the location of sensors/actuators. Moreover, the filtered-X LMS algorithm shows better control performance in suppressing the resonant vibration.

FUNDING

This work was partially supported by the National Natural Science Foundation of China under Grants 51175181 and 60934001, and partially supported by the Fundamental Research Funds for the Central Universities (SCUT, 2014ZG0019), partially supported by National Laboratory of Space Intelligent Control. The authors gratefully acknowledge these support agencies.

REFERENCES

- ¹ Niederberger, D., Morari, M., and Pietrzko, S. J. Adaptive resonant shunted piezoelectric devices for vibration suppression, *Proc. of SPIE Smart Structures and Materials*, **5056**, 213–224, (2003).
- ² Wu, S. Y., Turner, T. L., and Rizzi, S. A. Piezoelectric shunt vibration damping of an F-15 panel under high-acoustic excitation, *SPIE's 7th Annual International Symposium on Smart Structures and Materials*, International Society for Optics and Photonics, 276–287, (2000).
- ³ Hyland, D., Junkins, J., and Longman, R. Active control technology for large space structures, *Journal of Guidance, Control, and Dynamics*, **16**, 801–821, (1993).
- ⁴ Qiu, Z. C., Zhang, X. T., and Ye, C. D. Vibration suppression of a flexible piezoelectric beam using BP neural network controller, *Acta Mechanica Solida Sinica*, **25**, 417–428, (2012).
- ⁵ Moon, S. H. and Kim, S. J. Suppression of nonlinear composite panel flutter with active/passive hybrid piezoelectric networks using finite element method, *Composite structures*, **59**, 525–533, (2003).
- ⁶ Zhou, R., Lai, Z., Xue, D. Y., et al. Suppression of nonlinear panel flutter with piezoelectric actuators using finite element method, *AIAA Journal*, **33**, 1098–1105, (1995).
- ⁷ Forward, R. Electronic Damping of Orthogonal Bending Modes in a Cylindrical Mast-Experiment, *Journal of Spacecraft and Rockets*, **18** (1), 11–17, (1981).
- ⁸ Bailey, T. and Hubbard, J. Distributed piezoelectric-polymer active vibration control of a cantilever beam, *Journal of Guidance, Control, and Dynamics*, **8** (5), 605–611, (1985).
- ⁹ Li, F.-M. Active aeroelastic flutter suppression of a supersonic plate with piezoelectric material, *International Journal of Engineering Science*, **51**, 190–203, (2012).
- ¹⁰ Elshafei, M. A. and Alraies, F. Modeling and analysis of smart piezoelectric beams using simple higher order shear deformation theory, *Smart Materials and Structures*, **22**, 035006, (2013).
- ¹¹ Farhadi, S. and Hosseini-Hashemi, S. Active vibration suppression of moderately thick rectangular plates, *Journal of Vibration and Control*, **17**, 2040–2049, (2011).
- ¹² Ramu, I. and Mohanty, S. Study on Free Vibration Analysis of Rectangular Plate Structures Using Finite Element Method, *Procedia Engineering*, **38**, 2758–2766, (2012).
- ¹³ Arbel, A. Controllability measures and actuator placement in oscillatory systems, *International Journal of Control*, **33** (3), 565–574, (1981).
- ¹⁴ Bruant, I. and Proslie, L. Optimal location of actuators and sensors in active vibration control, *Journal of intelligent material systems and structures*, **16** (3), 197–206, (2005).
- ¹⁵ Ambrosio, P., Resta, F., and Ripamonti, F. An H_2 norm approach for the actuator and sensor placement in vibration control of a smart structure, *Smart Materials and Structures*, **21**, 125016, (2012).

- ¹⁶ Nestorović, T. and Trajkov, M. Optimal actuator and sensor placement based on balanced reduced models, *Mechanical Systems and Signal Processing*, **36** (2), 271–289, (2013).
- ¹⁷ Qiu, Z. C., Zhang, X. M., Wu, H. X., et al. Optimal placement and active vibration control for piezoelectric smart flexible cantilever plate, *Journal of Sound and Vibration*, **301**, 521–543, (2007).
- ¹⁸ Darivandi, N., Morris, K., and Khajepour, A. An algorithm for LQ optimal actuator location, *Smart Materials and Structures*, **22**, 035001, (2013).
- ¹⁹ Bachmann, F., Bergamini, A. E., and Ermanni, P. Optimum piezoelectric patch positioning: A strain energy-based finite element approach, *Journal of intelligent material systems and structures*, **23** (14), 1575–1591, (2012).
- ²⁰ Bruant, I., Gallimard, L., and Nikoukar, S. Optimal piezoelectric actuator and sensor location for active vibration control, using genetic algorithm, *Journal of Sound and Vibration*, **329**, 1615–1635, (2010).
- ²¹ Yang, Y., Jin, Z., and Kiong Soh, C. Integrated optimal design of vibration control system for smart beams using genetic algorithms, *Journal of Sound and Vibration*, **282**, 1293–1307, (2005).
- ²² Warminski, J., Bochenski, M., Jarzyna, W., et al. Active suppression of nonlinear composite beam vibrations by selected control algorithms, *Communications in Nonlinear Science and Numerical Simulation*, **16**, 2237–2248, (2011).
- ²³ Shin, C., Hong, C., and Jeong, W. B. Active vibration control of beam structures using acceleration feedback control with piezoceramic actuators, *Journal of Sound and Vibration*, **331**, 1257–1269, (2012).
- ²⁴ Lin, J. and Liu, W.-Z. Experimental evaluation of a piezoelectric vibration absorber using a simplified fuzzy controller in a cantilever beam, *Journal of Sound and Vibration*, **296**, 567–582, (2006).
- ²⁵ Qiu, Z. C., Wu, H. X., and Zhang, D. Experimental researches on sliding mode active vibration control of flexible piezoelectric cantilever plate integrated gyroscope, *Thin-Walled Structures*, **47**, 836–846, (2009).
- ²⁶ Kun, L., Long-Xiang, C., and Guo-Ping, C. An Experimental Study of Delayed Positive Feedback Control for a Flexible Plate, *International Journal of Acoustics and Vibration*, **17**, 171–180, (2012).
- ²⁷ Tong, Z., Long-Xiang, C. and Guo-Ping, C. Experimental study of H_∞ control for a flexible plate, *Journal of Vibration and Control*, **18**, 1631–1649, (2012).
- ²⁸ Ji, H., Qiu, J., Badel, A., et al. Semi-active vibration control of a composite beam by adaptive synchronized switching on voltage sources based on LMS algorithm, *Journal of intelligent material systems and structures*, **20**, 939–947, (2009).
- ²⁹ Morgan, D. R. History, Applications, and Subsequent Development of the FXLMS Algorithm [DSP History], *Signal Processing Magazine, IEEE*, **30**, 172–176, (2013).
- ³⁰ Widrow, B. and Stearns, S. D. *Adaptive Signal Processing*, Prentice Hall, Englewood Cliffs, NJ, (1985).
- ³¹ Anderson, E. H. and How, J. P. Adaptive feedforward control for actively isolated spacecraft platforms, *AIAA Structures, Structural Dynamics, and Materials Conference and Exhibit*, 7–10, (1997).
- ³² Zhu, X., Gao, Z., Huang, Q., et al. Analysis and implementation of MIMO FULMS algorithm for active vibration control, *Transactions of the Institute of Measurement and Control*, **34** (7), 815–828, (2011).
- ³³ Ma, K. Vibration control of smart structures with bonded PZT patches: novel adaptive filtering algorithm and hybrid control scheme, *Smart Materials and Structures*, **12** (3), 473–482, (2003).
- ³⁴ Carra, S., Amabili, M., Ohayon, R., et al. Active vibration control of a thin rectangular plate in air or in contact with water in presence of tonal primary disturbance, *Aerospace Science and Technology*, **12** (1), 54–61, (2008).
- ³⁵ Oh, J. E., Park, S. H., Hong, J. S., et al. Active vibration control of flexible cantilever beam using piezo actuator and Filtered-X LMS algorithm, *KSME International Journal*, **12**, 665–671, (1998).
- ³⁶ Carnahan, J. J. and Richards, C. M. A modification to filtered-X LMS control for airfoil vibration and flutter suppression, *Journal of Vibration and Control*, **14**, 831–848, (2008).
- ³⁷ Das, D. P., Moreau, D. J., and Cazzolato, B. S. A computationally efficient frequency-domain filtered-X LMS algorithm for virtual microphone, *Mechanical Systems and Signal Processing*, **37** (1–2), 440–454, (2013).
- ³⁸ Huang, Q., Luo, J., Li, H., et al. Analysis and implementation of a structural vibration control algorithm based on an IIR adaptive filter, *Smart Materials and Structures*, **22**, 085008, (2013).
- ³⁹ Clark, R. L., Saunders, W. R., and Gibbs, G. P. *Adaptive structures: dynamics and control*, Wiley, New York, (1998).
- ⁴⁰ Holland, J. H. *Adaption in Natural and Artificial Systems. An Introductory Analysis with Applications to Biology, Control, and Artificial Intelligence*, University of Michigan Press, Michigan, (1975).
- ⁴¹ Burgess, J. C. Active adaptive sound control in a duct: A computer simulation, *The Journal of the Acoustical Society of America*, **70** (3), 715–726, (1981).

Control of MR Damper Connected Buildings by Output Feedback

Gokarna Bahadur Motra and Naresh K. Chandiramani

Department of Civil Engineering, Indian Institute of Technology Bombay, Mumbai, 400076, India.

(Received 20 February 2013; revised: 14 October 2013; accepted: 14 October 2013)

The control of seismic response of buildings connected by a magnetorheological (MR) damper is studied. The desired control force is obtained using Linear Quadratic Gaussian (LQG) control based on the feedback of states estimated via measured outputs or Optimal Static Output Feedback (OSOF) control using the direct feedback of measured outputs. The damper input voltage is predicted using a Recurrent Neural Network (RNN), which proves more effective than the Clipped Voltage Law (CVL). Various sensor configurations and state weightings are considered to obtain effective control. LQG-RNN/OSOF-RNN yield significant reduction in response and base shear and require much less control effort compared to passive-on control with saturation voltage. Compared to passive-off control, they are very effective in attenuating maximum-peak/RMS responses and storeywise responses of the flexible building, except for max-peak accelerations that increase slightly. However, passive-off control is unable to transfer base shear to the stiffer building. LQG-RNN/OSOF-RNN also yield control at least as effective as LQR-RNN by deploying much fewer sensors but using a somewhat higher damper force. They are mostly comparable to each other, but OSOF-RNN requires an order-of-magnitude less CPU time for the control loop. Effective control is possible using few sensors.

1. INTRODUCTION

An earthquake induced response of adjacent buildings can be mitigated by connecting them with dampers. Semiactive devices, such as MR dampers, provide controllable damping with a low power expenditure.

Modelling of MR dampers is notably due to: Song et al.¹ who presented a model of an MR damper using polynomial functions and a first-order filter; Chang and Zhou² who proposed a recurrent neural network (RNN) model of an MR damper, which is appropriate for closed loop control; Spencer et al.³ who proposed the modified Bouc-Wen model, containing additional stiffness and damping elements to model accumulator and low-velocity behavior, respectively; Wang and Kamath⁴ who proposed a phase-transition model involving a nonlinear differential equation for damper force with velocity as input; and Jimenez and Alvarez-Icaza⁵ who presented a modified LuGre friction model by replacing material dependency with voltage dependency.

Predicting applied voltage to produce a desired damper force is difficult. This is due to the non-invertible force-voltage dynamics of hysteretic models for MR dampers. The controllers considered are notably due to: Xu and Shen⁶ who used intelligent bi-state control with a Bingham model and on-off current law and later Xu and Guo⁷ who proposed a neuro-fuzzy controller for damper current; Dyke et al.⁸ who used the modified Bouc-Wen model with acceleration feedback LQG control for desired damper force and proposed an on-off Clipped Voltage Law (CVL); Yuen et al.⁹ who used reliability based robust linear control for desired force and CVL for command voltage; Karamodin and Kazemi¹⁰ who used LQG control for desired force and a semiactive neural controller (using acceleration/velocity feedback) for damper voltage; and Bahar et al.¹¹ who designed a hierarchical controller with velocity feedback

for the desired force and proposed an inverse Bouc-Wen model for voltage.

Control of connected buildings with base excitation is notably due to: Aida and Aso¹² who used a passive connector and showed that damping improves when the connector is placed near the top and the natural frequencies are well separated; Ni et al.¹³ who experimentally showed, using an MR damper connector, that the optimum damper location is at the top of the shorter building; Zhu et al.¹⁴ who considered passive/active/semiactive connection elements, albeit without damper dynamics; Qu and Xu¹⁵ who used the Bingham MR model and instantaneous sub-optimal control with the damper relative displacement as the control input to study the whipping of a tall building connected to a podium; Xu et al.¹⁶ and Jing et al.¹⁷ who experimentally verified the results of Qu and Xu¹⁵ using single and multiple dampers, respectively; Christenson et al.¹⁸ who considered a semiactive damper without its dynamics and a clipped optimal controller that yields applied force instead of command voltage; and Cimellaro and Lopez-Garcia¹⁹ who performed constrained optimization design, using multiple passive dampers, to achieve performance equal to an LQR controller for white noise excitation.

In this study, a five-storey and a three-storey building are coupled with a single MR damper placed at the top of the shorter building. The system undergoes earthquake excitation. The objectives of the present study are: (i) Applying LQG control (with full state feedback and an optimal observer for state estimation based on measured outputs), and OSOF control (based directly on measured outputs), to obtain the desired control force. The hysteretic force-velocity behavior is modelled using the more accurate modified Bouc-Wen model. The aim here is to study the effectiveness of LQG/OSOF controllers that use fewer measured outputs than LQR control. (ii) Predicting, via RNN, the damper voltage required to produce the desired damper force obtained from LQG/OSOF control.

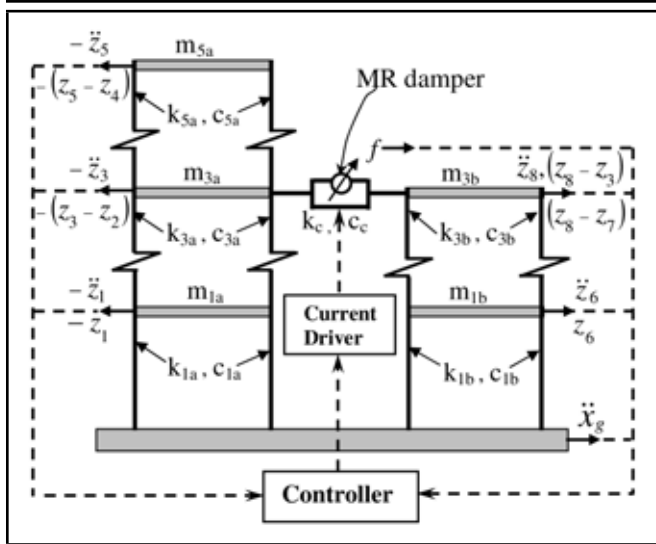


Figure 1. Buildings connected with MR damper.

The aim here is to compare the effectiveness of semiactive (i.e., LQG/OSOF/LQR) controllers based on RNN voltage law, with that of passive (constant voltage) controllers and semiactive controllers based on CVL (on-off) voltage law.

2. SYSTEM MODEL

The five- and three-storeyed buildings, B5 and B3, respectively, are assumed to have a symmetric plan, with the mass concentrated at rigid slabs. They are subject to the same horizontal uniaxial ground acceleration (Fig. 1). Let M_a , C_a , K_a and M_b , C_b , K_b denote mass, damping, stiffness matrices of B5 and B3, respectively; and c_c and k_c denote damping and stiffness coefficients, respectively, of the passive connector between B5 and B3. The system mass, damping, stiffness matrices, i.e., M_s , C_s , K_s , respectively, are

$$\begin{aligned} M_s &= \text{diag} [M_a \quad M_b]; \quad C_s = \text{diag} [C_a \quad C_b] + C_c; \\ K_s &= \text{diag} [K_a \quad K_b] + K_c; \end{aligned} \quad (1)$$

$$\begin{aligned} C_d &= \begin{bmatrix} 0 & 0 & 0 \\ 0 & 0 & 0 \\ 0 & 0 & c_c \end{bmatrix}; \quad C_c = \begin{bmatrix} C_d & 0 & -C_d \\ 0 & 0 & 0 \\ -C_d & 0 & C_d \end{bmatrix}; \\ K_d &= \begin{bmatrix} 0 & 0 & 0 \\ 0 & 0 & 0 \\ 0 & 0 & k_c \end{bmatrix}; \quad K_c = \begin{bmatrix} K_d & 0 & -K_d \\ 0 & 0 & 0 \\ -K_d & 0 & K_d \end{bmatrix}. \end{aligned} \quad (2)$$

The equation of motion for the coupled buildings system is

$$M_s \ddot{\mathbf{x}} + C_s \dot{\mathbf{x}} + K_s \mathbf{x} = \mathbf{D}f - M_s \mathbf{L} \ddot{x}_g; \quad (3)$$

where

$$\mathbf{D} = [0 \ 0 \ 1 \ 0 \ 0 \ 0 \ 0 \ -1]^T; \quad \mathbf{L} = [1 \ 1 \ 1 \ 1 \ 1 \ 1 \ 1 \ 1]^T; \quad \mathbf{f} = [f]. \quad (4)$$

Here, $\mathbf{x}(t) = [x_1 \ x_2 \ \dots \ x_8]^T$ is the displacement vector of the storeys of B5 (i.e., $[x_1 \ \dots \ x_5]^T$) and B3 (i.e., $[x_6 \ \dots \ x_8]^T$) measured relative to the ground, \mathbf{D} is the location matrix of MR damper forces, \mathbf{L} is the excitation influence vector, f is the MR damper force, and \ddot{x}_g is the ground acceleration. Defining the mechanical states $\mathbf{z}(t) = [\mathbf{x} \ \dot{\mathbf{x}}]^T$, the state equations are

$$\dot{\mathbf{z}} = \mathbf{A} \mathbf{z} + \mathbf{B} \mathbf{f} + \mathbf{E} \ddot{x}_g; \quad (5)$$

where state matrix \mathbf{A} , control input location matrix \mathbf{B} , earthquake excitation location matrix \mathbf{E} , and control input vector \mathbf{f} are

$$\begin{aligned} \mathbf{A} &= \begin{bmatrix} \mathbf{0} & \mathbf{I} \\ -\mathbf{M}_s^{-1} \mathbf{K}_s & -\mathbf{M}_s^{-1} \mathbf{C}_s \end{bmatrix}; \quad \mathbf{B} = \begin{bmatrix} \mathbf{0} \\ \mathbf{M}_s^{-1} \mathbf{D} \end{bmatrix}; \\ \mathbf{E} &= \begin{bmatrix} \mathbf{0} \\ -\mathbf{L} \end{bmatrix}; \quad \mathbf{f} = [f]. \end{aligned} \quad (6)$$

The modified Bouc-Wen model of Spencer et al.,³ involving voltage dependent parameters, is used to obtain the damper force, f , as follows:

$$f = c_1 \dot{y} + k_1 (z_8 - z_3); \quad (7)$$

where,

$$\dot{y} = \frac{1}{(c_0 + c_1)} \{ \alpha z_d + c_0 (z_{16} - z_{11}) + k_0 (z_8 - z_3 - y) \}; \quad (8)$$

$$\begin{aligned} \dot{z}_d &= -\gamma |z_{16} - z_{11} - \dot{y}| z_d |z_d|^{n-1} - \beta (z_{16} - z_{11} - \dot{y}) |z_d|^n + \\ &A (z_{16} - z_{11} - \dot{y}); \end{aligned} \quad (9)$$

$$\dot{u} = -\eta (u - v); \quad (10)$$

$$\alpha = \alpha_a + \alpha_b u; \quad c_1 = c_{1a} + c_{1b} u; \quad c_0 = c_{0a} + c_{0b} u. \quad (11)$$

Here $z_3 (= x_3)$, $z_8 (= x_8)$ are the displacements, and $z_{11} (= \dot{x}_3)$, $z_{16} (= \dot{x}_8)$ are the velocities, of storey three of B5, B3, respectively; y is an internal pseudo-displacement; z_d is the evolutionary variable describing damper hysteresis; u is the output of a first order filter, which models delay dynamics of the current driver and of the fluid to reach rheological equilibrium; v is the command voltage supplied to the damper. Data for hysteresis loop parameters (γ , β , A , n), spring stiffnesses (k_0 , k_1), and viscous damping coefficients (c_0 , c_1), are considered from Spencer et al.³

3. CONTROLLER DESIGN

Implementation of LQR control requires that all states be measured for feedback. This is often not possible. Hence, controllers using measured output to estimate states and then obtain the control input, or controllers that directly feed back measured outputs to obtain the control input, are considered. The control input thus obtained is the desired damper force f_d . Further, inverting damper dynamics to obtain command voltage v , that is required to produce f_d , is a nontrivial task (Eqs. (7)–(11)). Hence, voltage laws are considered to obtain v that produces a control input \mathbf{f} as close as possible to the desired control input \mathbf{f}_d .

3.1. LQG Control

A Kalman filter (optimal observer) is designed to estimate the states for subsequent use in the LQR controller.²⁰ The state equations describing plant dynamics, i.e., Eq. (5), contain ground acceleration \ddot{x}_g as the plant noise. Measured outputs are given by

$$\mathbf{y} = \mathbf{C} \mathbf{z} + \mathbf{D}_1 \mathbf{f} + \mathbf{v}. \quad (12)$$

The measurement noise, \mathbf{v} , is assumed uncorrelated with the plant noise, and both are assumed as zero-mean white noise

processes. Table 1 shows the combinations of measured outputs (comprising storey accelerations, interstorey drifts, and relative displacement of damper) considered. For example, for (8A,11D) sensor configuration the output and direct transmission matrices are

$$\mathbf{C} = \begin{bmatrix} -\mathbf{M}_s^{-1}\mathbf{K}_s & -\mathbf{M}_s^{-1}\mathbf{C}_s \\ 0 & \mathbf{0}_{8 \times 1} \end{bmatrix}; \quad \mathbf{D}_1 = \begin{bmatrix} \mathbf{M}_s^{-1}\mathbf{D} \\ 0 \end{bmatrix}. \quad (13)$$

The estimated state vector, $\hat{\mathbf{z}}$, is obtained via the observer dynamics, i.e.,

$$\dot{\hat{\mathbf{z}}} = (\mathbf{A} - \mathbf{L}_1\mathbf{C})\hat{\mathbf{z}} + (\mathbf{B} - \mathbf{L}_1\mathbf{D}_1)\mathbf{f} + \mathbf{L}_1\mathbf{y}; \quad (14)$$

in which the optimal observer gain \mathbf{L}_1 (obtained by minimizing the covariance of state estimation error $\mathbf{z} - \hat{\mathbf{z}}$) is given as

$$\mathbf{L}_1 = \mathbf{P}^*\mathbf{C}^T\mathbf{R}^{*-1}; \quad (15)$$

where \mathbf{P}^* is the solution of the algebraic Riccati equation

$$\mathbf{A}\mathbf{P}^* + \mathbf{P}^*\mathbf{A}^T - \mathbf{P}^*\mathbf{C}^T\mathbf{R}^{*-1}\mathbf{C}\mathbf{P}^* + \mathbf{G}\mathbf{Q}^*\mathbf{G}^T = \mathbf{0}. \quad (16)$$

Here \mathbf{Q}^* and \mathbf{R}^* are spectral density matrices corresponding to plant noise and measurement noise, respectively. For seismic excitation $\mathbf{Q}^* = [Q^*]$, a scalar. Measurement noise is assumed identical for all sensors, i.e., $\mathbf{R}^* = R^*\mathbf{I}$, where \mathbf{I} is the identity matrix. $Q^*/R^* = 50$ is considered.⁸ The optimal state feedback control is obtained by minimizing the quadratic performance index (PI) $J^* = \frac{1}{2} \int_0^\infty [\mathbf{z}^T\mathbf{Q}\mathbf{z} + \mathbf{f}_d^T\mathbf{R}\mathbf{f}_d]dt$. Here, \mathbf{Q} is the positive semi-definite state weighting matrix and \mathbf{R} is the positive definite control force weighting matrix. The minimization, subject to state equations as constraint (i.e., Eq. (5) without external excitation term), yields the desired control force as

$$\mathbf{f}_d = -\mathbf{R}^{-1}\mathbf{B}^T\mathbf{P}\hat{\mathbf{z}} = -\mathbf{K}\hat{\mathbf{z}}; \quad (17)$$

where estimated states, $\hat{\mathbf{z}}$, are used in place of unmeasurable states, \mathbf{z} , and \mathbf{P} is the solution of the algebraic Riccati equation

$$\mathbf{A}^T\mathbf{P} + \mathbf{P}\mathbf{A} - \mathbf{P}\mathbf{B}\mathbf{R}^{-1}\mathbf{B}^T\mathbf{P} + \mathbf{Q} = \mathbf{0}. \quad (18)$$

3.2. OSOF Control

The desired control input is obtained based on measured output feedback instead of full state feedback as done in LQR/LQG control. Thus, OSOF control, like LQG, uses fewer sensors than LQR. However OSOF, unlike LQG, dispenses with observer design. Thus OSOF requires less CPU time (due to fewer on-line computations) as compared to LQG.

The system dynamics represented by state equations (without plant noise, i.e., external excitation), the control input obtained by output feedback (i.e., desired damper force \mathbf{f}_d), and the measured output \mathbf{y} considered as a combination of states only (i.e., without feed-through $\mathbf{D}_1\mathbf{f}$ and measurement noise \mathbf{v}), are given as²⁰

$$\dot{\mathbf{z}} = \mathbf{A}\mathbf{z} + \mathbf{B}\mathbf{f}_d; \quad \mathbf{f}_d = -\mathbf{K}\mathbf{y}; \quad \mathbf{y} = \mathbf{C}\mathbf{z}. \quad (19)$$

The matrix of constant feedback gains \mathbf{K} (and hence control input \mathbf{f}_d) is determined by minimizing the PI, J^* , subject to closed loop dynamics, Eq. (19), as constraint. In general, if the controller is effective for random initial conditions, it is also effective for random input excitations.²¹ The closed loop system matrix is $\mathbf{A}_c = \mathbf{A} - \mathbf{B}\mathbf{K}\mathbf{C}$. For asymptotically stable \mathbf{A}_c ,

it can be shown that $J^* = \frac{1}{2}\text{tr}(\mathbf{P}\hat{\mathbf{Q}})$, where $\hat{\mathbf{Q}} = \mathbf{z}(0)\mathbf{z}^T(0)$. Minimizing J^* yields the design equations²⁰

$$\mathbf{A}_c^T\mathbf{P} + \mathbf{P}\mathbf{A}_c + \mathbf{C}^T\mathbf{K}^T\mathbf{R}\mathbf{K}\mathbf{C} + \mathbf{Q} = \mathbf{0}; \quad (20)$$

$$\mathbf{A}_c\mathbf{S} + \mathbf{S}\mathbf{A}_c^T + \tilde{\mathbf{Q}} = \mathbf{0}; \quad (21)$$

$$\mathbf{R}^{-1}\mathbf{B}^T\mathbf{P}\mathbf{S}\mathbf{C}^T(\mathbf{C}\mathbf{S}\mathbf{C}^T)^{-1} = \mathbf{K}; \quad (22)$$

with unknowns \mathbf{P} (symmetric, positive semi-definite), \mathbf{S} (matrix of Lagrange multipliers), and \mathbf{K} (optimal gain). The dependency on initial states is eliminated by minimizing the expected value of PI instead of PI itself.²² For uncorrelated initial states, $E\{\hat{\mathbf{Q}}\} = \mathbf{I}$, the identity matrix, and the optimal cost is $E\{J^*\} = J = \frac{1}{2}\text{tr}[\mathbf{P}]$. The Moerder-Calise algorithm,²³ converging to a local minimum of J , is used to solve Eqs. (20)–(22) as follows:

Step 1: For iteration counter $k = 0$, initial gain \mathbf{K}_0 is chosen such that \mathbf{A}_c is asymptotically stable. $\mathbf{K}_0 = \mathbf{0}$ is chosen since \mathbf{A} is stable.

Step 2: $\mathbf{A}_k \leftarrow (\mathbf{A} - \mathbf{B}\mathbf{K}_k\mathbf{C})$, $\mathbf{A}_c \leftarrow \mathbf{A}_k$, $\mathbf{K} \leftarrow \mathbf{K}_k$. Solve Eqs. (20) and (21) for \mathbf{P} and \mathbf{S} . Then $\mathbf{P}_k \leftarrow \mathbf{P}$, $\mathbf{S}_k \leftarrow \mathbf{S}$, $J_k = \frac{1}{2}\text{tr}[\mathbf{P}_k]$. If $k > 0$ and $|J_k - J_{k-1}| < \varepsilon$, where ε is a small tolerance, the algorithm has converged, go to Step 4.

Step 3: $\mathbf{K}_{k+1} \leftarrow \mathbf{K}_k + \alpha\Delta\mathbf{K}$, where $\Delta\mathbf{K} = \mathbf{R}^{-1}\mathbf{B}^T\mathbf{P}_k\mathbf{S}_k\mathbf{C}^T(\mathbf{C}\mathbf{S}_k\mathbf{C}^T)^{-1} - \mathbf{K}_k$ and α is chosen such that \mathbf{A}_{k+1} is asymptotically stable, where $\mathbf{A}_{k+1} \leftarrow (\mathbf{A} - \mathbf{B}\mathbf{K}_{k+1}\mathbf{C})$. $k \leftarrow k + 1$. Go to Step 2.

Step 4: $\mathbf{K} = \mathbf{K}_k$.

When using acceleration feedback, as done here, the measured output and the desired control input obtained from output feedback are

$$\hat{\mathbf{y}} = \mathbf{C}\mathbf{z} + \mathbf{D}_1\mathbf{f}_d; \quad \mathbf{f}_d = -\mathbf{K}\hat{\mathbf{y}}; \quad (23)$$

which yields

$$\mathbf{f}_d = -(\mathbf{I} + \mathbf{K}\mathbf{D}_1)^{-1}\mathbf{K}\mathbf{y} = -\hat{\mathbf{K}}\mathbf{y}. \quad (24)$$

Thus, $\hat{\mathbf{K}}$ is determined using the Moerder-Calise algorithm,²³ and \mathbf{K} is obtained as

$$\mathbf{K} = \hat{\mathbf{K}}(\mathbf{I} - \mathbf{D}_1\hat{\mathbf{K}})^{-1} \quad (25)$$

for controller implementation. This modification is necessary when using acceleration output feedback, instead of only displacement and velocity feedback for determining the desired control input \mathbf{f}_d . A single damper is considered. Hence $\mathbf{f}_d = [f_d]$ and $\mathbf{R} = [R]$ are scalars in LQG/OSOF controller design.

3.3. Clipped Voltage Law (CVL)

Using f_d and f , the command voltage, v , to the damper is obtained as follows.⁸ If $f_d f < 0$, then $v = v_{\min} = 0$ V; else $v = v_{\max} = 2.25$ V when $|f_d| > |f|$, or $v = v_{\min} = 0$ V when $|f_d| < |f|$, or v is held at its present value when $f_d = f$. Here f_d is the desired damper force obtained from the controller (Eq. (17) for LQG / Eq. (19b) for OSOF), and f is the applied damper force (Eq. (7)). Thus, saturation voltage (v_{\max})

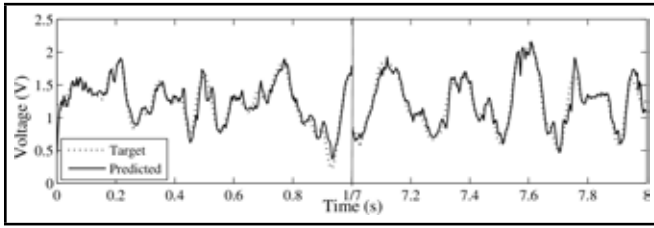


Figure 4. Target and predicted voltages, training data.

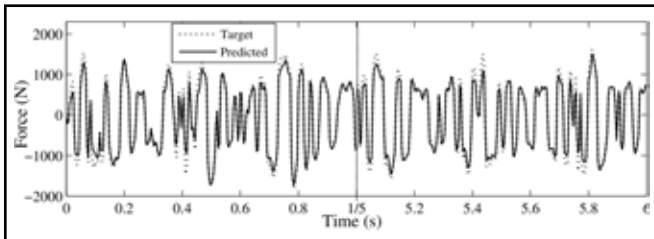


Figure 5. Target and predicted forces, validation data III.

where $z_u = \pm (A/(\gamma + \beta))^{\frac{1}{n}}$ are the limits of z_d obtained from Eq. (9). Here, $x^* = z_8 - z_3$ and $\dot{x}^* = z_{16} - z_{11}$, i.e., relative displacement and relative velocity of the damper, respectively. Equation (28) yields limiting straight lines (in $f-\dot{x}^*$ plane) when $v = 0$ V and $v = 2.25$ V, for which the damper force is minimum (f_{min}) and maximum (f_{max}), respectively. The region between these straight lines is the realizable zone. This lies in the first and third quadrants for positive and negative values, respectively, of z_u . The desired force, f_d , obtained from LQG/OSOF control, and the measured relative velocity \dot{x}^* , are provided to the MR constraint filter, which then generates the command voltage as follows:

- i) If $\dot{x}^* f_d > 0$ and f_d lies outside the realizable zone, then the control voltage is set to the appropriate limiting value. Thus, if $|f_d| > |f_{max}|$, then $v = v_{max} = 2.25$ V, else if $|f_d| < |f_{min}|$, then $v = v_{min} = 0$ V.
- ii) If $\dot{x}^* f_d > 0$ and f_d lies within the realizable region, i.e., $|f_{min}| \leq |f_d| \leq |f_{max}|$, then the control voltage to be applied is obtained from the RNN model. The inputs to the RNN are $f_d(t)$, $x^*(t)$, and the time histories of f (actual damper force), x^* (relative displacement), and v (applied voltage), i.e., as per Eq. (27).
- iii) If $\dot{x}^* f_d < 0$ then $v = v_{min} = 0$ V.

3.5. Controller Implementation

The schematic for actual implementation and simulation of LQG/OSOF control using RNN/CVL is shown in Fig. 2. Structure and MR damper equations (comprising the plant) are integrated using applied voltage v and states (z, y, z_d, u) at the beginning of each time step. The applied damper force f , computed via Eq. (7), and the states are thus obtained at the end of each time step. Measured outputs (y , damper relative displacement x^* , and damper relative velocity \dot{x}^*) are then obtained as shown and fed to the controller along with measured f . For LQG control, the desired damper force f_d is computed based on estimated states (obtained by integrating the observer, using measured outputs and the damper force as inputs to the observer). For OSOF control, f_d is computed directly using measured outputs. Then f_d and all measured quantities are fed

Table 1. Sensor configurations.

Storey	Sensor Configuration (o Accelerometer x LVDT)							
	8A,11D	8A	5A	3A	1A,21D	1A	51D	31D
3b	o	o	o	o			x	
2b	o	o	o					
1b	o	o	o		x		x	x
5a	o	o	o	o	o	o	x	
4a	o	o	o					
3a	ox	o	o	o			x	x
2a	o	o						
1a	o	o			x		x	x

to the CVL/RNN control laws to obtain v at the start of the next time step. Measured quantities are f for CVL, and f, x^*, \dot{x}^* for RNN. Although x^*, \dot{x}^* are measured outputs, they are not included in y since they are not used to obtain f_d herein. However, this does not preclude them from being part of y in future applications.

Thus, both OSOF-RNN and LQG-RNN require measurements of the same quantities, i.e., f, x^*, \dot{x}^* , and y , for their implementation. However, OSOF-RNN dispenses with the observer dynamics since it is based on direct output feedback, whereas LQG-RNN requires the time-intensive online-simulation of observer dynamics since it is based on the feedback of all estimated states. The on-line CPU times required for both controllers are compared in section 4.1.

4. RESULTS AND DISCUSSIONS

The mass, damping and stiffness coefficients (Fig. 1) considered are: $m_{1a} = m_{2a} = m_{1b} = m_{2b} = m_{3b} = 100$ kg, $m_{3a} = 95$ kg, $m_{4a} = m_{5a} = 90$ kg; $c_{1a} = 125$ Ns/m, $c_{2a} = c_{3a} = c_{4a} = c_{5a} = c_{2b} = c_{3b} = 50$ Ns/m; $c_{1b} = 100$ Ns/m; $k_{1a} = 1.7 \times 10^{06}$ N/m, $k_{2a} = k_{3a} = k_{4a} = k_{5a} = 2.9 \times 10^6$ N/m, $k_{1b} = 3.3 \times 10^6$ N/m, $k_{2b} = k_{3b} = 4.25 \times 10^6$ N/m; $c_c = 10$ Ns/m; $k_c = 100$ N/m. These are adapted from the experimental model of Dyke et al.⁸ so as to yield natural frequencies that are well separated, i.e., 7.13, 21.16, 34.74, 45.79, 53.17 Hz for B5 and 13.56, 39.24, 58.46 Hz for B3.

Equation (5) and Eqs. (7)–(10) are integrated for zero initial conditions using MATLAB ode45. The N-S component of the El-Centro ground motion data measured at Imperial Valley is used after suitable time-scaling.⁸ The following responses are obtained: (i) Uncontrolled, i.e., without coupler; (ii) Passive-off control, i.e., with applied voltage $v = 0$ V; (iii) Passive-on control with $v = v_{max} = 2.25$ V (damper saturation voltage); (iv) Semi-active control using LQG-CVL, LQG-RNN, OSOF-CVL, and OSOF-RNN controllers.

Various sensor configurations (Table 1) using accelerometers (o) and LVDT sensors (x) have been considered in order to obtain a well-distributed measurement of response for feedback to the controller. Various state weightings Q (Table 2), and control weightings R in the interval $[10^{-16}, 10^{01}]$, have been considered in order to achieve better control.

4.1. Controller Evaluation

Performance criteria defined by Ohtori et al. are evaluated.²⁴ Quantities J_1-J_8 are controlled responses normalized with the corresponding uncontrolled response. The responses considered are: Maximum peak displacement, J_1 ; Maximum peak interstorey drift, J_2 ; Maximum peak absolute acceleration, J_3 ; Peak base shear of the combined system, J_4 ; Maximum RMS

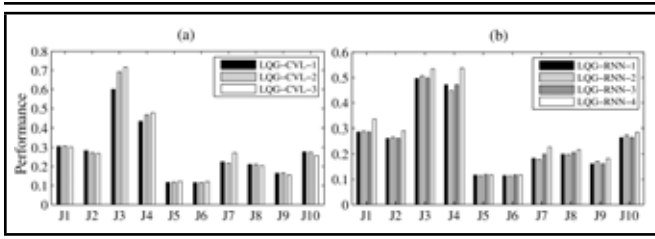


Figure 6. Performance criteria for effective controllers: (a) LQG-CVL, (b) LQG-RNN.

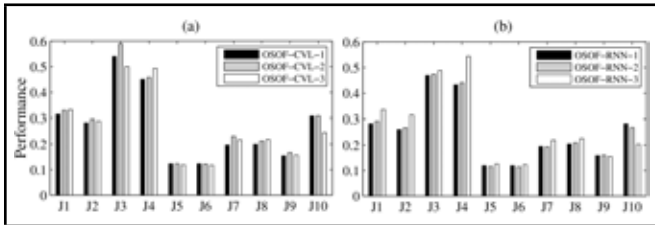


Figure 7. Performance criteria for effective controllers: (a) OSOF-CVL, (b) OSOF-RNN.

displacement, J_5 ; Maximum RMS interstorey drift, J_6 ; Maximum RMS acceleration, J_7 ; RMS base shear of the combined system, J_8 . J_9 is the maximum peak damper force normalized with the combined weight of the connected buildings. J_{10} is the maximum peak damper stroke normalized with the maximum peak uncontrolled displacement. The maximum for $J_1, J_2, J_3, J_5, J_6, J_7$, is taken across all storeys of the interconnected system. For J_9 and J_{10} , the maximum is taken across all dampers. A single damper is considered in the present case. Lower values of the performance criteria corresponds to better control.

Since earthquake induced vibrations occur for small durations, their control is essential mainly for maintaining structural integrity. Hence, interstorey drift and base shear are more critical than displacement and acceleration. Further, base shear is more critical than interstorey drift, since controlling the former is essential for maintaining the integrity of the overall structure. Hence, the indices based on peak values are ranked (J_4, J_2, J_3, J_1), and those based on RMS values are ranked (J_8, J_6, J_7, J_5) in decreasing order of importance. Low values of damper force and stroke imply less power expended for control. Hence, J_9 and J_{10} are also important in determining control effectiveness.

J_1 – J_{10} for effective controllers, obtained by varying sensor configurations, state weighting and control weighting, as shown in Tables 1 and 2, are compared in Fig. 6 and Fig. 7. The controllers are labeled LQG-CVL-1(8A, $Q_2, R = 10^{-11}$), LQG-CVL-2(3A, $Q_2, 10^{-09}$), LQG-CVL-3(1A, $Q_2, 10^{-10}$); LQG-RNN-1(3A, $Q_2, 10^{-08}$), LQG-RNN-2(8A, IID, $Q_2, 0.5 \times 10^{-08}$), LQG-RNN-3(1A, $Q_2, 10^{-08}$), LQG-RNN-4(5ID, $Q_5, 10^{-14}$); OSOF-CVL-1(5A, $Q_3, 10^{-06}$), OSOF-CVL-2(8A, IID, $Q_1, 10^{-04}$), OSOF-CVL-3(8A, 8ID, $Q_4, 0.5 \times 10^{-11}$); OSOF-RNN-1(5ID, $Q_4, 10^{-13}$), OSOF-RNN-2(8A, IID, $Q_1, 0.75 \times 10^{-03}$), OSOF-RNN-3(8A, 8ID, $Q_4, 0.5 \times 10^{-11}$). It is concluded, from the values obtained for J_1 – J_{10} , that LQG-CVL-1, LQG-RNN-2, OSOF-CVL-1, OSOF-RNN-1 yield most effective control.

Amongst LQG-CVL controllers, LQG-CVL-1 is the most effective since it affords the lowest J_3, J_4, J_5, J_6, J_8 , with J_3 and J_4 being at least 15% and 7% lower, respectively, than the

Table 2. Response quantities weighted in PI, corresponding state weighting Q .

Notation	Response weighted	Q
Q_1	5a, 1b, accelerations	$C^T Q C$, $Q = \text{diag}[0 \ 0 \ 0 \ 0 \ 1 \ 20 \ 0 \ 0 \ 0]$
Q_2	all states	$I_{16 \times 16}$
Q_3	4a, 5a, 2b, accelerations	$C^T Q C$, $Q = \text{diag}[0 \ 0.06 \ 2.1 \ 0.1 \ 0]$
Q_4	5a, 1b, displacement	$O_{16 \times 16}$, except $Q_{5,5}=Q_{6,6}=1$
Q_5	5a, displacement	$O_{16 \times 16}$, except $Q_{5,5}=1$

Table 3. Peak base shear (N).

Building	Uncontrolled	Passive-Off	Passive-On	LQG		OSOF		LQR	
				CVL	RNN	CVL	RNN	CVL	RNN
B ₅	7116	2593	2695	2018	1868	2019	1856	2060	1908
B ₃	3907	1709	3721	2695	3005	2857	2876	2873	2801

LQG-CVL-2/LQG-CVL-3 controllers. Amongst LQG-RNN controllers, LQG-RNN-2 appears the most effective since it affords the lowest J_4, J_5, J_6, J_7, J_8 . However, LQG-RNN-1 is comparable to LQG-RNN-2, except J_4 for which it is 5% higher. Thus LQG-RNN-1 is chosen as the most effective controller since it requires fewer sensors than LQG-RNN-2 (i.e., 3A instead of 8A, IID). Note that LQG-RNN-3 is also comparable to LQG-RNN-1, except for J_7 and J_8 , i.e., it is possible to realize quite effective control using a single accelerometer feedback. LQG-RNN-4 is the least effective of the four LQG-RNN controllers.

Amongst OSOF-CVL controllers, OSOF-CVL-1 is the most effective. It affords the lowest $J_1, J_2, J_4, J_7, J_8, J_9$; and J_5, J_6 comparable to OSOF-CVL-2/OSOF-CVL-3; and J_3 8% lower [higher] than OSOF-CVL-2 [OSOF-CVL-3]. Amongst OSOF-RNN controllers, OSOF-RNN-1 and OSOF-RNN-2 yield comparable results, and both are better than OSOF-RNN-3. OSOF-RNN-1 requires fewer sensors than OSOF-RNN-2 (i.e., 5ID compared to 8A, IID), and it affords the lowest J_1, J_2, J_3, J_4, J_8 . Hence it is chosen as the most effective OSOF-RNN controller. Thus very effective control is possible using few sensors, as in LQG-RNN-1 (3A), OSOF-CVL-1 (5A), and OSOF-RNN-1 (5ID).

Henceforth only the most effective controllers, i.e., LQG-CVL-1, LQG-RNN-1, OSOF-CVL-1, and OSOF-RNN-1, selected on the basis of performance criteria J_1 – J_{10} and the effective usage of sensors, are considered. They are denoted LQG-CVL, LQG-RNN, OSOF-CVL, OSOF-RNN. Online CPU time required by LQG-CVL, LQG-RNN is 22.12 s, 30.15 s, and for OSOF-CVL, OSOF-RNN it is 1.76 s, 2.96 s, respectively. Thus, time taken by OSOF controllers is an order of magnitude less than LQG controllers. This is expected since OSOF, unlike LQG, dispenses with running observer dynamics for state estimation.

Peak base shear for various controllers (including the four most-effective semiactive LQG/OSOF controllers) is shown in Table 3. Reduction, vis-a-vis passive-on control, in peak base shear of building B5[B3] is 25%[28%] with LQG-CVL, 31%[19%] with LQG-RNN, 25%[23%] with OSOF-CVL, and 31%[23%] with OSOF-RNN. Thus all four semiactive controllers provide considerable reduction in peak base shear vis-a-vis passive-on control, with the RNN controllers being more effective in reducing the peak base shear of B5. Semiactive and passive-on controllers result in a re-distribution of base shear from flexible B5 to stiffer B3, thus yielding a higher base shear

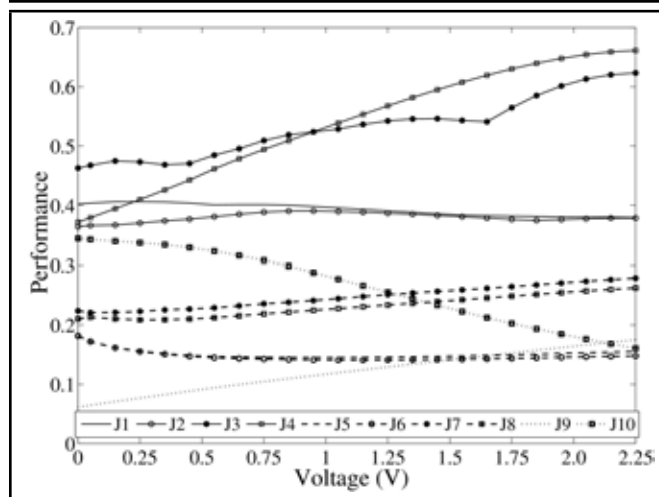


Figure 8. Performance of passive controllers versus applied voltage.

for B3 compared to B5. This is re-confirmed from storeywise acceleration responses in Fig. 12. Although passive-off control provides the lowest maximum peak base shear, it is unable to re-distribute it to the stiffer building.

Performance criteria for passive controllers are shown in Fig. 8. The constant applied voltage is varied in the range $[0, 2.25]$ V. The performance criteria increase/decrease almost monotonically with voltage, i.e., there is no distinct minima indicating an optimal passive-on voltage. J_1 and J_{10} are minimum for passive-on with saturation voltage (2.25 V). J_2 , J_3 , J_4 , and J_9 are minimum for passive-off (0 V). J_7 and J_8 are minimum for 0.05 V and 0.25 V, respectively (i.e., almost passive-off voltage), their minimum values being respectively 2% and 1% lower than the corresponding passive-off values. J_5 and J_6 are minimum for 0.95 V and 1.15 V, respectively, their minimum values being respectively 7% and 5% lower than the corresponding passive-on values. If $v = 1.05$ V is chosen as the optimal passive-on voltage, the performance indices J_3 – J_9 reduce by 15%, 19%, 7%, 5%, 12%, 13%, and 32%, respectively, compared to the passive-on values. However, in that case, the passive-on controller is quite ineffective in re-distributing base shear to B3, i.e., it acts almost like the passive-off controller. Thus, for future comparisons, passive-on control is considered with the saturation voltage (2.25 V) applied.

4.2. Peak/RMS Response

Maximum and storeywise values of peak/RMS responses are compared (the maximum across all storeys of the connected system is considered). The maximum drifts and displacements occur in B5, at storey one and five, respectively, for all controllers. Maximum accelerations occur at storey-five B5 for uncontrolled and passive control, and at different storeys of B3/B5 for semiactive control.

Performance criteria are shown in Fig. 9 for passive controllers and the most effective LQG/OSOF/LQR semiactive controllers. Figure 9 shows that passive controllers yield 37–62% reduction in max-peak responses and 72–85% reduction in max-RMS responses, when compared with the uncontrolled case. Compared to passive-off control, passive-on control provides comparable max-peak drift/displacement and at least 15% reduction in the corresponding max-RMS values,

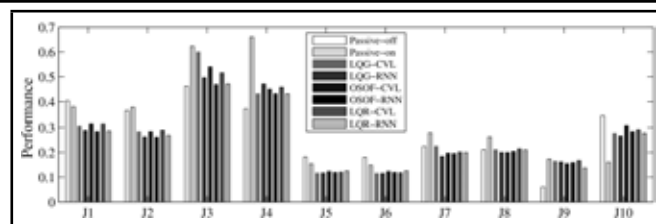


Figure 9. Performance of passive and semiactive LQG/OSOF controllers.

but an increase of 35%/25% in max-peak/max-RMS acceleration. Thus passive-on control is effective in drift/displacement control, but very ineffective in attenuating accelerations, vis-a-vis passive-off control. This is also evident from storeywise responses in Figs. 10–12.

For LQG/OSOF semiactive control, Fig. 9 shows that the RNN controllers outperform the corresponding CVL ones. Thus only LQG-RNN and OSOF-RNN are chosen for further comparisons.

Passive-off versus LQG/OSOF semiactive control

Figure 9 shows that the overall performance of LQG-RNN/OSOF-RNN semiactive controllers is superior to passive-off control. However, passive-off control provides the lowest max-peak acceleration, peak base shear, and peak damper force. Note that passive-off control does not reduce the base shear in the flexible building (B5) by re-distributing it to the stiffer building (B3). Compared to passive-off control, LQG-RNN/OSOF-RNN afford: a reduction of 28–30% in max-peak displacement/drift, but an increase of up to 7% in max-peak accelerations; a reduction of 34–36% in max-RMS displacement/drift, and 13–18% in max-RMS acceleration. Thus, compared to passive-off control, LQG/OSOF control is very effective except for max-peak accelerations, which increase slightly. Figures 10–12 show that compared to passive off control, LQG/OSOF provide an attenuation of the storeywise responses of B5 but not B3.

Passive-on versus LQG/OSOF semiactive control

Figure 9 shows that, except for the damper stroke, passive-on control performs the worst. Compared to passive-on control, LQG-RNN/OSOF-RNN afford a reduction of: 24% in max-peak displacement, 31% in max-peak drift, and 20–25% in max-peak acceleration; 23–25%, 19–22%, and 30–34%, in the corresponding max-RMS values; and 7–8% in peak damper force. Simulations show that LQG-RNN/OSOF-RNN also yield a reduction of around 36% in RMS damper forces compared to passive-on control. Thus the LQG/OSOF controllers require less control effort and provide better response attenuation, i.e., they are very effective compared to passive-on control.

Figures 10, 11, and 12 show storeywise comparison of displacement, drift, and acceleration. The LQG-RNN and OSOF-RNN controllers yield comparable peak drifts, with the former somewhat better for RMS drifts. They yield substantial reduction in drift vis-a-vis passive-on control (reduction of up to 41% in peak drift and 38% in RMS drift). Attenuations for B5 are somewhat higher than for B3. They also outperform passive-on control in displacement control (reduction of 19–31% in peak displacement and 15–32% in RMS displacement). When compared to passive-on control, LQG/OSOF attenuate peak acceleration by 23–55% and RMS acceleration

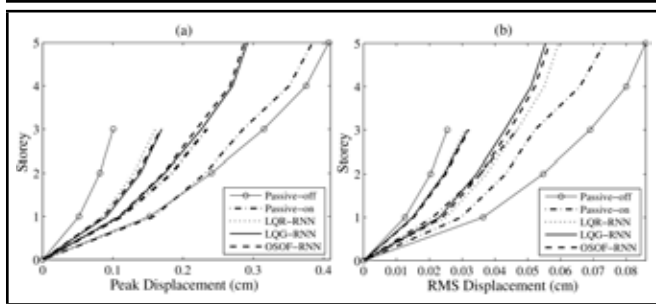


Figure 10. Storey displacements: (a) Peak, (b) RMS.

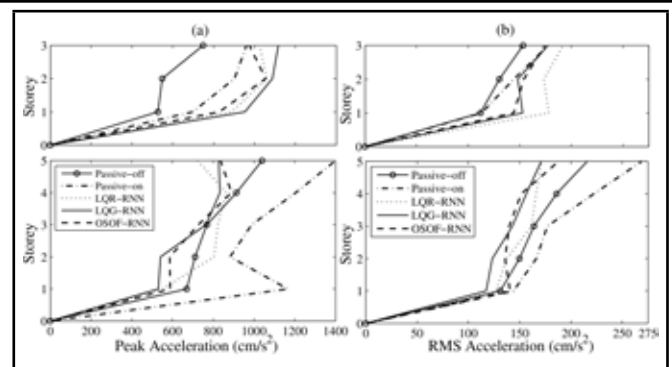


Figure 12. Storey accelerations: (a) Peak, (b) RMS.

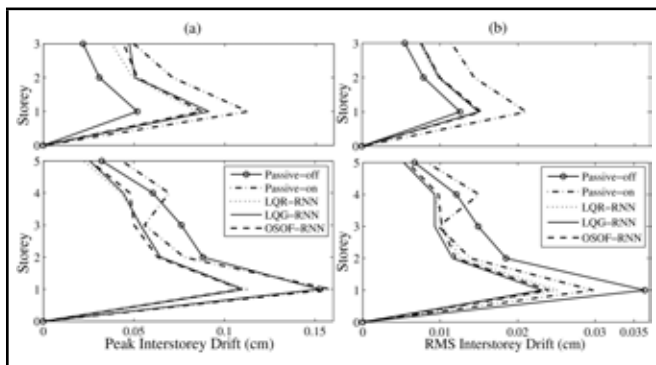


Figure 11. Interstorey drifts: (a) Peak, (b) RMS.

by up to 36% across B5. However, there is an increase in peak and RMS accelerations across B3, i.e., up to 37% and 35%, respectively. Thus, semiactive LQG-RNN/OSOF-RNN controllers yield considerable attenuation in storeywise peak/RMS responses of both buildings, except accelerations of B3, which increase considerably.

Comparison of LQR/LQG/OSOF semiactive controllers

LQG/OSOF controllers require fewer sensors compared to LQR. The latter requires that all states be measured. Performance criteria in Fig. 9 show that LQR-RNN is either more effective or comparable vis-a-vis LQR-CVL. Various combinations of Q and R , as considered for LQG/OSOF, were also considered for LQR. The most effective LQR controllers, whose performance criteria are shown in Fig. 9, were obtained for ($Q_2, R = 0.5 \times 10^{-8}$) for LQR-CVL and ($Q_3, R = 0.25 \times 10^{-4}$) for LQR-RNN. Hence, LQG-RNN/OSOF-RNN/LQR-RNN controllers, being the most effective, are compared. They yield comparable max-peak responses, while LQG-RNN/OSOF-RNN yield up to 8% attenuation in max-RMS responses as compared to LQR-RNN. OSOF-RNN and LQR-RNN yield somewhat lower max-peak acceleration and peak base shear, as compared to LQG-RNN. LQR-RNN yields the lowest peak damper force amongst semiactive (and passive-on) controllers (Fig. 9).

LQG-RNN is now compared with LQR-RNN for storeywise responses. Figures 10–12 show that LQG-RNN is as effective or better in reducing RMS responses (especially accelerations) of B3/B5. It is also effective in reducing peak accelerations of B5 to some extent, but it is not effective in reducing peak drifts/accelerations of B3, vis-a-vis LQR-RNN. For B5 the peak-displacements and peak-drifts from LQG-RNN are comparable with LQR-RNN (except storey five where the peak-drift increases 14%). However, across B3 the peak-displacements increase 6–7% and the peak-drifts increase up

to 25%, when using LQG-RNN. Peak accelerations reduce up to 33% across B5 (except storey five where it increases 14%), but they increase up to 9% across B3. RMS-displacements reduce 7–8% and RMS-drifts reduce up to 10% across B5, and are comparable across B3. RMS accelerations reduce up to 12% across B5, and 8–15% across B3.

Next, OSOF-RNN is compared with LQR-RNN for storeywise responses. Figures 10–12 show that OSOF-RNN is more effective in reducing RMS-accelerations of B3 and to some extent peak-accelerations of B5, but it is somewhat less effective in reducing peak-drifts of B3. It is comparable to LQR-RNN for other peak/RMS responses. For B5 the peak-drifts lie within -7% (attenuation) and 15% (accentuation), and the RMS-drifts lie within -5% and 10% of LQR-RNN values. For B3, OSOF-RNN yields an increase of up to 17% in peak-drifts, while RMS-drifts are comparable to LQR-RNN. The peak/RMS displacements are comparable across B5 and B3. For B5 the peak-accelerations lie within -27% and 16% , and the RMS-accelerations lie within -13% and 11% of LQR-RNN values. For B3, OSOF-RNN yields an attenuation of up to 7% in peak-accelerations and 9–19% in RMS-accelerations.

Table 3 shows that all three semiactive controllers yield a comparable peak base shear (LQG-RNN is 7% higher than LQR-RNN for B3). The damper forces from LQG-RNN/OSOF-RNN are around 18% higher in peak value and 8% higher in RMS value when compared with LQR-RNN.

LQG-RNN and OSOF-RNN yield comparable max-peak/max-RMS responses (OSOF-RNN yields 6% lower[higher] max-peak[max-RMS] acceleration). They are now compared for storeywise responses. Figures 10–12 show that they yield comparable peak-displacements/peak-drifts. LQG-RNN yields somewhat lower RMS-displacements/RMS-drifts for B3/B5, and significantly lower peak/RMS accelerations for B5. OSOF-RNN yields a peak-drift between -6% to 8% higher and RMS-drift up to 10% higher, as compared to LQG-RNN. For B5, OSOF-RNN yields peak accelerations up to 11% higher and RMS accelerations up to 20% higher than LQG-RNN. For B3, OSOF-RNN attenuates peak accelerations up to 13%.

Summarizing, the three semiactive controllers are comparable in peak drift and peak displacement control. OSOF-RNN and LQG-RNN are somewhat more effective in the peak-acceleration control of B3 and B5, respectively. LQG-RNN is somewhat more effective in RMS response control. The three semiactive controllers yield comparable peak base shear, but the peak damper force is lower for LQR-RNN control. Thus, OSOF-RNN/LQG-RNN controllers are quite effective in

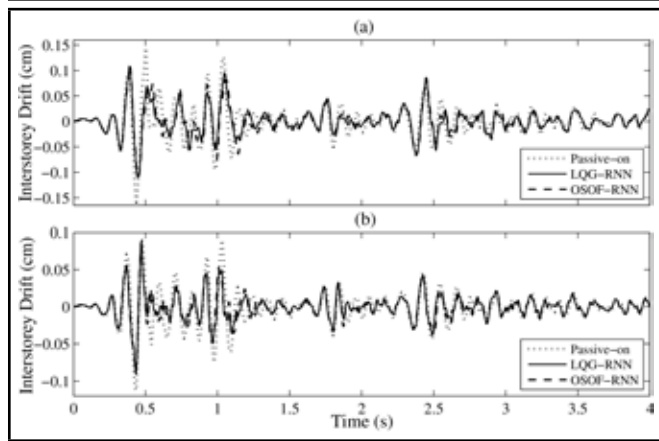


Figure 13. Time history of interstorey drift, storey-one: (a) B5, (b) B3.

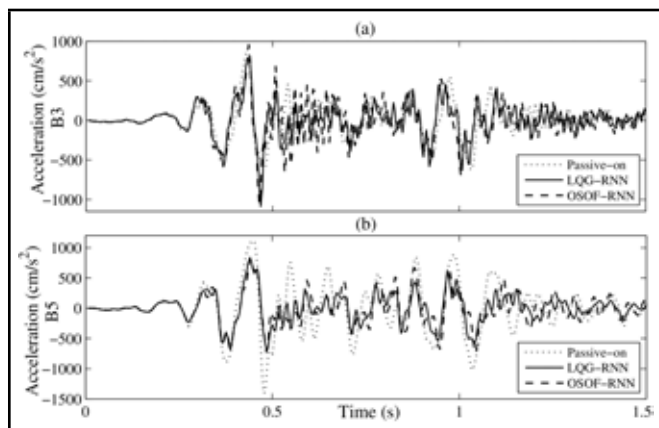


Figure 14. Time history of absolute acceleration: (a) Storey-two B3, (b) Storey-five B5.

attenuating storeywise/max-peak/max-RMS responses, when compared with LQR-RNN.

4.3. Time History

Figure 13 shows the time history of interstorey drift at storey-one B5 (where the max-peak/max-RMS drift occurs for all passive/semiactive controllers). The response at storey-one B3 is also shown. LQG-RNN and OSOF-RNN provide a significant control of drift, as seen by the early attenuation (i.e., for $t < 1.1s$), when compared with passive-on control. Figure 14 shows the time history of accelerations at storey-two B3 and storey-five B5 where max-peak acceleration occurs for OSOF-RNN and passive-on controllers, respectively (note that OSOF-RNN yields lower max-peak acceleration than LQG-RNN). It is clear that both semiactive controllers attenuate the acceleration of B5 but not B3.

Figure 15 shows the time history of applied voltage resulting from OSOF-RNN and OSOF-CVL controllers. The voltage is ‘off’ ($v = 0$) for around 81% of the duration and ‘on’ ($v = 2.25$ for CVL and $0 \leq v \leq 2.25$ for RNN) for the remainder. Thus the CVL and RNN semiactive controllers afford power savings while also providing effective control vis-a-vis passive-on control (for which the voltage is always ‘on’, $v = 2.25$ V).

The time history of applied and desired damper forces, resulting from LQG-RNN and OSOF-RNN, are compared in Fig. 16. Both semiactive controllers produce applied forces

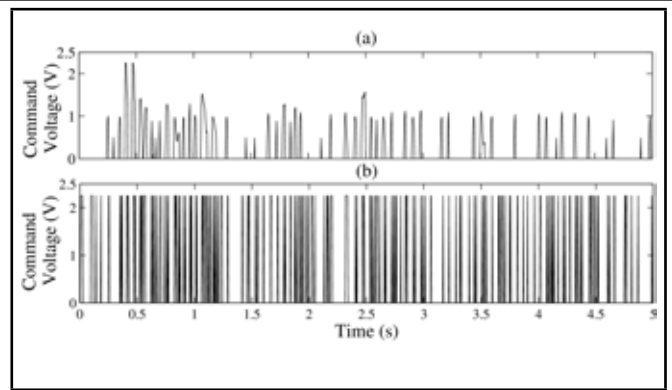


Figure 15. Time history of command voltage: (a) OSOF-RNN, (b) OSOF-CVL.

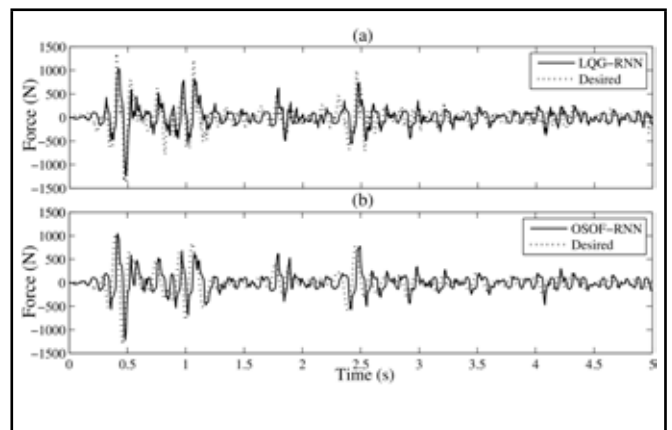


Figure 16. Time history of desired, applied damper forces: (a) LQG-RNN, (b) OSOF-RNN.

that closely follow the desired forces. The RMS of difference between the applied and desired forces is 278.12 N for OSOF-RNN and 231.89 N for LQG-RNN. The difference between applied and desired forces is mainly due to three reasons. Firstly, inverting damper dynamics (i.e., predicting the command voltage for a given force) is difficult. Thus one has to resort to ‘approximate’ voltage laws like CVL/RNN. Secondly, damper saturation occurs at $v = 2.25$ V. This limits the maximum damper force generated, irrespective of the force desired. Thirdly, the damper constitutive law (Eqs. (7)–(11)) yields applied-force versus velocity lying predominantly in the 1st and 3rd quadrants (Fig. 17(a) and Fig. 17(d)). However, LQG-RNN and OSOF-RNN controllers yield desired-force versus velocity lying in all quadrants (Fig. 17(b) and Fig. 17(e)). Hence desired forces in the 2nd and 4th quadrants are unrealizable. Thus, differences in applied and desired forces would occur even if a more accurate force-voltage law is devised. LQG-RNN appears somewhat better than OSOF-RNN in producing damper forces close to the desired ones (Fig. 17(c) and Fig. 17(f)).

4.4. Controller Effectiveness—Performance for Other Base Excitations

The results presented so far pertain to the El-Centro excitation. Now, in order to assess the effectiveness of the semiactive controllers, their performance is evaluated and compared with that of passive controllers for the following excitations: (i) Gaussian White Noise (GWN), (ii) Hachinohe—N-S

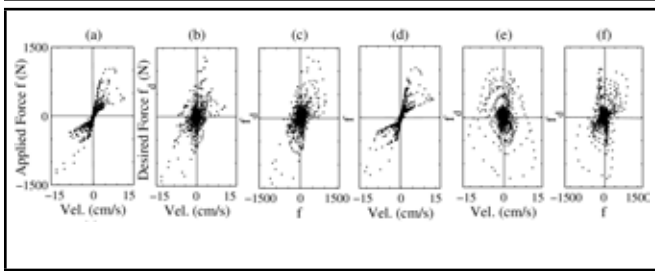


Figure 17. Applied/Desired force versus velocity: (a,b,c) LQG-RNN, (d,e,f) OSOF-RNN.

Table 4. Peak base shear (N).

Ground Excitation	Building	Uncontrolled	Passive-off	Passive-on	LQR-RNN	LQG-RNN	OSOF-RNN
GWN	B ₅	3034	1203	982	904	964	851
	B ₃	2817	923	1243	1088	1071	997
Hachinohe	B ₅	2534	643	562	559	579	486
	B ₃	596	567	720	596	589	599
Managua	B ₅	19597	5805	3924	3205	3121	3672
	B ₃	5383	2559	4682	3630	3543	3293
Northridge	B ₅	7100	3672	3427	3024	3013	3378
	B ₃	3691	2698	3463	2807	2711	2716
Kobe	B ₅	22416	8094	4897	5659	5873	6566
	B ₃	8873	6748	5505	5223	5076	5152

component, Japan, 1968, (iii) Managua, Nicaragua, 1972, (iv) Northridge—N-S component, Sylmar County Hospital, California, 1994, and (v) Kobe—N-S component, Kobe Japanese Meterological Agency station, 1995. The excitations in (ii)–(v) are time-scaled by a factor of 19.2, 2.6, 11, and 2.5, respectively, in order to excite the fundamental mode of the experimental building. The sensor configurations, state weighting Q , and control weighting R are considered the same as those obtained for the most effective controllers during the El-Centro study.

Table 4 shows the peak base shear obtained using passive controllers and semiactive controllers. The uncontrolled case generally yields the highest peak base shear. When compared to the passive controllers, the semiactive controllers mostly yield a lower peak base shear for the flexible building (B5). In fact, when compared with passive-on control, the semiactive controllers afford marginal to substantial reductions in peak base shear for both buildings, except for B5 in the case of the Kobe excitation. Semiactive and passive-on controllers mostly result in a re-distribution of base shear from B5 to B3. Passive-off control yields the lowest peak base shear for B3, except in the case of the Kobe excitation. However, it is unable to re-distribute the base shear.

The performance criteria obtained from the five controllers are shown in Fig. 18.

Max-peak displacement (J_1): Passive-off control is the least effective. Compared to passive-on control, the performance of semiactive controllers is 9–25% better for the El-Centro, Hachinohe, and Managua excitations, but 18–29% worse for the Kobe excitation. For the GWN and Northridge excitations, the performance of LQR-RNN/LQG-RNN is comparable with passive-on control, while that of OSOF-RNN is 11–15% worse than that of passive-on control.

Max-peak drift (J_2): Passive-off control is the least effective. Compared to passive-on control, the performance of

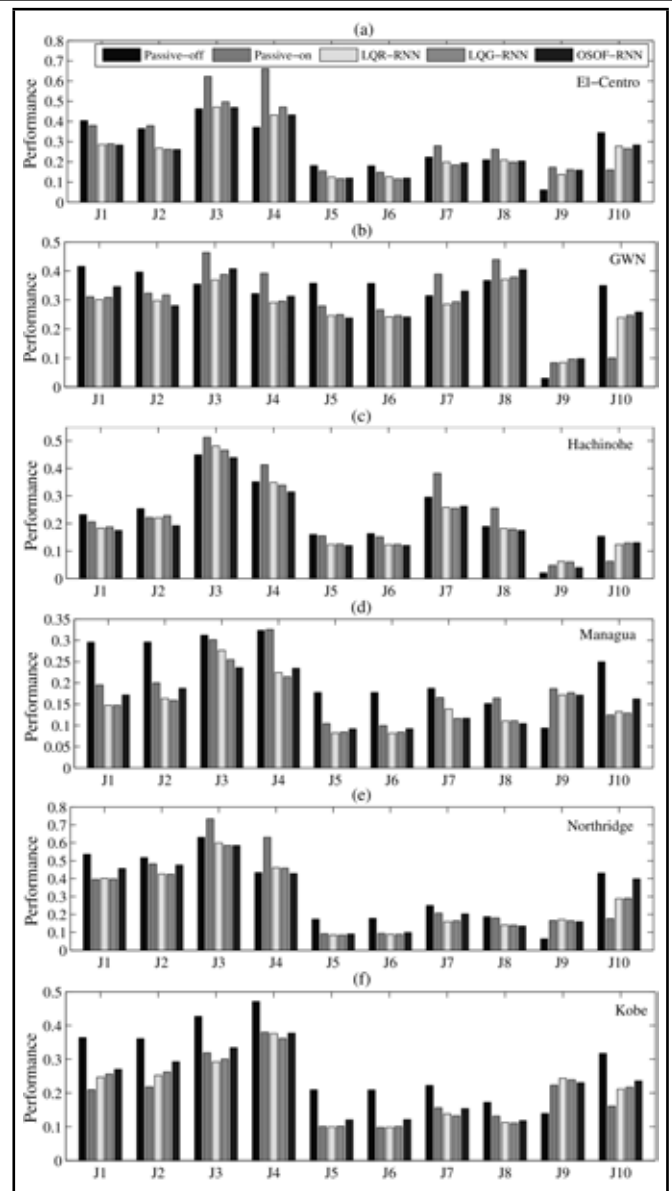


Figure 18. Performance of passive and semiactive controllers: (a) El-Centro, (b) Gaussian white noise (GWN), (c) Hachinohe, (d) Managua, (e) Northridge, and (f) Kobe excitations.

semiactive controllers is up to 31% better, except for the Kobe excitation for which it is 16–34% worse.

Max-peak acceleration (J_3): Passive-on is the least effective, except in the case of the Kobe excitation for which it is comparable to semiactive control. Compared to passive-off control, the performance of semiactive controllers is 6–31% better for the Managua, Northridge, and Kobe excitations, comparable for the El-Centro and Hachinohe excitations, but up to 15% worse for the GWN excitation.

Peak combined base shear (J_4): Passive-on is the least effective, except in the case of the Kobe excitation for which it is comparable to semiactive control. Compared to passive-off control, the performance of semiactive controllers is up to 34% better for GWN, Hachinohe, Managua, and Kobe excitations, comparable for the Northridge excitation, but 16–27% worse for the El-Centro excitation.

Max-RMS displacement (J_5): Passive-off control is the least effective. Compared to passive-on control, the performance of semiactive controllers is up to 24% better, except in the case of the Kobe excitation for which it is comparable when using LQR-RNN and LQG-RNN, but 20% worse when using OSOF-RNN.

Max-RMS drift (J_6): Passive-off control is the least effective. Compared to passive-on control, the performance of semiactive controllers is up to 22% better, except in the case of the Kobe excitation for which it is comparable when using LQR-RNN and LQG-RNN, but 24% worse when using OSOF-RNN.

Max-RMS acceleration (J_7): Semiactive controllers perform up to 40% better than passive-off control and up to 34% better than passive-on control.

RMS combined base shear (J_8): Passive-on is the least effective, except in the case of the Kobe excitation for which it is comparable to semiactive control. Compared to passive-off control, the performance of semiactive controllers is up to 36% better for the Hachinohe, Managua, Northridge, and Kobe excitations, comparable for the El-Centro excitation, but up to 10% worse for the GWN.

Peak damper force (J_9): As expected, passive-off control yields the lowest peak damper forces. However, it is unable to reduce the base shear of the flexible building B5 by redistributing it to the stiffer building B3. Passive-on control and semiactive controllers yield comparable peak damper forces.

Peak damper stroke (J_{10}): Passive-on control is the most effective in reducing the peak damper stroke, while passive-off control is the least effective in this regard.

Thus, for the range of ground excitations considered, the performance of semiactive controllers is generally superior to that of passive controllers. The exceptions are in the case of the Kobe excitation for which passive-on yields the lowest max-peak/max-RMS displacement/drift, the GWN excitation for which passive-off yields the lowest max-peak acceleration and RMS combined base shear, and the El-Centro excitation for which passive-off yields the lowest peak combined base shear. However, passive-off control is unable to redistribute the base shear from the flexible B5 to the stiffer B3. In general LQG-RNN performs somewhat better than OSOF-RNN.

5. CONCLUSIONS

Seismic control is studied for a five-storey flexible building coupled by an MR damper to a three-storey stiff building. LQG/OSOF control determines the desired damper force, following which CVL/RNN determine the command voltage required to produce this force. Various sensor configurations and state/control weightings are considered so as to obtain the most effective controllers on the basis of performance criteria J_1 – J_{10} . Semiactive and passive controllers are compared. This permits the following conclusions:

(i) When compared to passive-on control, LQG/OSOF provide a significant reduction in responses, base shear,

damper force, and ‘on’ duration of applied voltage. Only the storeywise accelerations of the B3 increase significantly, thus resulting in the re-distribution of base shear from the flexible to stiff building. Thus semiactive controllers require considerably less control effort and power and yet provide better response attenuation.

- (ii) Semiactive controllers using RNN outperform those using CVL. All three semiactive RNN controllers are comparable in max-peak response control (LQG-RNN yields somewhat higher max-peak accelerations). LQG-RNN/OSOF-RNN yield somewhat better attenuation (up to 8%) in max-RMS responses compared to LQR-RNN. Storeywise peak displacements/drifts are comparable across the three semiactive controllers. LQG-RNN, and to an extent OSOF-RNN, are more effective in attenuating storeywise peak-accelerations compared to LQR-RNN. LQG-RNN is the most effective in storeywise RMS response control. All three semiactive controllers yield a comparable peak base shear. LQG-RNN/OSOF-RNN require somewhat higher damper forces (peak value 18% higher than LQR-RNN) to achieve comparable control. Thus, using much fewer sensors, LQG-RNN/OSOF-RNN yield control that is as at least as effective as LQR-RNN, albeit by using a somewhat higher damper force.
- (iii) LQG-RNN and OSOF-RNN yield comparable max-peak/max-RMS responses and storeywise peak displacements/drifts. LQG-RNN yields somewhat lower storeywise RMS displacements/drifts than OSOF-RNN. For the flexible building, B5, LQG-RNN yields significantly lower peak/RMS accelerations, while for the stiffer building, B3, OSOF-RNN yields substantially lower peak accelerations. Both controllers yield comparable peak base shears. However, OSOF requires an order-of-magnitude lesser online computation time. Thus, both LQG-RNN and OSOF-RNN provide effective control, but OSOF-RNN is quicker.
- (iv) For the range of ground excitations considered, the performance of semiactive controllers is generally superior to that of passive controllers. However, in the case of Kobe excitation, passive-on yields the lowest max-peak/max-RMS displacement/drift. In general LQG-RNN performs somewhat better than OSOF-RNN.
- (v) Choice of feedback and state weighting is crucial in obtaining effective control. For example LQG-RNN with only drift feedback and Q_2 state weighting, or OSOF-RNN with only acceleration feedback and Q_4 state weighting, yield ineffective control since desired and applied forces have opposite signs, i.e., the desired force cannot be realized.
- (vi) Effective control is possible using few sensors. For example LQG-RNN with (8A,1ID), (3A), (1A), sensor configurations are comparable. Also, OSOF-RNN with (8A,1ID), (5ID), (5A) sensor configurations are comparable. Thus an effective controller can even be designed using a single accelerometer (at storey-five of B5).

REFERENCES

- ¹ Song, X., Ahmadian M., and Southward, S. C. Modelling magnetorheological dampers with application of nonparametric approach, *Journal of Intelligent Material Systems and Structures*, **16**, 421–432, (2005).
- ² Chang, C. C. and Zhou L. Neural network emulation of inverse dynamics for a magnetorheological damper, *Journal of Structural Engineering (ASCE)*, **128** (2), 231–239, (2002).
- ³ Spencer, B. F., Dyke, S. J., Sain, M. K., and Carlson, J. D. Phenomenological model for magnetorheological damper, *Journal of Engineering Mechanics (ASCE)*, **123** (3), 230–238, (1997).
- ⁴ Wang, L. X. and Kamath, H. Modelling hysteretic behavior in magnetorheological fluids and dampers using phase–transition theory, *Smart Materials and Structures*, **15**, 1725–1733, (2006).
- ⁵ Jimenez, R. and Alvarez-Icaza, L. LuGre friction model for a magnetorheological damper, *Structural Control and Health Monitoring*, **12**, 91–116, (2005).
- ⁶ Xu, Z. D. and Shen, Y. P. Intelligent bi-state control for the structure with magnetorheological dampers, *Journal of Intelligent Material Systems and Structures*, **14**, 35–42, (2003).
- ⁷ Xu, Z. D. and Guo, Y. Q. Neuro–fuzzy control strategy for earthquake-excited nonlinear magnetorheological structures, *Soil Dynamics and Earthquake Engineering*, **28**, 717–727, (2008).
- ⁸ Dyke, S. J., Spencer, B. F., Sain, M. K., and Carlson, J. D., Modelling and control of magnetorheological dampers for seismic response reduction, *Smart Materials and Structures*, **5** (5), 565–575, (1996).
- ⁹ Yuen, K. V., Shi, Y., Beck, J. L., and Lam, H. F. Structural protection using MR dampers with clipped robust reliability-based control, *Structural Multidisciplinary Optimization*, **34**, 431–443, (2007).
- ¹⁰ K-Karamodin, A. and H-Kazemi, H. Semiactive control of structures using neuro–predictive algorithm for MR dampers, *Structural Control and Health Monitoring*, **17**, 237–253, (2010).
- ¹¹ Bahar, A., Pozo, F., Acho, L., Rodellar, J., and Barbat, A. Hierarchical semiactive control of base-isolated structures using a new inverse model of magnetorheological dampers, *Computers and Structures*, **88**, 483–496, (2010).
- ¹² Aida, T. and Aso, T. Improvement of the structure damping performance by interconnection, *Journal of Sound and Vibration*, **242** (2), 333–353, (2001).
- ¹³ Ni, Y. Q., Liu, H. J., and Ko, J. M. Experimental investigation on seismic response control of adjacent buildings using semiactive MR dampers, *Proceedings of SPIE: Smart Structures and Materials*, **4696**, 334–344, (2002).
- ¹⁴ Zhu, H., Wen, Y., and Iemura, H. A study on interaction control for seismic response of parallel structures, *Computers and Structures*, **79**, 231–242, (2001).
- ¹⁵ Qu, W. L. and Xu, Y. L., Semiactive control of seismic response of tall buildings with podium structure using ER/MR dampers, *The Structural Design of Tall Buildings*, **10**, 179–192, (2001).
- ¹⁶ Xu, Y. L., Chen, J., Ng, C. L., and Qu, W. L. Semiactive seismic response control of buildings with podium structure, *Journal of Structural Engineering (ASCE)*, **131** (6), 890–899, (2005).
- ¹⁷ Jing, C., Youlin, X., Weilian, Q., and Zhilun, W. Seismic response control of a complex structure using multiple MR dampers: experimental investigation, *Earthquake Engineering and Engineering Vibration*, **3** (2), 181–193, (2004).
- ¹⁸ Christenson, R. E., Spencer, B. F., and Johnson, E. A. Semiactive connected control method for adjacent multidegree-of–freedom buildings, *Journal of Engineering Mechanics (ASCE)*, **133** (3), 290–298, (2007).
- ¹⁹ Cimellaro, G. P. and Lopez-Garcia, D. Algorithm for design of controlled motion of adjacent structures, *Structural Control and Health Monitoring*, **18**, 140–148, (2011).
- ²⁰ Lewis, F. L. and Syrmos, V. L. *Optimal Control*, Wiley, New York, 2nd ed., 359–370, 450–478, (1995).
- ²¹ Chu, S. Y., Soong, T. T., and Reinhorn, A. M. *Active, Hybrid and Semiactive Structural Control—A Design and Implementation Handbook*, Wiley, England, U.K., 183–184, (2005).
- ²² Levine, W. S. and Michael, A. On the determination of the optimal constant output feedback gains for linear multivariable systems, *IEEE Transactions on Automatic Control*, **AC-15** (1), 44–48, (1970).
- ²³ Moerder, D. D. and Calise, A. J. Convergence of a numerical algorithm for calculating optimal output feedback gains, *IEEE Transactions on Automatic Control*, **AC-30** (9), 900–903, (1985).
- ²⁴ Ohtori, Y., Christenson, R. E., Spencer, B. F., and Dyke, S. J. Benchmark control problems for seismically excited nonlinear buildings, *Journal of Engineering Mechanics (ASCE)*, **130** (4), 366–385, (2004).

Use of a New Modified Acoustic Model to Investigate Mean Flow Effects on Underwater Sound Sources

Mohammad Riahi, Norouz M. Nouri and Ali Valipour

Department of Mechanical Engineering, Iran University of Science and Technology, Narmak, Tehran, Iran, 1684613114

(Received 18 June 2013; revised: 17 October 2013; accepted: 28 October 2013)

In this investigation, by introducing a relatively comprehensive acoustic equations system, the possibility of a more precise time and spatial pattern for sound wave propagation in fluid was revealed. Since the conservation equation is known as a fundamental equation for obtaining the wave equation, initially, by using scale analysis, the differential terms and weight coefficients are converted into the dimensionless form. Then, by assuming the amplitudes of the sound sources are small and by utilizing the perturbation technique, these dimensionless equations are converted into different orders based on the order of acoustical fluctuations. Consequently, it was shown that the obtained first order equations are representative of acoustical equations. Also, the results are indicative of the first order equations being coupled with the leading order ones. Comparison of the obtained acoustic the equations of the present study are capable of considering velocity, viscosity, and density changes of the background fluid flow. In the end, the effects of the flow velocity with a different Mach number on the acoustical distribution pattern that stemmed from different sound sources have been studied for several benchmarks.

1. INTRODUCTION

The linear equation of the wave was founded on the basis of the linear constitutive theory in fluid mechanics and the assumption of sound waves with a small amplitude.¹ Linear constitutive theory of the fluid medium being used in the formulation of the linear equation of the wave includes the assumption of non-viscous and stationary background fluid flow with constant density. In light of these assumptions, linear wave equations in many fields of hydrodynamics and aerodynamics related to sound wave propagation are valid. Studies conducted on the noise generated by a hydrodynamic or aerodynamic occurrence in a time domain could be categorized into three groups.² The first group is based on the suggested acoustic analogy by Lighthill.³ The linear acoustic wave which is placed on the left side of the Lighthill model is capable of evaluating wave propagation under the effect of sound sources placed on the right side of model. Ffowcs Williams and Hawkins (FWH) extended this analogy by adding the effects of unsteady surface pressure.⁴ Seo and Salvator's studies are amongst those related to the FWH model in the investigation of the underwater propeller's noise.⁵⁻⁸ Although by using such models it is possible to identify patterns of wave propagation and directivity in the far field, this type of noise estimation methodology presents many assumptions such as those considered in linear acoustics, a low Mach number, and compressed sound sources.²

Another group of noise estimation viewpoints includes research utilizing Direct Numerical Simulation (DNS) to model and simulate the hydrodynamics of fluid with its acoustic

noise, directly and simultaneously. The advantage of using this method is in its limitless capability by which noise generated by all fluid flow such as a low Mach flow or a flow with a high Reynolds number could be obtained.² At the same time, scaled use in aerodynamics and hydrodynamics simulations have much difference with scaled use in acoustic simulation. This inequality of scales has caused the utilization of DNS in aerodynamic and hydrodynamic fields to be very difficult.⁹ Moreover, using the DNS method is very time consuming. Seo, et.al chose the DNS method to find the noise of the cloud cavitation.¹⁰ They used the compressible Navier-Stokes equations and a homogeneous equilibrium model based on fluctuating density to simulate noise generation in a flow field.

The third point of view is, in fact, a hybrid method between the two fields of hydrodynamics and acoustics or between the two fields of aerodynamics and acoustics. Some of these hybrid methods are formed based on dividing the flow field into compressible hydrodynamic and compressible acoustic perturbation equations (or Perturbed Euler Equations).¹¹⁻¹³ Seo and Moon present a set of revised Perturbed Euler Equations capable of calculating the effects of compressibility in the near field.¹⁴ They also developed a set of linearized, perturbed, compressible equations to overcome the occurred instability in numerical calculations caused by perturbed vorticity.^{9,15} Ewert and Schröder formulated several acoustic perturbation models based on the different sound sources derived from compressible flow simulation.³ They initially simulated the compressible flow and generated acoustic sources. Then on the basis of the type of formed sound sources, by using the suitable acous-

tic perturbation equation, they analysed the time and spatial wave propagation pattern. By using this hybrid method, Ewert also simulated the trailing edge noise of a propeller.¹⁶

Alongside studies mentioned thus far, some investigated the nonlinear effects caused by a high sound pressure level. Walsh and Torres presented a weak formulation of nonlinear acoustic equations.¹ They discretized and solved these governing equations by using the finite element method. Kuznetsov introduced classic wave equations containing the second order effects of nonlinearity.¹⁷ Söderholm has developed these equations by using the precise state equation.¹⁸ Also, Hoffelner, et al. demonstrated the effects of nonlinearity in high frequency such as ultrasonic increases, and as a result, considering these effects in high frequency is highly important.¹⁹

Considering the points discussed, in light of the need for the presentation of precise mathematical models for the estimation of sound wave propagation, in this investigation, attempts have been made to present a complete and, at the same time, precise model to estimate the time and spatial pattern of sound wave propagation. This has been done by decomposing the conservation equations of mass, momentum, and energy including the state equation of a different order. This order separation is based on the fluctuation of acoustic sources and is done by using the perturbation method. Hence initially, by utilizing scale analysis, differential terms, and their coefficients, equations of conservation are converted into a dimensionless form. Then, by assuming the amplitude of sound source fluctuations as very small and utilizing the perturbation method, equations would decompose into different orders based on the order of acoustic fluctuations. Results show that first order equations are coupled with leading order equations. Comparing the obtained acoustic model with linear acoustic equations reveals that the presented equations in this study are capable of considering velocity, viscosity, and density variations of the fluid flow and the effects on wave propagation. Finally, the effect of flow velocity with different Mach numbers on the pattern of wave propagation for different sound sources has been analysed and studied during several benchmarks.

2. MATHEMATICAL FORMULATION OF ACOUSTIC MODEL

Since acoustics are an ingredient of fluid flow dynamics, it would be possible to describe and model the sound radiated from different events in a fluid medium in addition to the hydrodynamics of them. This is done by using the governing conservation laws including conservation of mass, momentum, and energy for elementary particles of the fluid. Equations (1) through Eq. (3) represent general dimensional forms in the conservation of mass (continuity), momentum, and a combination of energy and state equations.²⁰

$$\frac{\partial \rho}{\partial t} + \nabla \cdot (\rho \vec{u}) = \rho Q; \quad (1)$$

$$\frac{\partial(\rho \vec{u})}{\partial t} + (\vec{u} \cdot \nabla)(\rho \vec{u}) = -\nabla p + \mu \left[\nabla^2 \vec{u} + \left(\left(\frac{1}{3} + \frac{\mu_v}{\mu} \right) \nabla(\text{div}(\vec{u})) \right) \right] + \rho \vec{u} Q; \quad (2)$$

$$\frac{\partial p}{\partial t} + (\vec{u} \cdot \nabla)p = c^2 [-\rho \text{div}(\vec{u})] + \left(\frac{c^2 \beta}{c_p} \right) \left[\mu_v (\nabla \cdot \vec{u})^2 + 2\mu \left\{ e_{ij} e_{ji} - \frac{1}{3} e_{ii}^2 \right\} \right]. \quad (3)$$

In these equations, $\rho(X, t)$ is the density, $\vec{u}(X, t)$ is the velocity, $Q(X, t)$ is the rate of fluid volume fluctuations, $p(X, t)$ is the pressure of fluid, μ is the viscosity, μ_v is the bulk viscosity, e_{ij} is the tensor of strain rate, c is the speed of sound, c_p is the heat capacity at constant pressure, T is the temperature, and $\beta = \frac{1}{\rho} \left(\frac{\partial \rho}{\partial T} \right)_{p_0}$ is the constant. Since in the present study the objective is to present an applied acoustic formulation for different problems in the fluid environment, it is necessary to convert all equations into a dimensionless form. In this way, depending on the problem, it is possible to disregard the less important terms by comparing the weight of each term.

2.1. Scale Analysis (Dimensional Analysis)

To make the governing equations dimensionless, the following relations are used:

$$p = \tilde{P} p^*; \quad \vec{u} = \tilde{U} \vec{u}^*; \quad \rho = \tilde{\rho} \rho^*; \quad t = \frac{t^*}{\tilde{\omega}}; \quad Q = \tilde{Q} Q^*; \\ X, Y, Z = \tilde{L} x, \tilde{L} y, \tilde{L} z \quad \Rightarrow \quad \nabla = \frac{\partial}{\partial x} = \frac{\partial}{\tilde{L} \partial x}. \quad (4)$$

In the above relations, terms containing the star index (*) are the order of one. Also, terms shown by the index of (~) are scale parameters in need of being selected from available physical parameters in the studied problem. Finally, by applying the above relations in Eq. (1) through Eq. (3), differential terms are made dimensionless. Then by conducting several mathematical operations, coefficients of these differential terms become dimensionless. Equation (5) through Eq. (7) are indicative of the dimensionless form of conservation equations.

$$St \frac{\partial \rho^*}{\partial t^*} + \nabla \cdot (\rho^* \vec{u}^*) = \left(\frac{L \tilde{Q}}{\tilde{U}} \right) \rho^* Q^*; \quad (5)$$

$$St \left[\frac{\partial(\rho^* \vec{u}^*)}{\partial t^*} \right] + [\vec{u}^* \nabla \cdot (\rho^* \vec{u}^*)] = Eu [-\nabla p^*] + \frac{1}{Re} \left[\nabla^2 \vec{u}^* + \left(\frac{1}{3} + \frac{\mu_v}{\mu} \right) (\nabla \text{div}(\vec{u}^*)) \right] + \left(\frac{L \tilde{Q}}{\tilde{U}} \right) \rho^* \vec{u}^* Q^*; \quad (6)$$

$$(St)(Eu) \left[\frac{\partial p^*}{\partial t^*} \right] + (Eu) [(\vec{u}^* \cdot \nabla)(p^*)] = \left(\frac{c}{\tilde{U}} \right)^2 [-\rho^* \text{div}(\vec{u}^*)] + \left(\frac{c^2 \beta}{c_p} \right) \left[\frac{1}{Re_v} (\nabla \cdot \vec{u}^*)^2 + \frac{1}{Re} 2 \left\{ e_{ij}^* e_{ji}^* - \frac{1}{3} e_{ii}^{*2} \right\} \right]; \quad (7)$$

where, (Re) , (St) , and (Eu) are Reynolds, Strouhal, and Euler dimensionless numbers. Now, in order to separate and decompose these equations that are dimensionless into two orders related to hydrodynamics and the acoustics of fluid flow, the Perturbation method will be used.

2.2. Decomposition of Governing Equations by Using the Perturbation Method

In light of the inequality between the time and spatial scales in the hydrodynamic solution of fluid flow with scales of its acoustic solution, using Direct Numerical Solution (DNS) in research for both aeroacoustics and hydroacoustics is very difficult and cumbersome. Moreover, using the DNS method is usually very time-consuming. On the other hand, considered assumptions in linear acoustics do not provide the possibility of considering effects like velocity, viscosity, and density changes of the background flow. Therefore, in the present study, it was attempted that by using the perturbation method, the governing equations of the hydrodynamics of flow became separated from equations governed in acoustics induced by that flow. Then, each one of these equations could be analysed and studied in the related computational domain.

In general, volume fluctuations in the fluid lead to the propagation of acoustic noise. On the other hand, the propagated sound waves from most phenomena in fluid with the exception of explosions or shock waves have fluctuations with small amplitude. Thus, it could be stated that the changes of volume sound sources in the fluid also have very small amplitude. The order of the governing equation in the acoustics of the fluid flow is from the same order of the volume fluctuations. So, if wave propagation in the fluid flow is viewed as the perturbation approach, then the order of the equations used in the modelling of the flow is much larger than the acoustic equations of the flow. As a result, by using the perturbation method and based on the order of acoustic fluctuations, conservation equations could be converted into different orders. In the perturbation method, the perturbed term is shown with (ε) . This term must be selected from the parameters of the considered problem. In light of the points mentioned and the objective of present research, which is separating equations on the basis of acoustic fluctuations, for the present study, $\varepsilon = \frac{Q\tilde{U}}{L}$ is considered. The following assumptions exist in equations:

$$\begin{aligned} p^*(X, t, \varepsilon) &= h_0(\varepsilon)p_0(X, t) + h_1(\varepsilon)p_1(X, t) + o(h_1(\varepsilon)); \\ \vec{u}^*(X, t, \varepsilon) &= f_0(\varepsilon)\vec{u}_0(X, t) + f_1(\varepsilon)\vec{u}_1(X, t) + o(f_1(\varepsilon)); \\ \rho^*(X, t, \varepsilon) &= g_0(\varepsilon)\rho_0(X, t) + g_1(\varepsilon)\rho_1(X, t) + o(g_1(\varepsilon)); \\ Q^*(X, t, \varepsilon) &= m_0(\varepsilon)Q_0(X, t) + m_1(\varepsilon)Q_1(X, t) + o(m_1(\varepsilon)). \end{aligned} \quad (8)$$

In these relations, p_0 , \vec{u}_0 , ρ_0 , Q_0 are dimensionless forms of pressure, velocity, density, and volume fluctuations in the leading order. Moreover, p_1 , \vec{u}_1 , ρ_1 , Q_1 are dimensionless forms of pressure, velocity, density, and volume fluctuations in the first order. Terms $h_0, h_1, \dots, m_0, m_1$ are indicative of the weight

of dimensionless parameters. On the basis of the above definitions, in this study, only the separating of the equations in the two orders of the leading and the first order has taken place. After placing the relationships of Eq. (8) into Eq. (5) through Eq. (7), the resulting equations need to be decomposed into different orders. This calls for obtaining the relationships of each of the weighting terms $(h_0, h_1, \dots, m_0, m_1)$ with the perturbed parameter (ε) from the stand point of order. Also, it needs to be considered that based on the applied definition in this study, it is presumed that the leading order equations must satisfy the conditions governing flow dynamics, and the first order equations must satisfy the conditions governing the acoustics of flow. In other words, relations between weighting terms of dimensionless parameters and perturbed terms have to be obtained such that after the decomposition of equations in different orders, the leading order equations can be capable of solving the flow field precisely. Moreover, the obtained first order equations should be indicative of linear wave equations after applying assumptions of linear acoustics (including non-viscos and static fluid). Alongside these points, the definition of $x_{n+1}(\varepsilon) = o(x_n(\varepsilon))$ and the concept of minimum possible conditions has been used. Eventually, after simplification, the only condition agreeable with the physical parameters of velocity, density, pressure, and volume source fluctuations would be obtained as following:

$$\begin{aligned} p^* &= p_0 + \varepsilon p_1; \\ \vec{u}^* &= \vec{u}_0 + \varepsilon \vec{u}_1; \\ \rho^* &= \rho_0 + \varepsilon \rho_1; \\ Q^* &= Q_0 + \varepsilon Q_1. \end{aligned} \quad (9)$$

Finally, these forms of parameters are applied in Eq. (5) through Eq. (7). Then, the obtained equations would be decomposed based on the order of the weight of the differential terms. Equations that are in the order of one $\{O(1)\}$ indicate leading order equations. Also, equations of the order of $\{O(\varepsilon)\}$ are first order or acoustic equations. The group of equations, Eq. (10) through Eq. (12), are indicative of leading order equations:

$$(St) \frac{\partial \rho_0}{\partial t} + \nabla \cdot (\rho_0 \vec{u}_0) = 0; \quad (10)$$

$$(St) \left[\frac{\partial(\rho_0 \vec{u}_0)}{\partial t} \right] + \left[\vec{u}_0 \nabla \cdot (\rho_0 \vec{u}_0) \right] = (Eu) [-\nabla p_0] + \frac{1}{Re} \left[\nabla^2 \vec{u}_0 + \left(\frac{1}{3} + \frac{\mu_v}{\mu} \right) (\nabla \text{div}(\vec{u}_0)) \right]; \quad (11)$$

$$\begin{aligned} (St)(Eu) \frac{\partial p_0}{\partial t} + (Eu)(\vec{u}_0 \cdot \nabla) p_0 &= \left(\frac{c}{\bar{U}} \right)^2 \rho_0 (\nabla \cdot \vec{u}_0) + \\ &\left(\frac{c^2 \beta}{c_p} \right) \left[\frac{1}{Re_v} (\nabla \cdot \vec{u}_0)^2 + \frac{1}{Re} 2 \left\{ e_{ij}^0 e_{ji}^0 - \frac{1}{3} (\nabla \cdot \vec{u}_0)^2 \right\} \right]. \end{aligned} \quad (12)$$

As it can be observed, leading order equations are, in fact, the most general form of governing equations on the hydrodynamics of viscous and compressible fluid flow.^{21,22} Also,

Eqs. (13) through Eq. (15) are indicative of the obtained acoustical model.

$$(St) \frac{\partial \rho_1}{\partial t} + \nabla \cdot (\rho_0 \vec{u}_1) + \nabla \cdot (\rho_1 \vec{u}_0) = \rho_0 Q_0; \quad (13)$$

$$(St) \left[\frac{\partial(\vec{u}_0 \rho_1)}{\partial t} \right] + (St) \left[\frac{\partial(\rho_0 \vec{u}_1)}{\partial t} \right] + [(\vec{u}_0) \nabla(\vec{u}_0 \rho_1)] + [(\vec{u}_0) \nabla(\vec{u}_1 \rho_0)] + [\vec{u}_1 \nabla(\vec{u}_0 \rho_0)] = (Eu) [-\nabla(p_1)] + \frac{1}{Re} \left[\nabla^2(\vec{u}_1) + \left(\frac{1}{3} + \frac{\mu_v}{\mu} \right) (\nabla \text{div}(\vec{u}_1)) \right] + \rho_0 \vec{u}_0 Q_0; \quad (14)$$

$$(St)(Eu) \frac{\partial p_1}{\partial t} + (Eu)(\vec{u}_0 \cdot \nabla) p_1 + (Eu)(\vec{u}_1 \cdot \nabla) p_0 = - \left(\frac{c}{\bar{U}} \right)^2 \rho_0 (\nabla \cdot \vec{u}_1) - \left(\frac{c}{\bar{U}} \right)^2 \rho_1 (\nabla \cdot \vec{u}_0) + \left(\frac{c^2 \beta}{c_p} \right) \left[\frac{1}{Re_v} \cdot 2 \cdot (\nabla \cdot \vec{u}_0)(\nabla \cdot \vec{u}_1) + \frac{1}{Re} 2 \left\{ \frac{1}{4} \frac{\partial u_{0i}}{\partial x_j} \frac{\partial u_{1j}}{\partial x_i} + \frac{1}{4} \frac{\partial u_{0i}}{\partial x_j} \frac{\partial u_{1i}}{\partial x_j} + \frac{1}{4} \frac{\partial u_{1i}}{\partial x_j} \frac{\partial u_{0j}}{\partial x_i} + \frac{1}{4} \frac{\partial u_{0j}}{\partial x_i} \frac{\partial u_{1j}}{\partial x_i} - \frac{1}{3} \cdot 2 \cdot (\nabla \cdot \vec{u}_0)(\nabla \cdot \vec{u}_1) \right\} \right]. \quad (15)$$

Considering the present terms in Eq. (13) through Eq. (15), it could be concluded that the obtained acoustic equations system is coupled with the leading order ones. The observed coupling, in fact, is a kind of static coupling and is unilateral. In other words, the solving of the acoustic equations is only in need of determining the terms of the leading order like \vec{u}_0 , ρ_0 , p_0 , Q_0 . Also, there is no need to solve the leading and first order equation simultaneously. Generally, it would be possible to find these terms from an individual solution of the leading order equations. By applying the assumptions of linear acoustics in Eqs. (13) through Eq. (15), it could be shown that these equations will also end up as a linear wave formulation. This point can be considered as validity of the obtained acoustic model. Despite everything discussed, in proceeding, first, the validation of the obtained acoustic model will take place for a benchmark problem. Then, during the two other benchmarks, this acoustic model will apply for different sound sources, including dipole and quadrupole. Finally, the effect of the background fluid velocity on the sound wave propagation pattern in several benchmark problems will be reviewed and studied.

3. NUMERICAL RESULTS OBTAINED FROM ACOUSTIC MODEL

Benchmark problems considered in the present study include the presence of the spherical sound sources, which are located along the fluid flow with different velocities. In light of the existing symmetry in the problem, to present the numerical solution, it was attempted to use cylindrical axisymmetric coordination. Also, in order to solve the acoustical system of equations, the finite element method has been used. So, first,

the momentum equation must be decomposed into two equations along (r) and (z) based on the velocity axis in the form of $\vec{u}_1 = u_{1r} \vec{e}_r + v_{1z} \vec{e}_z$. Then, by disregarding terms along (θ), acoustic equations in cylindrical axisymmetric coordinates will be in the following forms:

$$\frac{\partial \rho_1}{\partial t} + \left(u_{1r} \frac{\partial \rho_0}{\partial r} + u_{1z} \frac{\partial \rho_0}{\partial z} \right) + \rho_0 \left(\frac{\partial u_{1r}}{\partial r} + \frac{u_{1r}}{r} + \frac{\partial u_{1z}}{\partial z} \right) + \left(u_{0r} \frac{\partial \rho_1}{\partial r} + u_{0z} \frac{\partial \rho_1}{\partial z} \right) + \rho_1 \left(\frac{\partial u_{0r}}{\partial r} + \frac{u_{0r}}{r} + \frac{\partial u_{0z}}{\partial z} \right) = \rho_0 Q_0; \quad (16)$$

$$\left(\rho_1 \frac{\partial u_{0r}}{\partial t} + u_{0r} \frac{\partial \rho_1}{\partial t} + r h o_0 \frac{\partial u_{1r}}{\partial t} + u_{1r} \frac{\partial \rho_0}{\partial t} \right) + \left(u_{1r} \frac{\partial u_{0r}}{\partial r} \rho_0 + u_{1z} \frac{\partial \rho_0}{\partial z} u_{0r} + u_{1z} \frac{\partial u_{0r}}{\partial z} \rho_0 \right) + \left(u_{0r} \frac{\partial \rho_1}{\partial r} u_{0r} + u_{0r} \frac{\partial u_{0r}}{\partial r} \rho_1 + u_{0z} \frac{\partial \rho_1}{\partial z} u_{0r} + u_{0z} \frac{\partial u_{0r}}{\partial z} \rho_1 \right) + \left(2 u_{0r} \frac{\partial \rho_0}{\partial r} u_{1r} + u_{0r} \frac{\partial u_{1r}}{\partial r} \rho_0 + u_{0z} \frac{\partial \rho_0}{\partial z} u_{1r} + u_{0z} \frac{\partial u_{1r}}{\partial z} \rho_0 \right) + \frac{\partial p_1}{\partial r} = \rho_0 u_{0r} Q_0; \quad (17)$$

$$\left(\rho_1 \frac{\partial u_{0z}}{\partial t} + u_{0z} \frac{\partial \rho_1}{\partial t} + r h o_0 \frac{\partial u_{1z}}{\partial t} + u_{1z} \frac{\partial \rho_0}{\partial t} \right) + \left(u_{1r} \frac{\partial \rho_0}{\partial r} u_{0z} + u_{1r} \frac{\partial u_{0z}}{\partial r} \rho_0 + u_{1z} \frac{\partial u_{0z}}{\partial z} \rho_0 \right) + \left(u_{0r} \frac{\partial \rho_1}{\partial r} u_{0z} + u_{0r} \frac{\partial u_{0z}}{\partial r} \rho_1 + u_{0z} \frac{\partial \rho_1}{\partial z} u_{0z} + u_{0z} \frac{\partial u_{0z}}{\partial z} \rho_1 \right) + \left(u_{0r} \frac{\partial \rho_0}{\partial r} u_{1z} + u_{0r} \frac{\partial u_{1z}}{\partial r} \rho_0 + 2 u_{0z} \frac{\partial \rho_0}{\partial z} u_{1z} + u_{0z} \frac{\partial u_{1z}}{\partial z} \rho_0 \right) + \frac{\partial p_1}{\partial z} = \rho_0 u_{0z} Q_0; \quad (18)$$

$$\frac{\partial p_1}{\partial t} + \left(u_{0r} \frac{\partial p_1}{\partial r} + u_{0z} \frac{\partial p_1}{\partial z} \right) + \left(u_{1r} \frac{\partial p_0}{\partial r} + u_{1z} \frac{\partial p_0}{\partial z} \right) + \rho_0 \left(\frac{C}{\bar{U}} \right)^2 \left(\frac{\partial u_{1r}}{\partial r} + \frac{u_{1r}}{r} + \frac{\partial u_{1z}}{\partial z} \right) + \rho_1 \left(\frac{C}{\bar{U}} \right)^2 \left(\frac{\partial u_{0r}}{\partial r} + \frac{u_{0r}}{r} + \frac{\partial u_{0z}}{\partial z} \right) = 0. \quad (19)$$

3.1. Validation of the Acoustic Model

As mentioned earlier, by placing the assumptions of linear acoustics in the presented acoustic models, the linear wave equation could be found. Nevertheless, in order to validate the equations and the algorithm of the solution, initially, a simple benchmark problem is used. This problem contains single frequency oscillations of a spherical sound source in a static fluid flow. In the proposed benchmark problems in this study, the scale parameters used are based on water as the background fluid with the following properties in the form of $L = 130$ mm, $\tilde{\omega} = L/\bar{U}$, $\bar{U} = 1500$ m/s, $\tilde{\rho} = 1000$ kg/m³, $\tilde{P} = \tilde{\rho} \tilde{U}^2$ with the given values. The oscillating sphere and the computational domain shape in the cylindrical axisymmetric coordinate is as

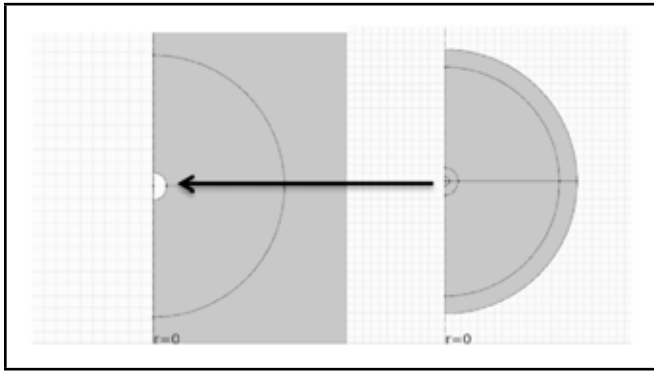


Figure 1. View of the cylindrical axisymmetric computational domain.

a half-circle. Figure 1 depicts a view of the computational domain beside the oscillating sphere in the cylindrical axisymmetric coordinate.

To prevent the effects of wave reflection and return, the computational domain extends to the point where, in light of sound wave velocity, during the time of the numerical analysis of the problem, the sound wave won't reach the end of the computational domain. Also, in order to prevent numerical instability, the Laplace of acoustic pressure and density will be considered zero on the end boundary of the computational domain. The boundary condition on the oscillating sphere with a dimensionless radius of $r_{\text{radius}} = 0.035 \text{ (m)/L}$ is $\vec{u} \cdot \vec{n} = \frac{0.005}{c} * \sin(2\pi \times (\frac{515}{\omega}) t^*)$. This problem is a model of a monopole sound source in the static fluid oscillating in the sinusoidal form with a frequency of $f = 515 \text{ Hz}$. Moreover, in order to review independence from the mesh grid, the above problem was repeated for four different mesh grids. In the selected mesh grid, the number of applied elements in the finite element solution is equal to 104,880. The dimensionless acoustic pressure obtained from this mesh grid compared to those obtained from a mesh grid containing 152,600 elements presented 0.3% relative error. Therefore, to reduce the calculation time, the mesh grid with the lower number of elements was chosen as a final mesh grid. Figure 2(a) is indicative of the time history of dimensionless acoustic pressure for the two sensors located within the distances $\tilde{r}_1 = 7 \text{ (m)/L}$ and $\tilde{r}_2 = 21 \text{ (m)/L}$. Figure 2(b) depicts the frequency response of dimensionless acoustic pressure for the same sensors.

According to Fig. 2(a), considering the sinusoidal pattern of the sound source fluctuations, the time response also possesses a sinusoidal form. On the other hand, in light of the results of the frequency response in Fig. 2(b), and based on the frequency response being dimensionless, if the obtained dimensionless value of $f = 0.28$ was returned to the dimensional form, this value would be $f = 514.19 \text{ Hz}$. This number is indicative of the overlapping of stimulation and response frequency. Furthermore, it could be observed that the sound wave intensity at distance \tilde{r}_2 from the source is decreased substantially compared to the distance due to divergence losses. In order to study the accuracy of the point mentioned, the Root Mean Square (RMS) of dimensionless pressure, which is indicative of effective sound pressure, would be compared to the

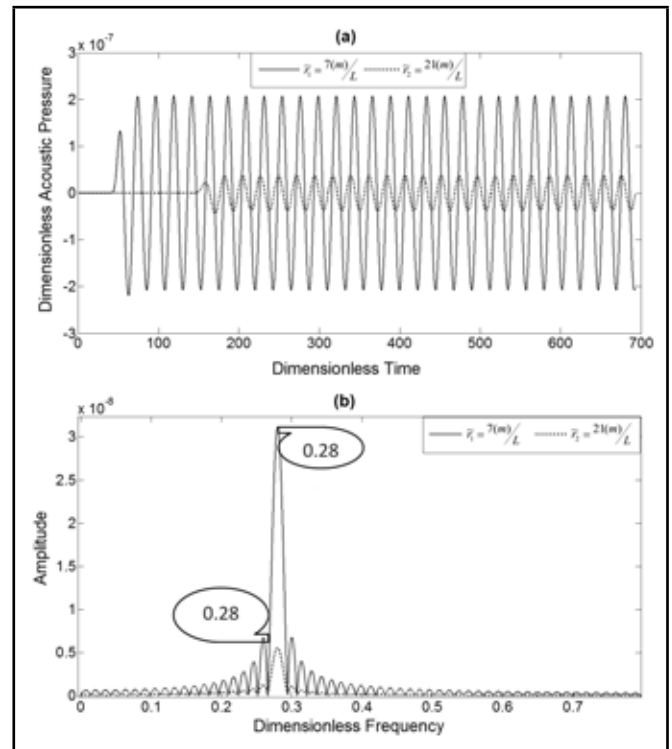


Figure 2. (a) Time response of dimensionless acoustic pressure for 2 sensors located at $\tilde{r}_1 = 7 \text{ (m)/L}$ and $\tilde{r}_2 = 21 \text{ (m)/L}$; (b) Frequency response of dimensionless acoustic pressure for 2 sensors located at $\tilde{r}_1 = 7 \text{ (m)/L}$ and $\tilde{r}_2 = 21 \text{ (m)/L}$.

results obtained from an analytical relation. According to the Distance Law, the following relation exists for a point source: According to Fig. 2(a), considering the sinusoidal pattern of the sound source fluctuations, the time response also possesses a sinusoidal form. On the other hand, in light of the results of the frequency response in Fig. 2(b), and based on the frequency response being dimensionless, if the obtained dimensionless value of $f = 0.28$ was returned to the dimensional form, this value would be $f = 514.19 \text{ Hz}$. This number is indicative of the overlapping of stimulation and response frequency. Furthermore, it could be observed that the sound wave intensity at distance \tilde{r}_2 from the source is decreased substantially compared to the distance due to divergence losses. In order to study the accuracy of the point mentioned, the Root Mean Square (RMS) of dimensionless pressure, which is indicative of effective sound pressure, would be compared to the results obtained from an analytical relation. According to the Distance Law, the following relation exists for a point source:

$$p_2 = p_1 \cdot \frac{r_1}{r_2};$$

$$20 \cdot \log(p_2)_{\text{dB}} = 20 \cdot \log(p_1)_{\text{dB}} + 20 \cdot \log\left(\frac{r_1}{r_2}\right)_{\text{dB}} \quad (20)$$

The above equations are indicative of the relationship of effective acoustic pressure p_1, p_2 between 2 points at distances r_1 and r_2 from the sound source, in terms of pressure unit and decibel. Now, if in light of simulation results, effective pressure p_1 at distance $\tilde{r}_1 = 7 \text{ (m)/L}$ be presumed as known, then, by using the distance law, effective pressure at distance $\tilde{r}_2 = 21 \text{ (m)/L}$ could be estimated. So, for comparing a numeri-

Table 1. Comparison of results of obtained effective pressure from numerical and analytical solutions at distance $\tilde{r}_2 = 21$ (m)/ L .

Numerical results of obtained effective pressure level at distance of $\tilde{r}_2 = 21$ (m)/ L and in dB unit	-336.707
Analytical results of obtained effective pressure level at distance of $\tilde{r}_2 = 21$ (m)/ L and in dB unit	-349.099
Relative error	3.550%

cal model presented here with the analytical model, it is assumed that the effective pressure p_1 at distance $\tilde{r}_1 = 7$ (m)/ L is known. Then, from the numerical model that is introduced in this paper and the analytical model referred to as Distance Law, effective pressure p_2 at distance $\tilde{r}_2 = 21$ (m)/ L would be predicted. For this goal, initially, the effective pressure at the distance of $\tilde{r}_1 = 7$ (m)/ L must be specified. In this investigation, it is chosen from numerical results and from time series pressure data. The Root Mean Square (RMS) of these dimensionless time pressures, which is indicative of effective sound pressure at distance $\tilde{r}_1 = 7$ (m)/ L , is obtained. For analytical results, this value is considered as p_1 in Distance Law and is used for calculating p_2 . On the other hand, by calculating RMS of the sound pressure time series data at distance $\tilde{r}_2 = 21$ (m)/ L , numerically and directly, p_2 is estimated. Results of the obtained effective pressure directly from the present study are compared with results of the analytical solution at a distance of $\tilde{r}_2 = 21$ (m)/ L and are presented in Table 1.

It is noteworthy that the obtained values are based on dimensionless results. Comparing the numerical and analytical results of the effective pressure level of sound in the problem shows that the acoustic model used in this study has been capable of modelling divergence losses of sound energy, effectively. Figure 3 and Fig. 4 are indicative of a sound wave propagation pattern at the dimensionless time of $t_1^* = 400$ and $t_2^* = 600$.

Figure 3(a) and Fig. 4(a) are indicative of the spatial pattern of sound wave propagation at axisymmetric coordinates. After solving the problem at axisymmetric coordinates and displaying the wave pattern in axisymmetric coordinates, the complete view of the wave propagation must be obtained. This has been done through an 180° rotation of the computational domain around the r -axis. By this rotation, the half sphere will be generated. Presented patterns in Fig. 3(b) and Fig. 4(b) are 2D views of this half sphere from the front view. It is obvious that the results indicate the spherical (can be circular in 2D figure) propagation of sound waves produced by the oscillation of a monopole sound source. It is noteworthy that during these dimensionless problems, the wave velocity is equal to one. So, according to the figures, at a time of $t_1^* = 400$, sound waves have reached the dimensionless distance $r_1^* \approx 400$, and at the time of $t_2^* = 600$, sound waves have reached the dimensionless distance $r_2^* \approx 600$.

3.2. Modelling of Dipole and Quadrupole Sound Sources

After the validation of the acoustic model, the above problem is considered for the dipole and quadrupole sources. In order to do that, two and four semi-circle sources with the

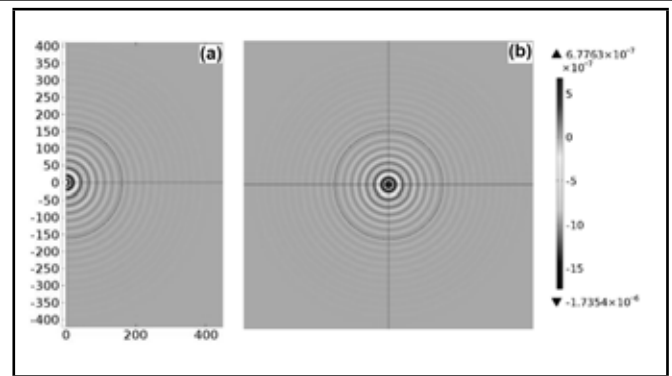


Figure 3. (a) Spatial wave propagation pattern of acoustic pressure around monopole sound sources at axisymmetric coordination and at a dimensionless time of $t_1^* = 400$, (b) Spatial wave propagation pattern of acoustic pressure around spherical monopole sound sources after 180° rotation around the r -axis at a dimensionless time of $t_1^* = 400$.

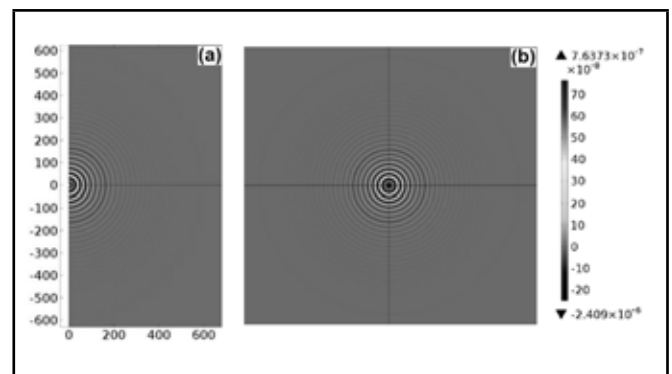


Figure 4. (a) Spatial wave propagation pattern of acoustic pressure around monopole sound sources at axisymmetric coordination and at a dimensionless time of $t_2^* = 600$, (b) Spatial wave propagation pattern of acoustic pressure around spherical monopole sound sources after 180° rotation around the r -axis at a dimensionless time of $t_2^* = 600$.

$radius = 0.035$ (m)/ L are used in axisymmetric cylindrical coordinates. It is important to note that in dipole modelling, two spheres (two semi-circles in axisymmetric coordinates) with equal frequency ($f = 515$ Hz) and 180° phase differences are oscillating, simultaneously. Also, in the linear quadrupole sound source model, all four spheres (four semi-circles in axisymmetric coordinates) that are stranded in a line are oscillating together with the same frequency of ($f = 515$ Hz). The oscillation of the two inside spheres is considered to have the same phase, and they have 180° phase differences with the two side spheres. The spatial wave propagation pattern produced by sinusoidal oscillation of dipole and quadrupole sound sources is shown in Fig. 5 and Fig. 6, respectively. The amplitude of the oscillations is also considered depending on the oscillation phase of each source in the form of $\vec{u} \cdot \vec{n} = \pm \left[\frac{0.005}{\bar{v}} * \sin \left(2\pi \times \left(\frac{515}{\omega} \right) t^* \right) \right]$.

Figure 5(a) and Fig. 6(a) are indicative of the spatial propagation pattern of the sound wave pressure in axisymmetric coordinates. After solving the problem in axisymmetric coordinates and the 180° rotating of the computational domain around the r -axis, the presented pattern in Fig. 5(b) and Fig. 6(b) can be obtained. Also, for better comparison between the dipole and quadrupole sound sources model, Fig. 7

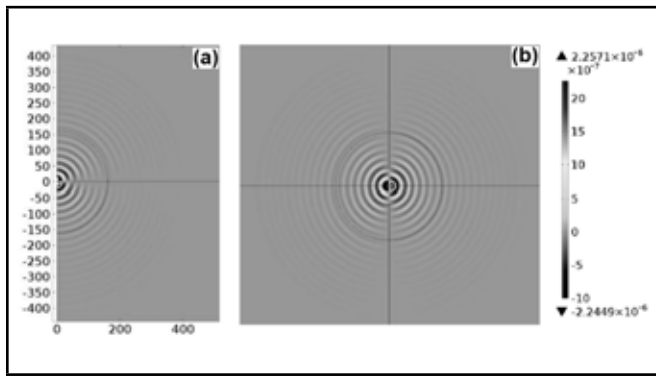


Figure 5. (a) Spatial wave propagation pattern of acoustic pressure around dipole sound sources at axisymmetric coordination and at a dimensionless time of $t_1^* = 400$, (b) Spatial wave propagation pattern of acoustic pressure around dipole sound sources after 180° rotation around the r -axis at a dimensionless time of $t_1^* = 400$.

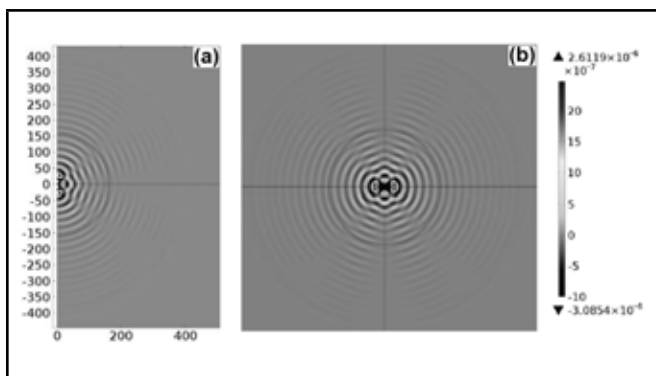


Figure 6. (a) Spatial wave propagation pattern of acoustic pressure around quadrupole sound sources at axisymmetric coordination and at a dimensionless time of $t_1^* = 400$, (b) Spatial wave propagation pattern of acoustic pressure around quadrupole sound sources after 180° rotation around the r -axis at a dimensionless time of $t_1^* = 400$.

and Fig. 8 display the directivity pattern due to the dipole and quadrupole sound source.

In these figures, the oscillating spheres were located at the centre of these polar plots, and the main axes are horizontal (between 0 and 180°). These directivity patterns are those expected from the dipole and linear quadrupole sound sources at the far field. So, by the consideration of the spatial patterns of Fig. 5 and Fig. 6 besides the far field directivity patterns of Fig. 7 and Fig. 8, it is obvious that the results indicate the acoustic model introduced in this investigation is capable of modelling and solving different sound sources. At the same time, this model is also capable of considering parameters like velocity and viscosity of the background fluid flow. The effects of the background fluid flow will be analysed later on.

3.3. Study of Flow Velocity Effects on the Spatial Pattern of Sound Wave

In the previous problem, the background flow velocity was considered to be equal to zero. Here, attempts are made to investigate the sound wave pattern produced by monopole sound sources and in a flow with a different Mach number. It is important to point out that placement of a fixed sound source in a dynamic fluid flow, from the point of view of a sound

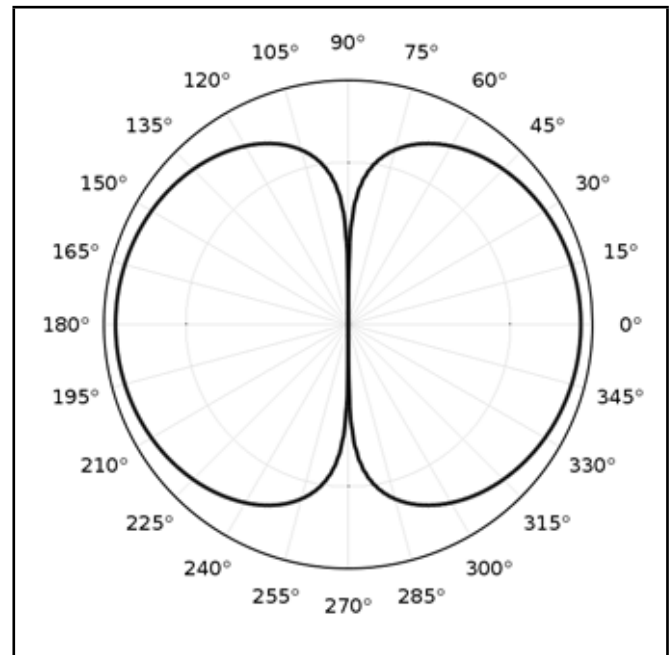


Figure 7. Far field directivity pattern of dipole sound source with a frequency of $f = 515$ Hz at a dimensionless time of $t_1^* = 400$.

pattern, is equivalent and similar to assuming that the flow is stationary and the oscillating source in the fluid flow is moving. The patterns shown in Fig. 9 and Fig. 10 are indicative of the presence of a monopole sound source in the fluid flow with different velocities. In Fig. 9, the frequency of oscillation is equal to 5510 Hz. Also, the boundary condition on the wall of the oscillating source is in the form of $\vec{u} \cdot \vec{n} = \frac{0.005}{U} * \sin(2\pi * (\frac{5510}{\omega}) t^*)$. It is necessary to point out that the results have been obtained based on equations and parameters being non-dimensional.

Similarly, the results are obtained on the basis of another monopole source oscillated with a frequency of 75 Hz. The boundary condition imposed on the wall of the oscillating source is in the form of $\vec{u} \cdot \vec{n} = \frac{0.005}{U} * \sin(2\pi * (\frac{75}{\omega}) t^*)$. These results are shown in Fig. 10.

As it is evident from Fig. 9 and Fig. 10, the results were compared for three background flow velocities. The relation of the Mach number is $Ma = u/c$. In light of all of the relations and the analysis in this study being dimensionless and the independent of the nature of the fluid flow, the velocity of the background flow in this investigation is considered such that the Mach numbers of $Ma = 0.067, 0.133, 0.267$ are produced. Based on the obtained results, by any increase in the Mach number that was caused by the background flow velocity increase, the spherical pattern of the sound wave propagation would be dissipated. In order to precisely observe the outcome, some concentric circles centred on the monopole sound source are drawn, virtually. By comparing the pattern of propagation with these circles, it becomes evident that through increasing the Mach number, the sound propagation pattern shows more tendencies to exit from the spherical form. Also, it is obvious that acoustic pressure contours are more compressed at the downstream of the sound source, whereas, at the upstream, the flow is more rarefaction. This situation, in particular at the

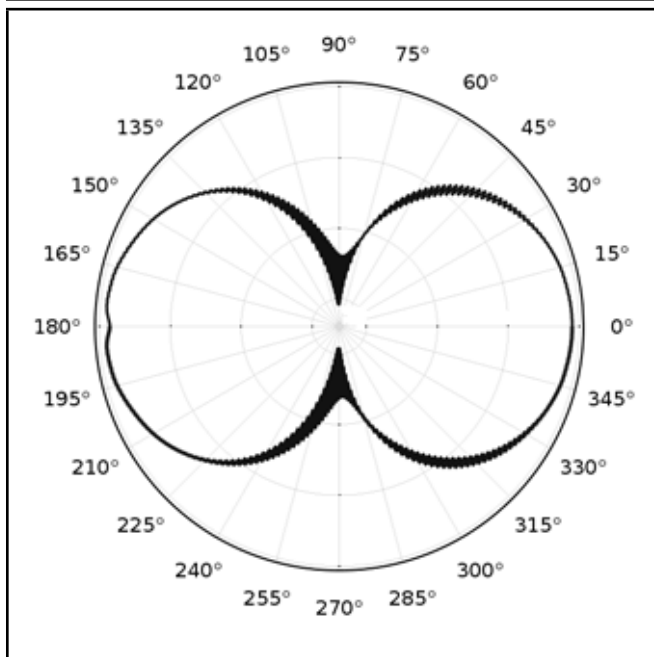


Figure 8. Far field directivity pattern of linear quadrupole sound source with a frequency of $f = 515$ Hz at a dimensionless time of $t_1^* = 400$.

Mach number of $Ma = 0.267$, is more vividly noticeable. The reason for this is that at the downstream of the source, the flow direction is opposite to the direction of the sound wave propagation. Consequently, this causes the pressure contours to be more concentrated. This concentration, in return, leads to an increase in the intensity of the acoustic pressure in this region.

4. DISCUSSION AND CONCLUSIONS

Conservation equations of mass, momentum, energy, and the equation of state are considered the fundamental equations in the formulation of a linear acoustic equation or a wave equation. Recognition and analysis of acoustic noise stemmed from the occurrence of a hydrodynamic phenomenon in a fluid flow depends on these equations being studied completely in the entire computational domain. Inequalities of time and space hydrodynamical and acoustical scale and the resulting time cost of the computational processes make this analysis very cumbersome or even impossible. On the other hand, many simplifying assumptions involved in the conservation equations used to obtain the wave equation are sometimes not suitable. Therefore, in the present study, by utilizing scale or dimensional analysis and the perturbation method, governing equations on the fluid flow dynamics are separated from governing equations of acoustics. Then, each one of these equations should be analysed and studied in a suitable domain. This means each equation is governed in a domain where the other equation is not to be able to affect it. So, separation of the equation at different orders and using each group of equations in the related computational domain leads to an enormous reduction in the computational processing for the hydrodynamic and hydroacoustic simulation. Based on the obtained results, the acoustic model of the present study is capable of modelling different kinds of acoustic sources effectively. Furthermore, the ability

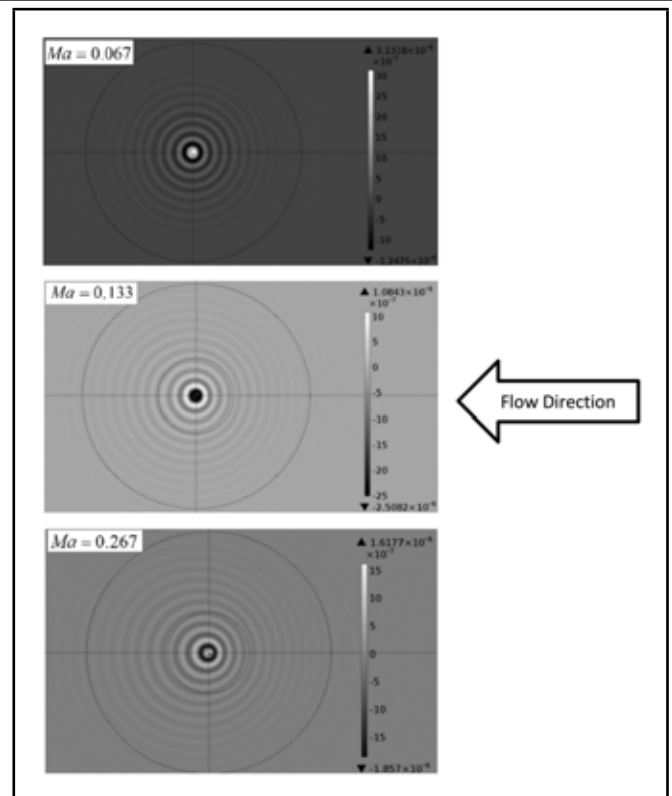


Figure 9. Spatial wave propagation pattern of acoustic pressure caused by the oscillation of a monopole sound source with a frequency of $f = 5510$ Hz and the presence of a background flow with different velocities.

of this acoustic model in the recognition and the prediction of a pattern of wave propagation that stemmed from the presence of oscillating sound sources with desired frequency in the fluid flow with a different speed were proven and demonstrated.

REFERENCES

- Walsh, T., Torres, M. Finite element methods for nonlinear acoustics in fluids, *Journal of Computational Acoustics*, **15** (3), 353–375, (2007).
- Zheng, T. H., Tang S. K., Shen, W. Z. Simulation of vortex sound using the viscous/acoustic splitting approach, *Transactions of the Canadian Society for Mechanical Engineering*, **35** (1), 39–56, (2011).
- Ewert, R., Schröder, W. Acoustic perturbation equations based on flow decomposition via source filtering, *Journal of Computational Physics*, **188** (2), 365–398, (2003).
- Pfowcs Williams, J. E., Hawkings, D. L. Sound generated by turbulence and surfaces in arbitrary motion, *Philosophical Transactions of the Royal Society of London Series A*, **264**, 321–342, (1969).
- Salvatore, F., Ianniello, S. Preliminary results on acoustic modelling of cavitating propellers, *Computational Mechanics*, **32** (4–6), 291–300, (2003).
- Seol, H., Jung, B., Suh, J. C., Lee, S. Prediction of non-cavitating underwater propeller noise, *Journal of Sound and Vibration*, **257** (1), 131–156, (2002).

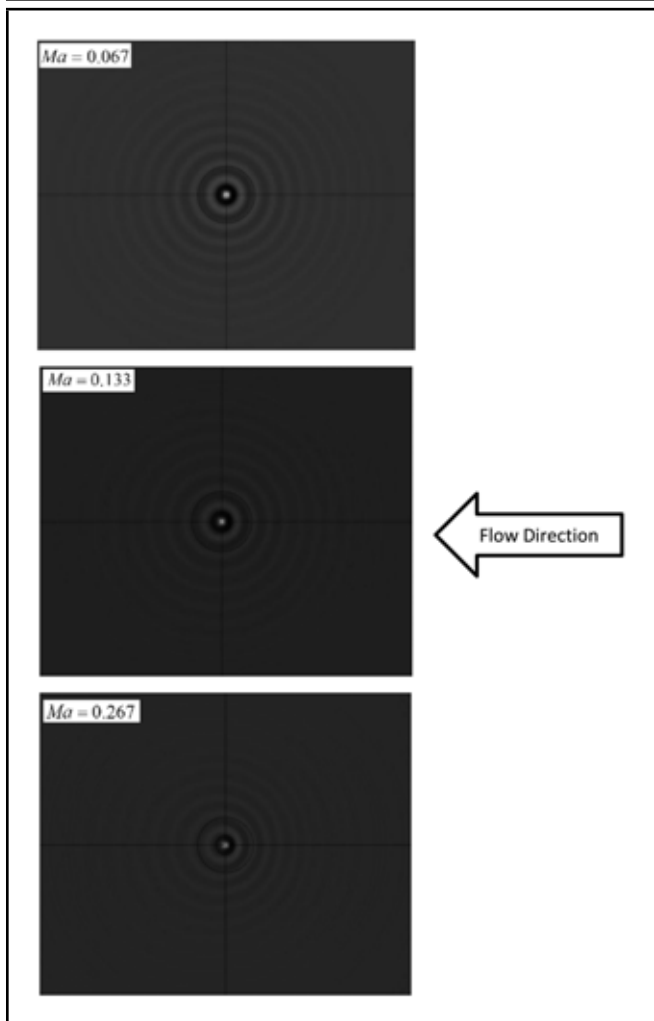


Figure 10. Spatial wave propagation pattern of acoustic pressure caused by the oscillation of a monopole sound source with a frequency of $f = 75$ Hz and the presence of a background flow with different velocities.

- 7 Seol, H., Suh, J.-C., Lee, S. Development of hybrid method for the prediction of underwater propeller noise, *Journal of Sound and Vibration*, **288** (1–2), 345–360, (2005).
- 8 Salvatore, F., Testa, C., Greco, L. Coupled hydrodynamics–hydroacoustics BEM modelling of marine propellers operating in a wakefield, *Proc. First International Symposium on Marine Propulsors smp'09, MARINTEK*, Norwegian Marine Technology Research Institute, Trondheim, Norway, (2009).
- 9 Seo, J. H., Moon, Y. J. Linearized perturbed compressible equations for low Mach number aeroacoustics, *Journal of Computational Physics*, **218** (2), 702–719, (2006).
- 10 Seo, J. H., Moon, Y. J., Shin, B. R. Prediction of cavitating flow noise by direct numerical simulation, *Journal of Computational Physics*, **227** (13), 6511–6531, (2008).
- 11 Hardin, J. C., Pope, D. S. An acoustic/viscous splitting technique for computational aeroacoustics, *Theoretical and Computational Fluid Dynamics*, **6** (6–5), 323–340, (1994).
- 12 Shen, W. Z., Sørensen, J. N. Comment on the aeroacoustic formulation of Hardin and Pope, *AIAA Journal*, **37** (1), 141–143, (1999).
- 13 Slimon, S. A., Soteriou, M. C., Davis, D. W. Development of computational aeroacoustics equations for subsonic flows using a Mach number expansion approach, *Journal of Computational Physics*, **159** (2), 377–406, (2000).
- 14 Seo, J.-H., Moon, Y. J. Perturbed compressible equations for aeroacoustic noise prediction at low Mach numbers, *AIAA Journal*, **43** (8), 1716–1724, (2005).
- 15 Moon, Y. J. Sound of fluids at low Mach numbers, *European Journal of Mechanics - B/Fluids*, **40**, 50–63, (2013).
- 16 Ewert, R., Schröder, W. On the simulation of trailing edge noise with a hybrid LES/APE method, *Journal of Sound and Vibration*, **270** (3), 509–524, (2004).
- 17 Kuznetsov, V. P. Equations of nonlinear acoustics, *Soviet Physics - Acoustics*, **16**, 467–470, (1971).
- 18 Söderholm, L. H. On the Kuznetsov equation and higher order nonlinear acoustics equations, *Proc. AIP Conference Proceedings, 15th International Symposium*, Göttingen, Germany, (1999).
- 19 Hoffelner, J., Landes, H., Kaltenbacher, M., Lerch, R. Finite element simulation of nonlinear wave propagation in thermoviscous fluids including dissipation, *Ultrasonics, IEEE Transactions on Ferroelectrics and Frequency Control*, **48** (3), 779–786, (2001).
- 20 Temkin, S. *Elements of Acoustics*, John Wiley & Sons, New York, (1981).
- 21 Saranjam, B. Experimental and numerical investigation of an unsteady supercavitating moving body, *Journal of Ocean Engineering*, **59**, 9–14, (2013).
- 22 Nouri, N. M., Moghimi, M., and Mirsaeedi, S. M. H. Unsteady modelling of cavitating flow with artificial viscosity, *Proceedings of the Institution of Mechanical Engineers, Part C: Journal of Mechanical Engineering Science*, **224** (1), 123–132, (2010).

A Note on the Influence of Intermediate Restraints and Hinges in Frequencies and Mode Shapes of Beams

Javier L. Raffo

Universidad Tecnológica Nacional, Facultad Regional Delta, San Martín 1171, 2804 Campana, Argentina

Ricardo O. Grossi

Universidad Nacional de Salta, INIQUI - Facultad de Ingeniería, Av. Bolivia 5150, 4400 Salta, Argentina

(Received 21 December 2012; revised: 27 March 2013; accepted: 30 April 2013)

This note deals with the free transverse vibration of a beam with two arbitrarily located internal hinges, four intermediate elastic restraints, and ends elastically restrained against rotation and translation. The method of separation of variables is used for the determination of the exact frequencies and mode shapes. New results are presented for different boundary conditions and restraint conditions in the internal hinges.

The mathematical model is also used to study the influence on the frequencies and mode shapes of varying intermediate supports that are located at the nodal points of higher modes. A detailed numerical study on the effects of the locations of intermediate translational restraints and their stiffness on the natural frequencies and mode shapes is performed for different boundary conditions. The effect of the presence of the internal hinges is also analysed. Graphs and tables of the non-dimensional frequencies and the corresponding mode shapes are given in order to illustrate the behaviour of frequency parameters and the presence of mode shape switching.

1. INTRODUCTION

There has been extensive research into the vibration of Euler–Bernoulli beams with elastic restraints. It is not possible to give a reasonable and detailed account of this great amount of information; nevertheless, some relevant references will be cited. Particularly, several investigators have studied the influence of elastic restraints at the ends of vibrating beams.^{1–16} Exact frequency and normal mode shape expressions have been derived for uniform beams with elastically restrained ends against rotation and translation.¹⁷ Excellent handbooks have appeared in the literature giving frequencies, tables and mode shape expressions.^{18,19}

The problem of the vibrations of beams that are elastically restrained at intermediate points has also been extensively treated. One of the earliest works was performed by Lee and Saibel who analysed the problem of free vibrations of a constrained beam with intermediate elastic supports.²⁰ Rutenberg presented eigenfrequencies for a uniform cantilever beam with a rotational restraint at an intermediate position.²¹ Lau extended Rutenberg's results with an additional translational restriction.²² Maurizi and Bambill analysed the transverse vibrations of clamped beams with an intermediate translational restraint.²³ Rao analysed the frequencies of a clamped-clamped uniform beam with intermediate elastic support.²⁴ De Rosa et al. studied the free vibrations of stepped beams with intermediate elastic supports.²⁵ Ewing and Mirsafian analysed the forced vibrations of two beams joined with a non-linear rotational joint.²⁶ Arenas and Grossi presented exact and approximate frequencies of a uniform beam, with one end spring-

hinged and a rotational restraint in a variable position.²⁷ Grossi and Albarraçín determined the exact eigenfrequencies of a uniform beam with intermediate elastic constraints.²⁸

The minimum stiffness of an elastic translational restriction that raises a natural frequency of a beam to its upper limit has been investigated by several researchers. Courant and Hilbert have demonstrated that the optimum location of a rigid support should be at the nodal points of a higher vibration mode.²⁹ Akesson and Olhoff showed that in the case of elastic supports the optimum locations are the same as that of rigid supports, and there exists a minimum stiffness of an additional elastic support whenever the fundamental frequency of a uniform cantilever beam is increased to its maximum.³⁰ Wang determined the minimum stiffness of an internal elastic support to maximize the fundamental frequency of a vibrating beam.³¹ Wang et al. derived the closed-form solution for the minimum stiffness of a simple point support that raises a natural frequency of a beam to its upper limit.³² Albarraçín et al. detected a rather curious situation of changes in frequency values and mode shapes when an intermediate translational restraint is placed in a beam that is simply supported at both ends.³³

There is only a limited amount of information for the vibration of beams with internal hinges. Wang and Wang studied the fundamental frequency of a beam with an internal hinge with an axial force.³⁴ Chang et al. investigated the dynamic response of a beam with an internal hinge, subjected to a random moving oscillator.³⁵ Grossi and Quintana investigated the natural frequencies and mode shapes of a non homogeneous tapered beam subjected to general axial forces, with an arbitrarily located internal hinge and elastic supports and ends that

are elastically restrained against rotation and translation.³⁶

The above review of the literature reveals that many efforts have been devoted to the analysis of the influence of elastic restraints parameters, located at the ends and intermediate points, on the dynamics characteristics of beams. However, the influence on the frequencies and mode shapes of varying intermediate supports located at the nodal points of higher modes has been studied only for classical end conditions. There is no paper that presents a complete analysis of the mentioned effects of intermediate elastic supports in a beam generally restrained at both ends. Also, in this subject the presence of internal hinges has not been treated.

The aim of the present note is to investigate the natural frequencies and mode shapes of a beam with two arbitrarily located internal hinges, four intermediate elastic restraints and ends elastically restrained against rotation and translation. Adopting the adequate values of the rotational and translational restraints parameters at the ends, all the possible combinations of classical end conditions, (i.e., clamped, simply supported, sliding and free) can be generated. The presence of the two hinges and the intermediate elastic restraints in particular, allows for the inclusion of a hinge located at an intermediate point and a translational restraint located at a different point. This property will prove to be valuable in studying the influence of a translational restraint located at a node of a higher mode of vibration. The existence of a critical value of the dimensionless restraint parameter which determines the interchange of roles of the corresponding modal shapes of two consecutive non-dimensional frequency parameters is demonstrated. More specifically, whenever there is no internal hinge and the beam is simply supported, it is demonstrated that some frequencies increase as the stiffness of the intermediate support increases; if this parameter assumes a critical value, the symmetric modes shift to anti-symmetric modes and vice versa. The existence of an analogue phenomenon in the case of other boundary conditions is established; this also exists when there is an internal hinge.

The classical method of the separation of variables has been used for the determination of the exact frequencies and mode shapes. The algorithm developed can be applied to a wide range of elastic restraint conditions. The effects of the variations of the elastic restraints on the switching of the mode shape order and the influence of the internal hinges are investigated. Tables and figures are given for frequencies, and two-dimensional plots for mode shapes are included. A great number of problems were solved and, since the number of cases is prohibitively large, results are presented for only a few cases. The present note is organized first by the brief history stated above. In Section 2, a rigorous treatment of techniques of the calculus of variations to obtain the governing differential equations, the boundary conditions and the transitions conditions is presented. In Section 3, the method of the separation of variables is used for the determination of the exact frequencies and mode shapes. In Section 4, the influence of intermediate translational restraints is considered, and the analyses of the most important cases are included. Finally, Section 5 contains the conclusions of this note.

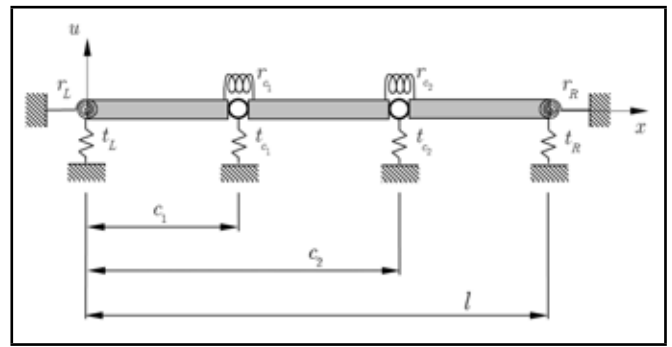


Figure 1. Mechanical system under study.

2. THE BOUNDARY VALUE PROBLEM

Let us consider a beam of length l , which has elastically restrained ends, is constrained at two intermediate points and has two internal hinges, as shown in Fig. (1). The beam system is made up of three different spans, which correspond to the intervals $[0, c_1]$, $[c_1, c_2]$ and $[c_2, l]$ respectively. It is assumed that the ends and the internal hinges are elastically restrained against translation and rotation. The rotational restraints are characterised by the parameters $r_L, r_R, r_{c_i}, i = 1, 2$ and the translational are characterized by $t_L, t_R, t_{c_i}, i = 1, 2$. Adopting the adequate values of the parameters r_L, r_R and t_L, t_R , all the possible combinations of classical end conditions can be generated. By using $t_{c_i}, r_{c_i}, i = 1, 2$, the effects of the internal hinges and intermediate restraints are taken into account.

In order to analyse the transverse planar displacements of the system under study, we suppose that the vertical position of the beam at any time t is described by the function $u = u(x, t), x \in [0, l]$. It is well known that at time t , the kinetic energy of the beam can be expressed as

$$T_b = \frac{1}{2} \sum_{i=1}^3 \int_{c_{i-1}}^{c_i} (\rho A)_i(x) \left(\frac{\partial u}{\partial t}(x, t) \right)^2 dx; \quad (1)$$

where $(\rho A)_i = \rho_i A_i$ denotes the mass per unit length of the i -th span and $c_0 = 0, c_3 = l$.

The total potential energy due to the elastic deformation of the beam, the elastic restraints at the ends and the intermediate elastic restraints, is given by:

$$U = \frac{1}{2} \left\{ \sum_{i=1}^3 \int_{c_{i-1}}^{c_i} (EI)_i(x) \left(\frac{\partial^2 u}{\partial x^2}(x, t) \right)^2 dx + \sum_{i=0}^3 \left(r_{c_i} \left(\frac{\partial u}{\partial x}(c_i^+, t) - \frac{\partial u}{\partial x}(c_i^-, t) \right)^2 + t_{c_i} u^2(c_i, t) \right) \right\}; \quad (2)$$

where $(EI)_i = E_i I_i$ denotes the flexural rigidity of the i -th span, $r_{c_0} = r_L, t_{c_0} = t_L, r_{c_3} = r_R$, and $t_{c_3} = t_R$. The notations $0^+, c_i^+, c_i^-$ and l^- imply the use of lateral limits and lateral derivatives and in consequence in Eq. (2), it is assumed that $\frac{\partial u}{\partial x}(0^-, t) = 0, \frac{\partial u}{\partial x}(l^+, t) = 0$.

Hamilton's principle requires that between times t_a and t_b , at which the positions are known, the motion will make station-

$$F(u) = \frac{1}{2} \int_{t_a}^{t_b} \left[\sum_{i=1}^3 \int_{c_{i-1}}^{c_i} \left((\rho A)_i(x) \left(\frac{\partial u}{\partial t}(x, t) \right)^2 - (EI)_i(x) \left(\frac{\partial^2 u}{\partial x^2}(x, t) \right)^2 \right) dx \right] dt - \frac{1}{2} \int_{t_a}^{t_b} \sum_{i=0}^3 \left[r_{c_i} \left(\frac{\partial u}{\partial x}(c_i^+, t) - \frac{\partial u}{\partial x}(c_i^-, t) \right)^2 + t_{c_i} u^2(c_i, t) \right] dt. \quad (3)$$

$$D = \left\{ u; u(x, \bullet) \in C^2([t_a, t_b]), u(\bullet, t) \in C([0, l]), u(\bullet, t)|_{[c_{i-1}, c_i]} \in C^4([c_{i-1}, c_i]), i = 1, 2, 3, \right. \\ \left. u(x, t_a), u(x, t_b) \text{ predescribed } \forall x \in [0, l] \right\}. \quad (5)$$

$$D_a = \left\{ v; v(x, \bullet) \in C^2([t_a, t_b]), v(\bullet, t) \in C([0, l]), v(\bullet, t)|_{[c_{i-1}, c_i]} \in C^4([c_{i-1}, c_i]), i = 1, 2, 3, \right. \\ \left. v(x, t_a) = v(x, t_b) = 0, \forall x \in [0, l] \right\}. \quad (6)$$

ary the action integral $F(u) = \int_{t_a}^{t_b} L dt$ on the space of admissible functions, where the Lagrangian L is given by $L = T_b - U$. In consequence, the energy functional to be considered is given by Eq. (3).

The stationary condition for the functional given by Eq. (3) requires that

$$\delta F(u; v) = 0, \quad \forall v \in D_a; \quad (4)$$

where $\delta F(u; v)$ is the first variation of F at u in the direction v and D_a is the space of admissible directions at u for the space D of admissible functions. In order to make the mathematical developments required by the application of the techniques of the calculus of variations, we assume that $(\rho A)_i \in C([c_{i-1}, c_i])$, $(EI)_i \in C^2([c_{i-1}, c_i])$, $i = 1, 2, 3$. The space D is the set of functions $u(x, \bullet) \in C^2([t_a, t_b])$, $u(\bullet, t) \in C([0, l])$, $u(\bullet, t)|_{[c_{i-1}, c_i]} \in C^4([c_{i-1}, c_i])$, $i = 1, 2, 3$.

In view of all these observations and since Hamilton's principle requires that at times t_a and t_b the positions are known, the space D is given by Eq. (5).

The only admissible directions v at $u \in D$ are those for which $u + \varepsilon v \in D$ for a sufficiently small ε and $\delta F(u; v)$ exists. In consequence, and in view of Eq. (5), v is an admissible direction at u for D if, and only if, $v \in D_a$ where D_a is given by Eq. (6).

The definition of the first variation of F at u in the direction v , is given by

$$\delta F(u; v) = \left. \frac{dF(u + \varepsilon v)}{d\varepsilon} \right|_{\varepsilon=0}. \quad (7)$$

The application of Eq. (7) with the expression of F given by Eq. (3) leads to Eq.(8).

The integration by parts of the procedure and the well-known application of the fundamental lemma of the calculus of variations leads to the following boundary value problem:

$$\frac{\partial^2}{\partial x^2} \left((EI)_i(x) \frac{\partial^2 u}{\partial x^2}(x, t) \right) + (\rho A)_i(x) \frac{\partial^2 u}{\partial t^2}(x, t) = 0, \\ \forall x \in (c_{i-1}, c_i), \quad i = 1, 2, 3, t \geq 0; \quad (9)$$

$$r_L \frac{\partial u}{\partial x}(0^+, t) = (EI)_1 0^+ \frac{\partial^2 u}{\partial x^2}(0^+, t); \quad (10)$$

$$t_L u(0^+, t) = -\frac{\partial}{\partial x} \left((EI)_1(0^+) \frac{\partial^2 u}{\partial x^2}(0^+, t) \right); \quad (11)$$

$$w(c_i^-, t) = w(c_i^+, t), \quad i = 1, 2; \quad (12)$$

$$r_{c_i} \left(\frac{\partial u}{\partial x}(c_i^+, t) - \frac{\partial u}{\partial x}(c_i^-, t) \right) = \\ (EI)_i(c_i^-) \frac{\partial^2 u}{\partial x^2}(c_i^-, t), \quad i = 1, 2; \quad (13)$$

$$r_{c_i} \left(\frac{\partial u}{\partial x}(c_i^+, t) - \frac{\partial u}{\partial x}(c_i^-, t) \right) = \\ (EI)_{i+1}(c_i^+) \frac{\partial^2 u}{\partial x^2}(c_i^+, t), \quad i = 1, 2; \quad (14)$$

$$t_{c_i} u(c_i, t) = \frac{\partial}{\partial x} \left((EI)_i(c_i^-) \frac{\partial^2 u}{\partial x^2}(c_i^-, t) \right) - \\ \frac{\partial}{\partial x} \left((EI)_{i+1}(c_i^+) \frac{\partial^2 u}{\partial x^2}(c_i^+, t) \right), \quad i = 1, 2; \quad (15)$$

$$r_R \frac{\partial u}{\partial x}(l^-, t) = -(EI)_3(l^-) \frac{\partial^2 u}{\partial x^2}(l^-, t); \quad (16)$$

$$t_R u(l^-, t) = \frac{\partial}{\partial x} \left((EI)_3(l^-) \frac{\partial^3 u}{\partial x^3}(l^-, t) \right) \text{ where } t \geq 0. \quad (17)$$

Different situations can be generated by substituting values and/or limiting values of the restraint parameters r_c and t_c . When we consider $r_{c_i} = \infty$, $t_{c_i} = 0$, $i = 1, 2$, there are no internal hinges. Now if we consider $r_{c_i} = 0$, $t_{c_i} = 0$, $i = 1, 2$, there are internal hinges located at c_1 and c_2 and the articulations are perfect. Finally if we have $0 < r_{c_i} < \infty$, $0 < t_{c_i} < \infty$, $i = 1, 2$, there are internal hinges elastically restrained against rotation and supported by the respective translational restraints.

$$\delta F(u; v) = \int_{t_a}^{t_b} \left[\sum_{i=1}^3 \int_{c_{i-1}}^{c_i} \left((\rho A)_i(x) \frac{\partial u}{\partial t}(x, t) \frac{\partial v}{\partial t}(x, t) - (EI)_i(x) \frac{\partial^2 u}{\partial x^2}(x, t) \frac{\partial^2 v}{\partial x^2}(x, t) \right) dx - \sum_{i=0}^3 \left(r_{c_i} \left(\frac{\partial u}{\partial x}(c_i^+, t) - \frac{\partial u}{\partial x}(c_i^-, t) \right) \left(\frac{\partial v}{\partial x}(c_i^+, t) - \frac{\partial v}{\partial x}(c_i^-, t) \right) + t_{c_i} u(c_i, t) v(c_i, t) \right) \right] dt. \tag{8}$$

It is worth noting that this mathematical model allows the inclusion of a hinge located at a point c_i and a translational restraint located at a different point c_j . As stated above this property will prove to be valuable for studying the influence of a translational restraint located at a node of a higher vibration mode.

3. NATURAL FREQUENCIES AND MODE SHAPES

Using the well-known method of the separation of variables, when the mass per unit length and the flexural rigidity at the spans are constant, we assume as solutions of Eq. (9) the functions given by the series

$$u_i(x, t) = \sum_{n=1}^{\infty} u_{i,n}(x) \cos \omega t, \quad i = 1, 2, 3; \tag{18}$$

where $u_{i,n}$ are the corresponding n th nodes of natural vibration, and ω is the radian frequency. Introducing the change of variable $\bar{x} = x/l$ into Eqs. (9) through (17), the functions $u_{i,n}$ are given by

$$u_{i,n}(\bar{x}) = A_i \cosh \lambda \bar{x} + B_i \sinh \lambda \bar{x} + C_i \cos \lambda \bar{x} + D_i \sin \lambda \bar{x}, \quad \forall \bar{x} \in [a_i, b_i]; \tag{19}$$

where $\bar{c}_i = c_i/l$, $a_1 = 0$, $b_1 = \bar{c}_1$, $a_2 = \bar{c}_1$, $b_2 = \bar{c}_2$, $a_3 = \bar{c}_2$, $b_3 = 1$, and

$$\lambda^4 = \frac{\rho A}{EI} \omega^2 l^4; \tag{20}$$

where $\rho A = (\rho A)_1 = (\rho A)_2 = (\rho A)_3$ and $EI = (EI)_1 = (EI)_2 = (EI)_3$. Substituting Eq. (19) into Eq. (18), and then in the boundary conditions given by Eqs. (10), (11), (16), (17) and transition conditions defined by Eqs. (12) to (15), expressed in the new variable \bar{x} , we obtain a set of twelve homogeneous equations in the constants A_i, \dots, D_i . Since the system is homogeneous, in order to obtain a non-trivial solution, the determinant of coefficients must be equal to zero. This procedure yields the frequency equation:

$$G(T_L, R_L, T_R, R_R, T_{\bar{c}_i}, R_{\bar{c}_i}, \lambda, \bar{c}_i) = 0, \quad i = 1, 2; \tag{21}$$

where

$$T_L = \frac{t_L l^3}{EI}, R_L = \frac{r_L l}{EI}, T_R = \frac{t_R l^3}{EI}, R_R = \frac{r_R l}{EI}, T_{\bar{c}_i} = \frac{t_{c_i} l^3}{EI}, R_{\bar{c}_i} = \frac{r_{c_i} l}{EI}, \quad i = 1, 2. \tag{22}$$

The values of the frequency parameter $\lambda = ((\rho A/EI)\omega^2)^{1/4} l$, were obtained with the classical bisection method and rounded to eight decimal digits.

In order to describe the corresponding boundary conditions the symbolism *SS* identifies a simply supported end, *C* a clamped end, *F* a free end and *ER* identifies an elastically restrained end. Since the number of cases which can be analysed by the developed algorithm is prohibitively large, results are presented only for a few cases.

Table 1 and Table 2 depict the first three exact values of the frequency parameter λ of a beam with two internal hinges. Different boundary conditions and values of the parameters $\bar{c}_i, i = 1, 2$ are considered. The corresponding mode shapes are also included. It is worth noting that in order to avoid zero frequencies and to obtain mode shapes, which clearly show the effect of the hinges, a relative small value of the restraint parameters $T_{\bar{c}_1}$ and $T_{\bar{c}_2}$ has been adopted. Table 1 contains symmetrical boundary conditions, and Table 2 includes non-symmetrical boundary conditions. In the case *ER – ER*, the values $T_L = R_L = 1000, T_R = R_R = 100$ have been adopted. It is worth pointing out that $u(\bullet, t) \in C[0, 1]$, i.e. the deflection function is only continuous, but it has corner points that only exist at the hinges locations. This property can be observed in the mode shapes included in Tables 1 and 2.

Table 3 depicts the first six exact values of the frequency parameter λ of a beam with two free internal hinges, different boundary conditions, and different values of the restraint parameters $T_{\bar{c}_1}$ and $T_{\bar{c}_2}$, where $\bar{c}_1 = 1/3$ and $\bar{c}_2 = 2/3$. In the case *ER – ER*, the values $T_L = R_L = 1000, T_R = R_R = 100$ have been adopted.

4. THE INFLUENCE OF INTERMEDIATE TRANSLATIONAL RESTRAINTS

As stated in Section 1, in the determination of an additional translational restraint required to maximize a natural frequency, Courant and Hilbert have demonstrated that the optimum location of a support should be at the nodal points of a higher vibration mode, and Akesson and Olhoff have demonstrated the same for elastic supports.^{29,30} For this reason in all the described cases in this study, the restraint locations coincide with the nodal points of some higher modes.

First the case of an *SS – SS* beam without hinges and with one flexible support at the mid-point is considered ($\bar{c}_1 = 0, \bar{c}_2 = \bar{c}, \bar{c} = 0.5$). Fig. 2 the first two exact values of the frequency parameter λ are plotted against the restraint parameter $T_{\bar{c}}$. It is observed that the curves have a contact point denoted by P_1 , and to this point it corresponds with a value, namely $T^{(1,2)}$ of $T_{\bar{c}}$, such that over it the values of λ_1 cannot be raised

BC	\bar{c}_1	\bar{c}_2	λ_1		λ_2		λ_3	
<i>F – F</i>	0.2	0.6	1.375081		1.643200		9.362790	
	0.25	0.75	1.337032		1.618163		8.120665	
	1/3	2/3	1.414102		1.638014		10.669474	
	0.5	0.75	1.445185		1.681667		8.680980	
<i>SS – SS</i>	0.2	0.6	1.342282		1.583975		8.273242	
	0.25	0.75	1.315682		1.565026		7.855269	
	1/3	2/3	1.377333		1.564958		9.424777	
	0.5	0.75	1.390513		1.608228		7.173072	
<i>C – C</i>	0.2	0.6	3.772331		6.656591		9.738941	
	0.25	0.75	4.686472		6.031293		8.680536	
	1/3	2/3	4.248089		4.958357		10.740080	
	0.5	0.75	3.324057		6.124616		8.655705	

Table 1. Values λ_1, λ_2 and λ_3 of the frequency coefficient λ and mode shapes of a beam with two internal hinges with different symmetrical boundary conditions and values of the parameters $\bar{c}_i, i = 1, 2$. ($T_{\bar{c}_1} = T_{\bar{c}_2} = 1$).

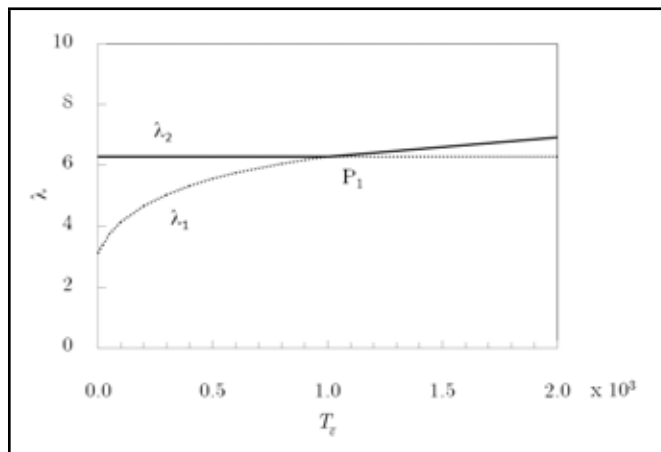


Figure 2. Variation of the first two exact values of the frequency parameter λ as a function of the translational restraint parameter $T_{\bar{c}}$, which corresponds to an *SS – SS* beam with $\bar{c} = 0.5$.

further whereas the values of the coefficient λ_2 increases. This phenomenon suggests the possibility of a change in the corresponding mode shapes, and it can also be observed in the case of the upper eigenvalues.

Based on the concepts presented, a numerical procedure

$T_{\bar{c}}$	λ_1	λ_2
0	3.14159265	6.28318531
$T^{(1,2)} - \varepsilon$	6.28318520	6.28318531
$T^{(1,2)} = 995.9135$	6.28318531	6.28318531
$T^{(1,2)} + \varepsilon$	6.28318531	6.28318541

Table 4. Values λ_1, λ_2 of the frequency coefficient λ and mode shapes of an *SS – SS* beam with $T^{(1,2)} = 995.9135$ and $\bar{c} = 0.5$.

has been developed with the purpose of determining the critical value $T^{(1,2)}$ of $T_{\bar{c}}$, which consists in the replacement of the values of λ_2 and \bar{c} into Eq. (21). In this case the value $T^{(1,2)} = 995.9135$ has been obtained.

Table 4 depicts the first two exact values of the frequency coefficient λ and the corresponding mode shapes of an *SS – SS* beam with $\bar{c} = 0.5$, for different values of the restraint stiffness $T_{\bar{c}}$. It is observed that the modes which correspond to λ_1 for

BC	\bar{c}_1	\bar{c}_2	λ_1	λ_2	λ_3
<i>C – F</i>	0.2	0.6	1.438556	6.609714	9.735284
	0.25	0.75	1.444605	5.385415	8.439022
	1/3	2/3	1.505427	4.639534	10.705621
	0.5	0.75	1.616772	3.382267	8.626570
<i>SS – AA</i>	0.2	0.6	1.391308	6.521151	8.583106
	0.25	0.75	1.413622	5.353031	8.319202
	1/3	2/3	1.456066	4.624047	9.810502
	0.5	0.75	1.564002	3.375018	8.611874
<i>ER – ER</i>	0.2	0.6	3.200393	5.459548	6.224496
	0.25	0.75	3.661568	5.060301	7.209206
	1/3	2/3	3.508990	4.478442	6.445352
	0.5	0.75	3.266975	4.056564	7.364875

Table 2. Values λ_1 , λ_2 and λ_3 of the frequency coefficient λ and mode shapes of a beam with two internal hinges with different non-symmetrical boundary conditions and values of the parameters $\bar{c}_i, i = 1, 2$. ($T_{\bar{c}_1} = T_{\bar{c}_2} = 1$). The case *ER – ER* is defined by $T_L = R_L = 1000, T_R = R_R = 100$.

$T_{\bar{c}} = 0$ and $T_{\bar{c}} = T^{(1,2)} - \varepsilon$ are symmetric while the second mode are anti-symmetric. Nevertheless, when $T_{\bar{c}} = T^{(1,2)} + \varepsilon$, the first mode is anti-symmetric, and the second mode is symmetric. Obviously ε assumes a small value. It can also be observed that as $T_{\bar{c}}$ increases, the first modal shape presents inflection points as it is illustrated by the figure which corresponds to the case $T^{(1,2)} - \varepsilon$. The corresponding mode shapes are analog until $T_{\bar{c}} = T^{(1,2)}$. In this process we have that $\lambda_1 \rightarrow \lambda_2$ from the left $T_{\bar{c}}$ increases in the interval $[0, T^{(1,2)}]$. When $T_{\bar{c}} > T^{(1,2)}$ there is a change: the values of λ_1 remain constant meanwhile the values of λ_2 increase as $T_{\bar{c}}$ increases, and the original second mode ($T_{\bar{c}} = 0$) becomes the new first mode, (i.e., the mode shape which corresponds to λ_1 when $T_{\bar{c}} > T^{(1,2)}$, is identical to the mode shape which corresponds to λ_2 when $T_{\bar{c}} = 0$).

The described phenomenon can be generalized by arguing that there exists a critical value $T^{(i,i+1)}$ of $T_{\bar{c}}$ where $\lambda_i = \lambda_{i+1}, \forall i$. The equality of eigenvalues can be explained through the existence of roots of multiplicity of the frequency Eq. (21). The procedure to obtain the values $T^{(i,i+1)}$, is analogous to that used for $T^{(1,2)}$.

In order to analyse the variation of the parameters λ_2 and

$T_{\bar{c}}$	λ_2	λ_3
0	6.28318531	9.42477796
$T^{(2,3)} - \varepsilon$	9.42477792	9.42477796
$T^{(2,3)} = 3354.9547$	9.42477796	9.42477796
$T^{(2,3)} + \varepsilon$	9.42477796	9.42477800

Table 5. Values λ_2, λ_3 of the frequency coefficient λ and mode shapes of a *SS – SS* beam with $T^{(2,3)} = 3354.9547$ and $\bar{c} = 1/3$.

λ_3 , it must be noted that the elastic restraint must be located at the point which coincides with the node of the modal shape which corresponds to λ_3 . In consequence, it is necessary to adopt $\bar{c} = 1/3$. By applying the procedure described above the value $T^{(2,3)} = 3354.9547$ has been obtained. Table 5 depicts the corresponding values and mode shapes.

In the cases that correspond to a beam that is clamped

BC	$T_{\bar{c}_1}$	$T_{\bar{c}_2}$	λ_1	λ_2	λ_3	λ_4	λ_5	λ_6
SS – SS	1	100	1.45611719	4.64282187	9.42477796	10.70691056	12.94235190	18.84955592
	100	100	4.31972616	4.90844437	9.42477796	10.74621939	12.98905869	18.84955592
	1000	100	4.55718873	7.66530463	9.42477796	11.07323213	13.48364215	18.84955592
	1000	1000	7.16349829	8.01393524	9.42477796	11.58970605	13.81448359	18.84955592
C – SS	1	100	4.28396838	4.93096581	9.81676729	11.83889375	13.76143072	19.22906792
	100	100	4.49969419	5.68516462	9.83627402	11.83894768	13.81211148	19.23144015
	1000	100	4.55795734	8.20313432	10.08227546	11.83943444	14.30200370	19.25413332
	1000	1000	7.28320226	8.44540826	10.19995164	12.40106641	14.46057634	19.26220167
ER – ER	1	100	4.25888244	4.74542202	6.69509498	8.93580767	11.66964943	15.09815518
	100	100	4.53063529	5.41229247	6.74864331	8.96276595	11.70947787	15.09913507
	1000	100	4.57054340	6.49115080	7.96847577	9.35593518	12.12807968	15.10746783
	1000	1000	5.57262634	7.47074935	8.42342470	9.99835788	12.28490310	15.24185358

Table 3. First six exact values of the frequency coefficient λ of a beam with two internal hinges, different boundary conditions, and intermediate points elastically restrained against translation located at $\bar{c}_1 = 1/3$ and $\bar{c}_2 = 2/3$. The case $ER - ER$ is defined by $T_L = R_L = 1000, T_R = R_R = 100$.

$T_{\bar{c}}$	λ_1	λ_2
0	3.42004348	5.03505659
$T^{(1,2)} - \varepsilon$	5.03483553	5.03505659
$T^{(1,2)} = 302.4782$	5.03505659	5.03505659
$T^{(1,2)} + \varepsilon$	5.03505659	5.03540105

Table 6. Values λ_1, λ_2 of the frequency coefficient λ and mode shapes of an $ER - ER$ beam ($T_L = R_L = 1000, T_R = R_R = 100$) with a free hinge located at $\bar{c}_1 = 0.5$. ($T^{(1,2)} = 302.4782, \bar{c}_2 = 0.617515$).

at $x = 0$ and simply supported at $x = l$ and to a beam with ends elastically restrained against rotation and translation ($T_L = R_L = 1000, T_R = R_R = 100$), the pairs $\lambda_1, \lambda_2, \lambda_2, \lambda_3$ and λ_3, λ_4 show the same features as those cases described previously. For brevity, the corresponding tables and figures are not included.

It is possible here to use the property of the boundary value problem described in Section 2 which allows to include one hinge located at \bar{c}_1 and an elastic restraint located at a different point \bar{c}_2 . Table 6 depicts the exact values λ_1 and λ_2 of the frequency coefficient λ and the corresponding mode shapes of an $ER - ER$ beam ($R_L = T_L = 1000, R_R = T_R = 100$) with a free hinge located at $\bar{c}_1 = 0.5$ and the elastic restraint located at $\bar{c}_2 = 0.617515$ with $T^{(1,2)} = 302.4782$. The phenomenon of change of frequencies and mode shapes is analogous to the case that corresponds to a beam without hinge.

5. CONCLUSIONS

Hamilton’s principle has been rigorously applied to obtain the boundary value problem and particularly the transition conditions, of a beam with two arbitrarily located internal hinges, four intermediate elastic support and ends elastically restrained against rotation and translation. Also a simple and accurate approach has been developed for the determination of natural frequencies and the mode shapes of free vibration. The mathematical model allows the inclusion of a hinge located at a point c_i and a translational restraint located at a different point

c_j . This property permits to study the influence on frequencies and mode shapes of varying intermediate supports, located at the nodal points of higher modes. It has been demonstrated that the existence of a critical value of the dimensionless restraint parameter, which determines a particular behaviour of frequency parameters and the presence of mode shape switching. It has also been demonstrated that the eigenvalues and mode shapes show some of the same features when there are internal hinges.

ACKNOWLEDGMENTS

The present investigation has been sponsored by CONICET Project P 242.

REFERENCES

- Mabie, H., and Rogers, C. B. Transverse vibrations of tapered cantilever beams with end support, *J. Acoust. Soc. Am.*, **44**(6), 1739–1741, (1968).
- Mabie, H., and Rogers, C. B. Transverse vibrations of double-tapered cantilever beams, *J. Acoust. Soc. Am.*, **57**(51), 1771–1774, (1972).
- Lee, W. Vibration frequencies for a uniform beam with one end spring hinged and carrying a mass at the other free end, *J. Appl. Mech.*, **40**(3), 813–815, (1973).
- Mabie, H., and Rogers, C. B. Transverse vibrations of double-tapered cantilever beams with end support and with end mass, *J. Acoust. Soc. Am.*, **55**(5), 986–991, (1974).
- Grant, A. Vibration frequencies for a uniform beam with one end elastically supported and carrying a mass at the other end, *J. Appl. Mech.*, **42**(2), 878–880, (1975).
- Hibbeler, C. Free vibration of a beam supported with unsymmetrical spring-hinges, *J. Appl. Mech.*, **42**(2), 501–502, (1975).
- Maurizi, R., Rossi, R. and Reyes, J. Vibration frequencies for a uniform beam with one end spring hinged and subjected to a translational restraint at the other end, *J. Sound Vib.*, **48**(4), 565–568, (1976).

- 8 Goel, P. Free vibrations of a beam-mass system with elastically restrained ends, *J. Sound Vib.*, **47**(1), 9–14, (1976).
- 9 Goel, P. Transverse vibrations of tapered beams, *J. Sound Vib.*, **47**(1), 1–7, (1976).
- 10 Grossi, R. O. and Laura, P. A. A. Further results on a vibrating beam with a mass and spring at the end subjected to an axial force, *J. Sound Vib.*, **84**(4), 593–594, (1982).
- 11 Laura, P. A. A., Grossi, R. O. and Alvarez, S. Transverse vibrations of a beam elastically restrained at one end and with a mass and spring at the other subjected to an axial force, *Nucl. Eng. Des.*, **74**(2), 299–302, (1982).
- 12 Cortinez, H. and Laura, P. A. A. Vibration and buckling of a non-uniform beam elastically restrained against rotation at one end and with concentrated mass at the other, *J. Sound Vib.*, **99**(1), 144–148, (1985).
- 13 Laura, P. A. A. and Gutierrez, R. H. Vibrations of an elastically restrained cantilever beam of varying cross section with tip mass of finite length, *J. Sound Vib.*, **108**(1), 123–131, (1986).
- 14 Grossi, R. O., Bhat, R. B., A note on vibrating tapered beams, *J. Sound Vib.*, **147**(1), 174–178, (1991).
- 15 Grossi, R. O., Aranda, A. and Bhat, R. B. Vibration of tapered beams with one end spring hinged and the other end with tip mass, *J. Sound Vib.*, **160**(1), 175–178, (1993).
- 16 Nallim, L. and Grossi, R. O. A general algorithm for the study of the dynamical behaviour of beams, *Appl. Acoust.*, **57**(4), 345–356, (1999).
- 17 Rao, C. K. and Mirza, S. A note on vibrations of generally restrained beams, *J. Sound Vib.*, **130**(3), 453–465, (1989).
- 18 Blevins, R. D. Formulas for Natural Frequency and Mode Shape, *Krieger Publishing Company*, Malabar, Florida, (1993).
- 19 Karnovsky, I. A. and Lebed, O. I. Free Vibrations of Beams and Frames, *Mc Graw-Hill*, New York, (2004).
- 20 Lee, W. F. Z. and Saibel, E. Free vibration of constrained beams, *J. Appl. Mech.*, **19**(1), 471–477, (1952).
- 21 Rutemberg, A. Vibration frequencies for a uniform cantilever with a rotational constraint at a point, *J. Appl. Mech.*, **45**(2), 422–423, (1978).
- 22 Lau, J. H. Vibration frequencies and mode shapes for a constrained cantilever, *J. Appl. Mech.*, **51**(1), 182–187, (1984).
- 23 Maurizi, M. J. and Bambill, D. V. Free vibration of a clamped-clamped beam with an intermediate elastic support, *J. Sound Vib.*, **119**(1), 173–176, (1987).
- 24 Rao, C. K. Frequency analysis of clamped-clamped uniform beams with intermediate elastic support, *J. Sound Vib.*, **133**(3), 502–509, (1989).
- 25 De Rosa, M. A., Bells, P. M. and Maurizi, M. J. Free vibrations of stepped beams with intermediate elastic supports, *J. Sound Vib.*, **181**(5), 905–910, (1995).
- 26 Ewing, M. S. and Mirsafian, S. Forced vibrations of two beams joined with a non-linear rotational joint: clamped and simply supported end conditions, *J. Sound Vib.*, **193**(2), 483–496, (1996).
- 27 Arenas, B. and Grossi, R. O. Vibration frequencies for a beam with a rotational restraint in an adjustable position, *Appl. Acoust.*, **57**(3), 197–202, (1999).
- 28 Grossi, R. O. and Albarracín, C. Eigenfrequencies of generally restrained beams, *J. Appl. Math.*, **2003**(10), 503–516, (2003).
- 29 Courant, R. and Hilbert D. Methods of Mathematical Physics, Vol. **1**, Interscience, New York, (1953).
- 30 Akesson, B. and Olhoff, N. Minimum stiffness of optimally located supports for maximum value of beams eigenfrequencies, *J. Sound Vib.*, **120**(3), 457–463, (1988).
- 31 Wang, C. Y. Minimum stiffness of an internal elastic support to maximize the fundamental frequency of a vibrating beam, *J. Sound Vib.*, **259**(1), 229–232, (2003).
- 32 Wang, D., Friswell, M. I. and Lei, Y. Maximizing the natural frequency of a beam with an intermediate elastic support, *J. Sound Vib.*, **291**(3–5), 1229–1238, (2006).
- 33 Albarracín, C., Zannier, L. and Grossi, R. O. Some observations in the dynamics of beams with intermediate supports, *J. Sound Vib.*, **271**(1–2), 475–480, (2004).
- 34 Wang, C. Y. and Wang, C. M. Vibration of a beam with an internal hinge, *Int. J. Struct. Stab. Dy.*, **1**(1), 163–167, (2001).
- 35 Chang, T. P., Lin, G. L. and Chang, E. Vibrations analysis of a beam with an internal hinge subjected to a random moving oscillator, *Int. J. Solids Struct.*, **43**(21), 6398–6412, (2006).
- 36 Grossi, R. O. and Quintana, M. V. The transition conditions in the dynamics of elastically restrained beams, *J. Sound Vib.*, **316**(1–5), 274–297, (2008).

Passive Vibration Isolation by Compliant Mechanism Using Topology Optimization

V. Vijayan

Mechanical Engineering Department, K.Ramakrishnan College of Engineering, Trichy, Tamilnadu—621 112, India

T. Karthikeyan

Mechanical Engineering Departments, Arulmurugan College of Engineering, Karur, Tamilnadu—639206, India

M. Udayakumar and K. Chellamuthu

Mechanical Engineering Department, K.Ramakrishnan College of Engineering, Trichy, Tamilnadu—621 112, India

(Received 11 June 2013; revised 9 May 2014; accepted: 3 June 2014)

Compliant mechanisms have been designed for various types of applications to transmit desired forces and motions. In this paper, we explore an application of compliant mechanisms for passive vibration isolation systems. For this, a compliant isolator is used to cancel undesired disturbances, resulting in attenuated output amplitude. A compliant mechanism is equipped with an isolator, while a compliant mechanism also functions as a transmission of force and controls the amount of displacement that is transmitted from it. It can be used as passive vibration isolation. Here, by introducing compliance into the connection, the transmission of applied forces is reduced at some frequencies at the expense of increasing transmission at other frequencies. While transmitted force is the key parameter from the receiver's perspective, motion at the isolated machine is uninteresting. The force transmissibility is numerically identical to the motion transmissibility. The structural optimization approach is focused on the determination of the topology, shape, and size of the mechanism. The building blocks are used to optimize a structure for force transmission. The flexible building blocks method is used for the optimal design of compliant mechanisms. This approach is used to establish the actuator model of the block and its validation by commercial finite element software. A library of compliant elements is proposed in FlexIn. These blocks are limited in number, and the basis is composed of 36 elements. The force transmitted to the rigid foundation through the isolator is reduced in order to avoid the transmission of vibration to other machines. The preliminary results of FEA from ANSYS demonstrate that compliant mechanism can be effectively used to reduce the amount of force transmitted to the surface.

NOMENCLATURE

δ_{st}	Static deflection, mm
k	Stiffness, N/m ²
m	Applied mass, kg
X	Displacement amplitude, mm
c	Damping coefficient
ω	Forcing frequency, rad/sec
ω_n	Natural frequency, rad/sec
I	area moment of inertia, mm ⁴
L	Length of strip, mm
R	Frequency ratio
η	Isolation efficiency
Tr	Transmissibility ratio
F_T	Force transmitted, kN
E	Young's modulus, N/m ²

1. INTRODUCTION

1.1. Compliant Mechanism

Compliant mechanism is the mechanism that relies on its own elastic deformation to transfer or transform motion or force.¹ Common compliant mechanisms function under the application of force at certain location (input) and generate a desired force or deflection at another location (output). Compliant mechanism is designed for passive vibration isolation system (PVIS). In this system, the existing element (i.e., the coil spring isolator) is replaced with the new designed element in order to reduce the amount of force transmitted to the ground or to the foundation of the machine, which tends continuously to damage the base over a longer period of time. This happens because the initial starting machine gives rise to huge amplitude up to the frequency ratio one. This region is identified as the amplification region, and during this, a large amount of vibration force is transmitted. By reducing the force transmit-

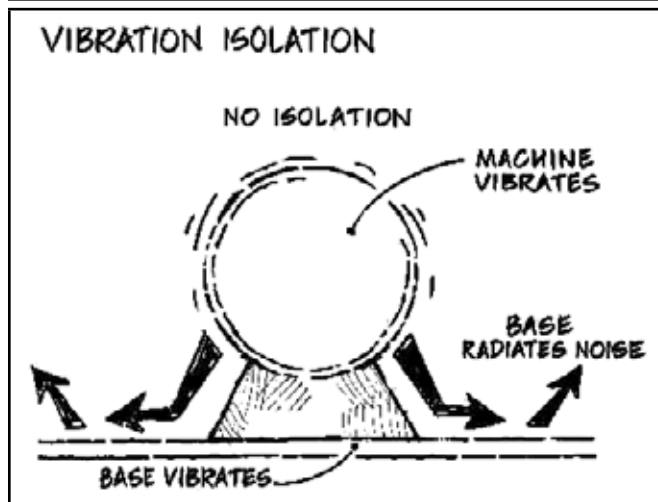


Figure 1. Directly mounted.

ted to the surface, one can increase the life of the base or the foundation of machine.

1.2. Topology Optimization

Homogenization based topology optimization is the basis for the design technique proposed in this research.²⁻⁴ Topology and size optimization methods are used to design compliant mechanisms, and the design procedure followed is based on the size optimization of the beam-element abstraction derived from the continuum topology solution.⁵ The topology optimization problem is formulated as a problem of finding the optimal distribution of materials in an extended fixed domain where some structural cost function is maximized.^{6,7} This work of topology optimization is carried out using ANSYS;^{8,9} by this, the optimum material distribution is obtained.¹⁰ Then the structural optimization¹¹ is done using flexible building blocks¹² designed by FlexIn Corporation. These elements are arranged in such a manner that to reduce the amount of force transmitted the trial and approximation method is used. Stability analysis in compliant mechanism design is of utmost importance. From a practical point of view, a CM that is unstable is of no significance. A stable system is defined as a system with a bounded system response. That is, if the system is subjected to a bounded input or disturbance, and the response is bounded in magnitude, the system is said to be stable.

1.3. Vibration Isolation

Vibrations are produced in machines that have unbalanced masses. These vibrations will be transmitted to the foundation upon which the machines are installed (see Fig. 1). This is usually undesirable. To diminish the transmitted forces, machines are usually mounted on springs or dampers as seen in Fig. 2, or on some other vibration isolation material. Vibration isolation reduces the level of vibration transmitted to or from a machine, building, or structure from another source.

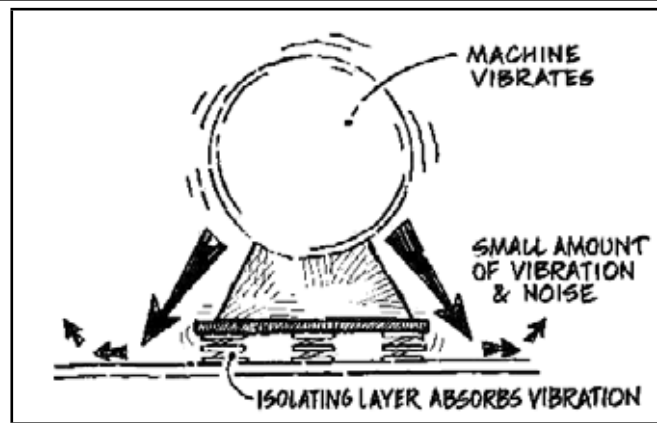


Figure 2. Mounted through isolators.

For damped system transmissibility

$$T = \sqrt{\frac{1 + \frac{R^2}{Q^2}}{(1 - R^2)^2 + \frac{R^2}{Q^2}}}; \tag{1}$$

$$R = \frac{f_e}{f_n}; \tag{2}$$

$$Q = \frac{1}{2C/C_C}. \tag{3}$$

1.4. Problem Formulation

Compliant mechanism is the focus of active research because of the stability, robustness, and ease of manufacturing endowed by their unitized construction. In this paper, we explore an application of compliant mechanism for a vibration isolation system with a rigid foundation. The structural optimization approach is focused on the determination of the topology, shape, and size of the mechanism. The building blocks are used to optimize a structure for force transmission.

1.5. Methodology

The displacement amplitude of the coil spring isolator is obtained for varying frequency ratios R (1.5–5). For the corresponding displacement amplitude, the force transmitted to the rigid foundation is determined. Then by using topology optimization and flexible building blocks, the vibration isolator is designed. The design is subjected to harmonic analysis using ANSYS software. For this design displacement amplitude and for the corresponding amplitude, the force transmission is calculated. For the coil spring isolator and compliant mechanism, isolation efficiency is determined and compared.

2. DESIGN OF COMPLIANT MECHANISM USING TOPOLOGY OPTIMIZATION AND BUILDING BLOCKS FOR VIBRATION ISOLATION

Topological optimization is a form of “shape” optimization sometimes referred to as “layout” optimization. The goal of topological optimization is to minimize/maximize the criteria

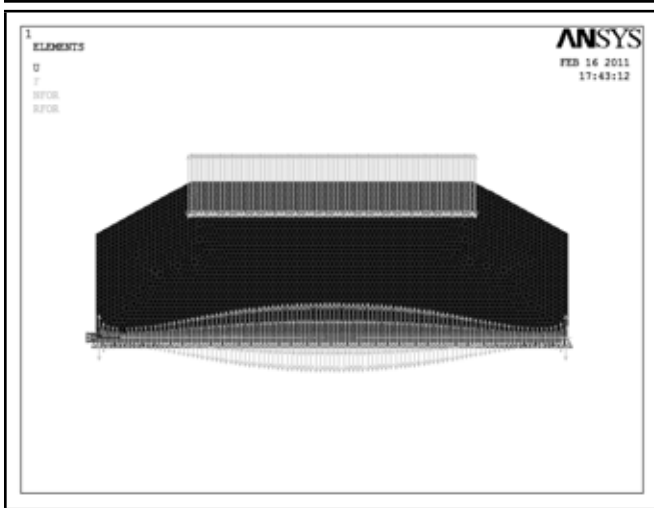


Figure 3. Meshed design domain.

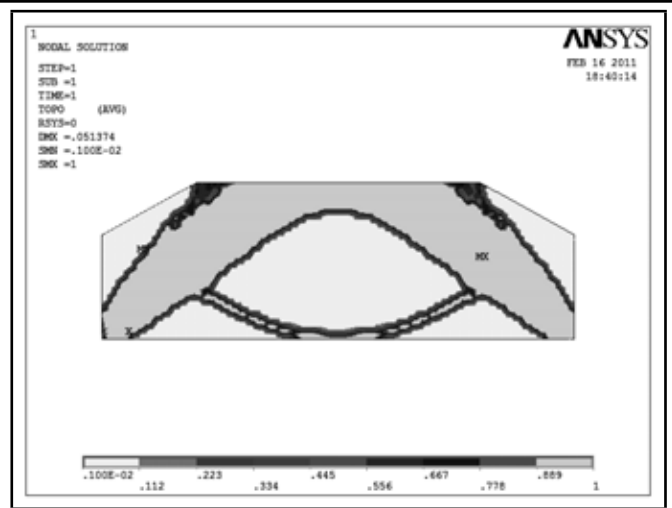


Figure 5. After 50% of volume reduction.

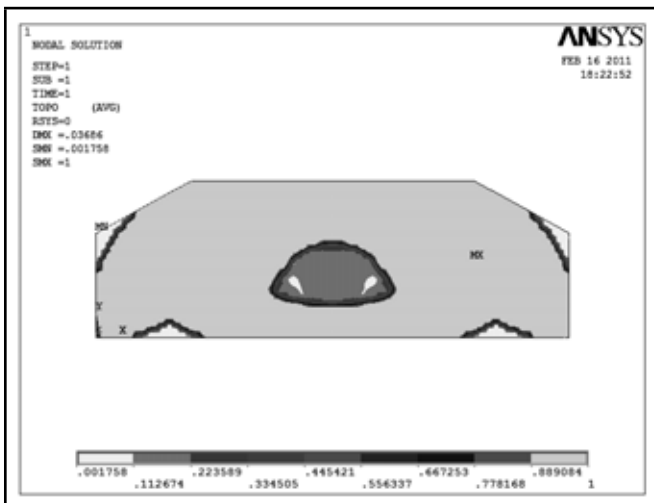


Figure 4. After 10% of volume reduction.

selected (minimize the energy of structural compliance, maximize the fundamental natural frequency, etc.), while satisfying the constraints specified (volume reduction, etc.).

The topology optimization predicts the optimal distribution of the material in the design domain. It is very promising for the systematic design of compliant mechanism because topological design is automated by the given prescribed boundary conditions.

The problem is defined for linear-elastic analysis. Then it is defined for material properties (Young’s modulus, Poisson’s ratio, and possibly the material density). Then the two types of element 2D planes for topological optimizations to generate a finite element model are selected. Load and boundary conditions for a single load case linear structural static analysis are shown in Fig. 3.

Figure 4 and Fig. 5 illustrate the volume constraints for the specific load of 85 kN, and the force transfer path is identified for structural size of 500 mm width and 165 mm height. The optimized path for the transfer of the maximum force is obtained using topology optimization.

2.1. Topology Optimization for Vibration Isolator Using FEA

In this example the boundary condition specified as all the corners of the design domain is fixed, and a point load is applied at the middle of the bottom face. The material property and the design variable and the domain dimension are given below in Table 1.

2.2. Compliant Building Blocks

The optimal design of compliant mechanisms made of an assembly of basic building blocks is chosen in a given library. A library of passive compliant elements is proposed in FlexIn. These blocks are limited in number: the basis is composed of 36 elements as shown in Fig. 6.

2.3. Creation of Building Blocks Library

A library of passive compliant elements made of piezoelectric beams has been implemented in FlexIn. As for passive blocks, a block stiffness matrix is constituted by the assembly of beams stiffness matrices in the global coordinate system. The blocks present some various topologies. Their advantage is that they can furnish multiple coupled degrees of freedom (Dofs), thus generating more complex movements with only one building block.

They are sufficient to constitute a high variety of topologies, and it has been verified that they can describe many existing compliant structures of the literature. Moreover, the block feasibility related to fabrication process constraints can also be taken into account at this stage, which is not the case for classical beam-based optimization approaches. From the library of passive compliant building blocks, the structure formed for the

Table 1. Specifications for topology optimization.

Design domain	500 mm × 305 mm × 165 mm
Young’s modulus	200 × 10 ⁹ N/m ²
Poisson’s ratio	0.29
Input force	85 kN
Upper limit of design variable	10 mm ²
Lower limit of design variable	0.1 mm ²

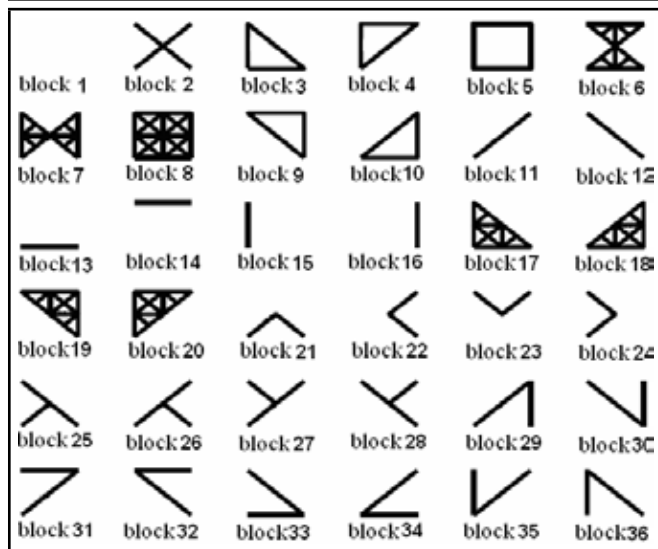


Figure 6. Library of compliant building blocks for planar compliant mechanisms synthesis using FlexIn.

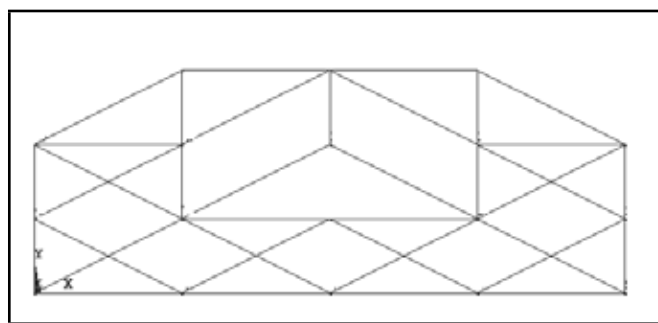


Figure 7. Structural optimization of isolator using flexible building blocks.

optimal distribution of the material distribution path for force transmission is determined using topology optimization. Figure 7 illustrates the use of flexible passive compliant building blocks in the path that maximum force transmissibility occurs.

2.4. Proposed Approach of Compliant Mechanism in Passive Vibration Isolation

We propose compliant mechanisms as a means to provide efficient and low cost vibration isolation. Due to their monolithic (jointless) construction, compliant transmissions offer many inherent benefits including low cost, zero backlash, ease of manufacture, and scalability. Although leaf springs and cantilever beams employed in previous research are in effect of “compliant mechanisms”, the motion amplification mechanism proposed in this research offers a more effective solution.

The scope of this study is limited to low-frequency isolation because the use of compliant mechanisms in active vibration isolation systems has the greatest advantage in the low frequency range.⁵ Since many passive systems are effective and sufficient for high-frequency isolation, the need of active systems for high-frequency isolation is less than that needed for low frequency isolation. We also focus on understanding the effects of the compliant design parameters and attempt to solve problems systematically. The preliminary results of FEA from

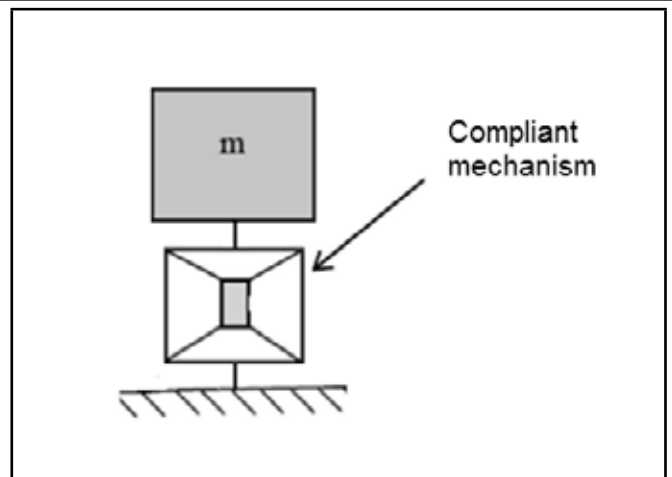


Figure 8. Models illustrating the concept of using a compliant mechanism in vibration isolation.

ANSYS demonstrate that compliant mechanism can be effectively used to reduce the amount of force transmitted to the surface. Figure 8 illustrates how compliant mechanism can be integrated into a vibration isolation system.

To achieve efficient vibration isolation, it is necessary to use a resilient support with sufficient elasticity so that the natural frequency of the isolated machine is substantially lower than the disturbing frequency, f_e , of vibration. The ratio R should be greater than 1.4 and ideally greater than 2 to 3 in order to achieve a significant level of vibration isolation. Damping provides energy dissipation in a vibrating system. It is essential to control the potential high levels of transient vibration and shock, particularly if the system is excited at, or near, its resonant frequency. When it is not possible to prevent or sufficiently lower the transmission of shock and vibration from the source, a resiliently supported foundation block can be used for the passive isolation of sensitive equipment.

2.5. The Existing Coil Spring Isolator (FSL Coil Spring Isolator)

Farrat Isolevel Ltd. (FSL) coil spring isolation systems are used to provide both active and passive vibration isolation with natural frequencies down to 3 Hz in order to isolate the disturbing frequencies down to 6 Hz. Table 2 shows the existing coil spring isolator specification.

In this preliminary study, the existing coil spring isolator is used to reduce the force transmitted from or to the machine. A compliant mechanism is designed to reduce the force transmitted to the foundation by reducing the displacement transmissibility of various frequency ratios. The model shown in

Table 2. Properties of the model used in finite element analyses.

Element type	2D elastic beam, 2D mass
Number of elements	37 elastic beam elements, 1 mass element attached at 17 th node
Young's modulus	200×10^9 N/m ²
Poisson's ratio	0.3
Density	7860 kg/m ³
Cross section	305 mm width \times 4 mm thickness
Overall dimension	500 \times 165 mm

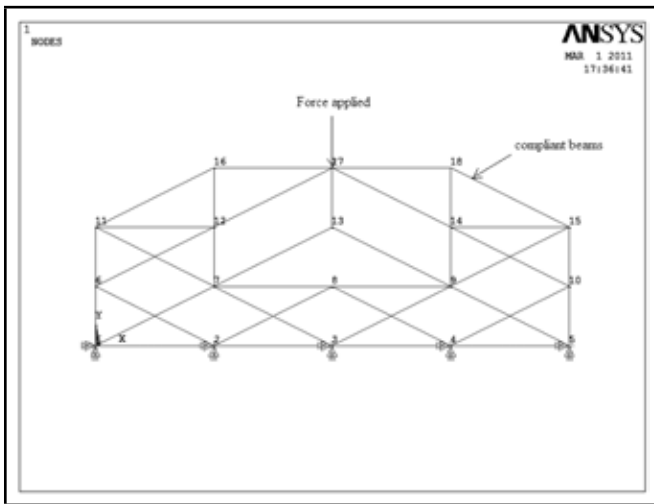


Figure 9. A finite element model of compliant mechanism.

Fig. 9 is designed with the load ranges from 85 kN–28 kN and constant K ranges from 3.4 kN/mm to 1.12 kN/mm; the free height of the structure is 165 mm, and the static deflection due to the self-weight of the load is $\delta_{st} = 25$ mm and 8 mm for the corresponding maximum and minimum load.

The compliant mechanism is assumed to be made of structural steel. The gravity and structural damping are ignored for these preliminary analyses. The motion of output is contributed by displacement controlled input.

2.6. Material Selection for Compliant Mechanism

Material for this compliant mechanism is selected based on the Young’s modulus, which includes natural frequency and the area moment of inertia, mass, and also the cross sectional area of a compliant beam. The following equations are used for material selection:

$$\text{Natural frequency of compliant mechanism } \omega_n = \sqrt{\frac{k}{m}}; \quad (4)$$

$$\text{Material constant } k = \frac{192EI}{l^3} = m\omega_n^2; \quad (5)$$

$$\text{Young’s modulus of the material is } E = \frac{m\omega_n^2 l^3}{192I}; \quad (6)$$

$$\text{Area moment of inertia } I = \frac{bh^3}{12}; \quad (7)$$

The size of the designed isolator is 500 mm × 305 mm × 165 mm.

From the given maximum load of 85 kN, the maximum mass acting on the isolator is $m = 8500$ kg, and the material constant is $k = 3400$ N. By varying the dimension of the width and height of the isolator using the area moment of inertia, the thickness of the compliant beams are determined. In this the width of the isolator is 305 mm. Table 3 shows the selection of material using Young’s modulus.

Here the optimum range of dimension is 305 mm × 4 mm which is having a Young’s modulus of 209×10^9 N/m². The required range of E value is around 200 Gpa. Figure 10 and Fig. 11 show the two dimensional and three dimensional respectively for the suggested optimum range of dimensions.

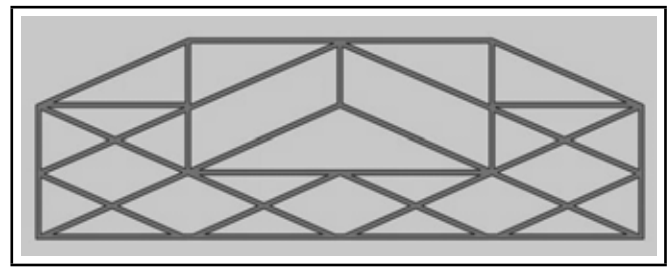


Figure 10. 2D compliant isolator design.

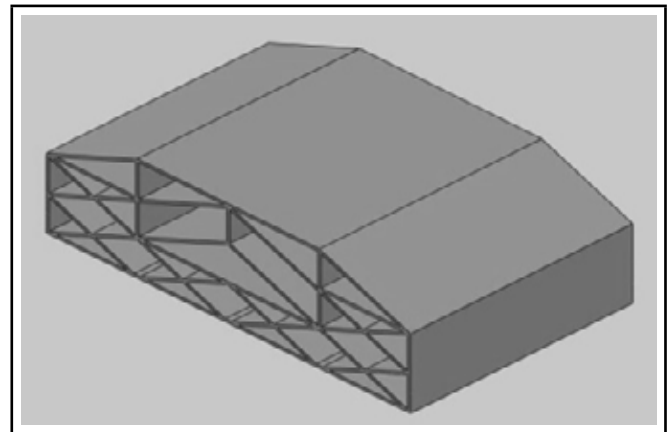


Figure 11. 3D compliant isolator design.

3. HARMONIC ANALYSIS

The harmonic response analysis solves the time-dependent equations of motion for linear structures undergoing steady-state vibration. The entire structure has constant or frequency-dependent stiffness, damping, and mass effects. All loads and displacements vary sinusoidally at the same known frequency. The element loads are assumed to be real (in-phase) only.

3.1. Harmonic Response of FSL Coil Spring Isolator

Initially the displacement amplitude shown in Fig. 12 is calculated for various frequency ratios from (1.5–5) for the damping ratio $\zeta = 0.3$ of the coil spring isolator. The forces transmitted in Fig. 13 for the corresponding amplitude and frequency ratios are also calculated.

3.1.1. Displacement Amplitude

The displacement amplitude is calculated by using the static displacement Eq. (8), the frequency ratio, and the damping ratio;

$$\frac{X}{\delta_{st}} = \frac{1}{\sqrt{(1 - R^2)^2 + (2\zeta R)^2}}. \quad (8)$$

Table 3. Selection of material using Young’s modulus.

S. No	Dimension, mm	Young’s modulus E , N/m ²
1	305 × 3	278×10^9
2	305 × 4	209×10^9
3	305 × 5	107×10^9
4	305 × 6	60×10^9
5	305 × 7	35×10^9

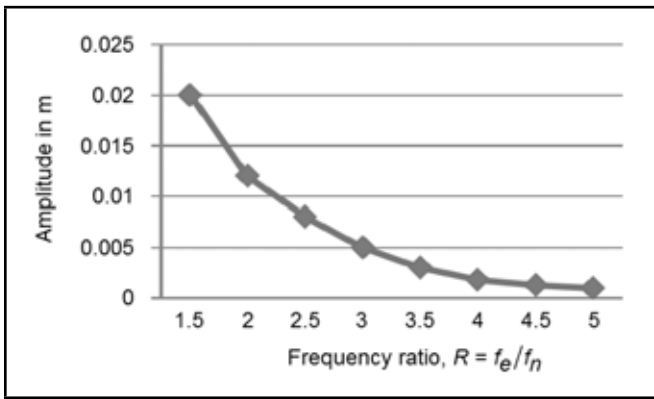


Figure 12. Amplitude for a different frequency ratio with a constant damping ratio $\zeta = 0.3$.

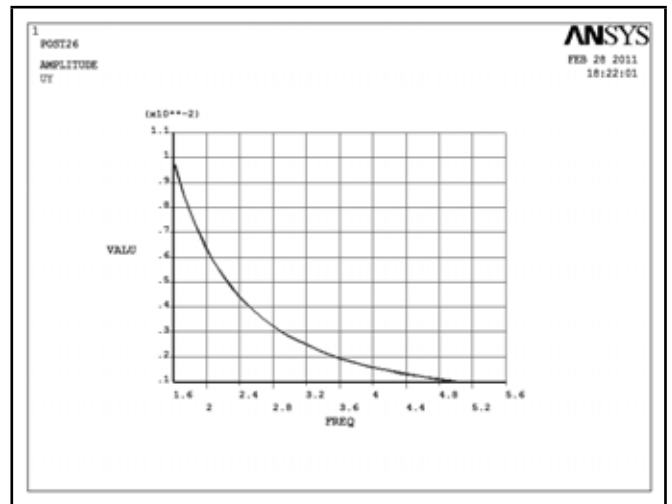


Figure 14. Displacement amplitude for corresponding frequency ratio ranges from R , (1.5–5) for compliant mechanism.

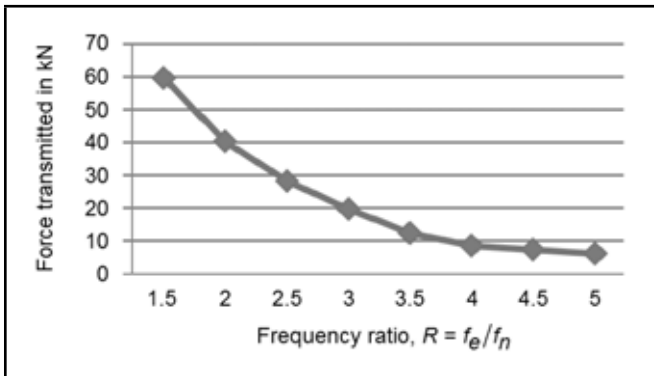


Figure 13. Force transmitted for the corresponding frequency ratio, R .

3.1.2. Force Transmitted

The force transmitted for the corresponding displacement amplitude is calculated by using the known material constant and the damping coefficient; it is taken as $\zeta = 0.3$ for the maximum value and the natural frequency of the coil spring isolator;

$$F_T = X\sqrt{(k^2 + c^2\omega^2)}. \quad (9)$$

3.2. Harmonic Response of Compliant Isolator

3.2.1. Displacement Amplitude

The displacement amplitude is calculated for compliant mechanism for various frequency ratios ranging from (1.5–5) with the damping ratio $\zeta = 0.3$ by using ANSYS as shown in Fig. 14.

3.2.2. Force Transmitted

The force transmitted (Fig. 15) for the corresponding amplitude and frequency ratios are also calculated by using Eq. (9).

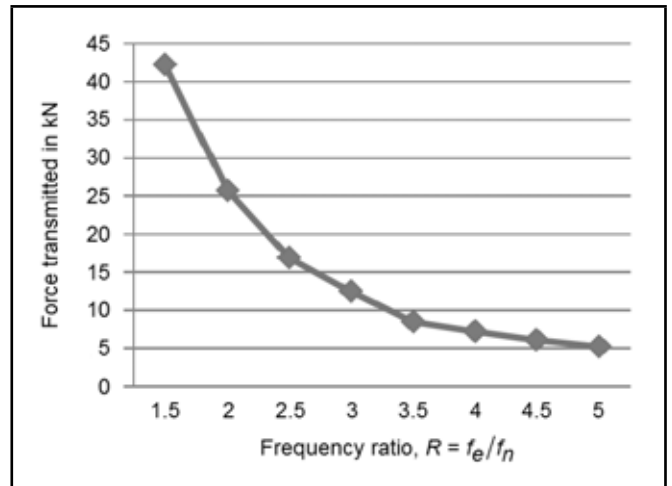


Figure 15. Force transmitted for varying frequency ratio.

motion at amplitude x and the absolute value of the mass response amplitude y expressed as a ratio $|y/x|$ is the Tr . Transmissibility Ratio $Tr = (\text{Force transmitted in kN} / \text{Disturbing force in kN})$.

4.2. Isolation Efficiency

Isolation efficiency η in percent transmission is related to transmissibility as

$$\eta = 100(1 - Tr)\%. \quad (10)$$

Isolation efficiency of the existing isolator and designed compliant mechanism is compared in Fig. 18.

5. CONCLUSION

Compliant mechanisms are proposed to provide cost effective and high performance vibration isolation systems. Their function is to transmit the force for various displacement amplitudes of corresponding frequency ratios. The preliminary results from FEA using ANSYS show that compliant mechanism can provide effective vibration isolation from a sinusoidal

4. RESULTS AND DISCUSSION

4.1. Transmissibility Ratio

The force transmitted by using compliant mechanism is compared with the existing isolator with the constant damping ratio $\zeta = 0.3$ as shown in Fig. 16. The sinusoidal foundation

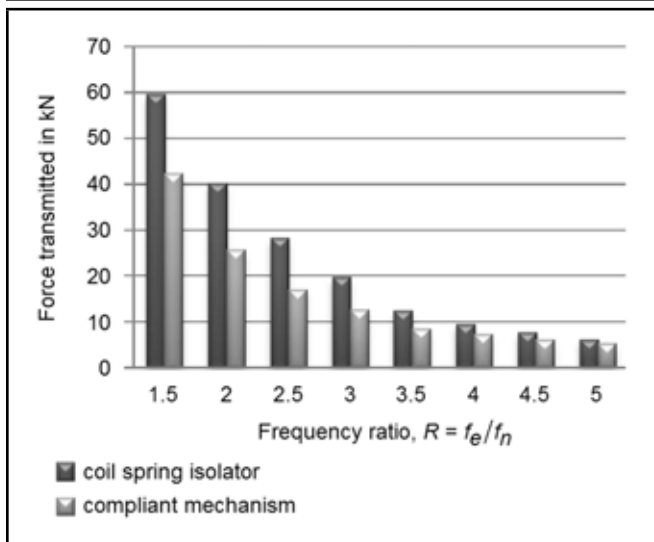


Figure 16. Force transmission of coil spring isolator with compliant mechanism.

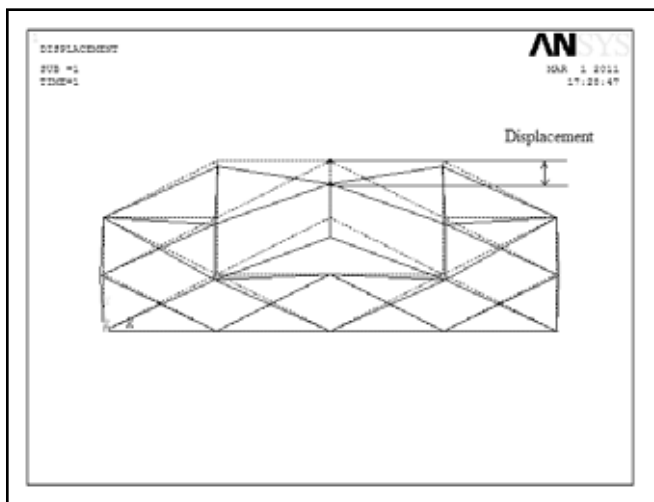


Figure 17. Displacement transmissibility for various frequency ratios.

disturbance with known frequency ratios. Both force transmissibility and amplitude transmissibility are discussed, as both of them have same results for validation purpose only.

In this research, we demonstrated, through harmonic analyses, that the disturbance of 0.01 m amplitude, the isolation efficiency of 56% is 1.5 Hz (for the coil spring isolator, the isolation efficiency for the corresponding amplitude and frequency ratio is 30%), and by 98%, it is at 5 Hz for the amplitude of 0.001 m (for the coil spring isolator, the isolation efficiency for the corresponding amplitude and frequency ratio is 93%), using compliant mechanism.

REFERENCES

- Howell, L. *Compliant Mechanisms*, Wiley, New York, (2001).
- Bendsoe, M. P. Optimal shape design as a material distribution problem, *Structural and multidisciplinary optimization*, **1**, 193–202, (1989).
- Burn, T. E. and Tortorelli, D. A. Topology optimization
- Pedersen, C. B., Buhl, T., and Sigmund, O. Topology synthesis of large-displacement compliant mechanisms, *International Journal for Numerical Methods in Engineering*, **50**, 2683–2705, (2001).
- Tantanawat, T., Li, Z., and Kota, S. Application of compliant mechanisms to active vibration isolation systems, *Proc. ASME 2004 International Design Engineering Technical Conferences*, Salt Lake City, USA, 1165–1172, (2004).
- Li, Y., Chen, B., and Kikuchi, N. Topology optimization of mechanism with thermal actuation, *Proc. 4th International Conference on ECO Materials*, Gifu, Japan, (1998).
- Sigmund, O. Design of multi-physics actuators using topology optimization—Part I: One material structures, *Computer Methods in Applied Mechanics and Engineering*, **190**, 6577–6604, (2001).
- Haftka, R. T. and Grandhi, R. V. Structural shape optimization—A survey, *Computer Methods in Applied Mechanics and Engineering*, **57**, 91–106, (1986).
- Ding, Y. Shape optimization of structures: A Literature Survey, *Computers and Structures*, **24**, 985–1004, (1986).
- Kikuchi, N. and Bendsoe, M. P. Generating optimal topologies in structural design using a homogenization method, *Computer Methods in Applied Mechanics and Engineering*, **71**, 197–224, (1988).
- Joo, J. Y. Nonlinear Synthesis of Compliant Mechanisms: Topology, Size and Shape Design, Ph.D. Dissertation, University of Michigan, (2001).
- Nastac, S. and Leopa, A. Structural optimization of vibration isolation devices for high performances, *International Journal of Systems Applications, Engineering & Development*, **2**, 66–74, (2008).

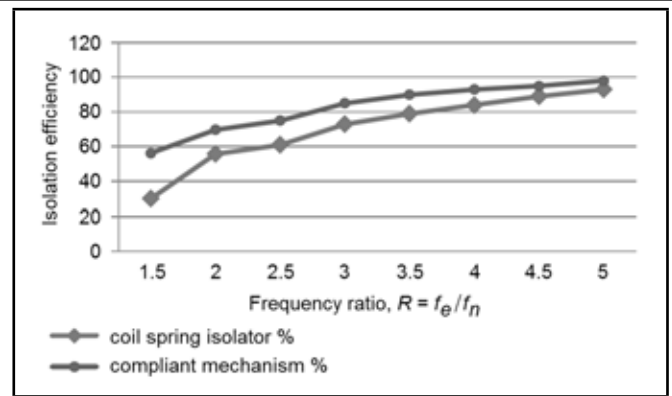


Figure 18. Isolation efficiency vs. frequency ratio.

of non-linear elastic structures and compliant mechanisms, *Computer Methods in Applied Mechanics and Engineering*, **190**, 3443–3459, (2001).

Blind Source Separation Research Based on the Feature Distance Using Evolutionary Algorithms

Yang Yang

School of Engineering, Bohai University, 121013, Jinzhou, China

Xiuqin Wang

Information Science and Technology School, Bohai University, 121013, Jinzhou, China

Di Zhang

Liaoning Datang International Jinzhou Power Generation Co., Ltd, 121001, Jinzhou, China

(Received 3 April 2012; revised: 28 August 2013; accepted: 14 January 2014)

Without any information on the mixing system, the blind source separation (BSS) technique efficiently separates mixed signals. The approach called evolutionary algorithms was used for the BSS problem in this paper. The fitness function based on the feature distance and kurtosis was proposed to measure the degree of the separated signals in this paper. Compared with the traditional algorithm in the BSS problem, the mathematical calculation and the physical significance of the separated signals are both taken into consideration in the proposed method. Therefore, the separated signals could have great correlation with the original individual signal and could be used in the additional signal processing step with good signal property. Experimental results on mixed spoken signals indicated that the established evolutionary algorithm of particle swarm optimization (PSO) and genetic algorithm (GA) could effectively solve the BSS problem from the signal feature distance and independence measurement. The study in this paper was implemented with MATLAB language.

1. INTRODUCTION

Without knowing the mixing processing and sources, blind source separation (BSS) deals with recovering a set of underlying sources from observations. The BSS problem is widely used in the fields of: image processing, acoustics signal separation, vibration signal separation, medical signal processing, biomedical data analysis, telecommunications, stock analysis and fault recognition.¹⁻³

In the literature, the theory of BSS has been approached in several ways and various algorithms have been proposed. For example, the methods were originally introduced in the context of neural network (NN) modelling, independent component analysis (ICA), principle component analysis (PCA), singular value decomposition (SVD), high order statistical cumulants and others. The most important and simplest of the methods mentioned above is ICA which has the goal of finding a suitable representation of non-Gaussian sources with all the most independent components as possible. Lots of ICA algorithms for BSS problems are proposed, including the minimization (or maximization) of a contrast function (for example Mutual Information and non-Gaussianity). ICA works with different algorithms, including FastICA algorithm, JADE (Joint Angle and Delay Estimation) algorithm, extended Infomax algorithm, and mean field approach ICA. The ICA method differs from other similar methods in that the components are both statistically independent and non-Gaussian. BSS is used for recovering unobserved signals from a known set of mixtures. Therefore, ICA and BSS are equivalent when the mixtures are

assumed to be linear up until possible permutations and invertible scalings.²⁻⁷

In the past, the NN model was the popular architecture for separation, but its performance depends strongly on the initiation of weight. In a previous study, the authors used the genetic algorithm (GA) for optimizing the weights of the NN system in order to enhance global convergence.⁸ In another study, a support vector machine (SVM) methodology is applied to ICA in the search for the separating matrix.⁵

According to a previous paper, through finding optimum and accurate coefficients of the separating matrix, the evolutionary algorithms can be the best solution for solving BSS problems. In this approach, the new population can be created where independence among its components is maximized if a suitable fitness function is used. There are two types of contrast functions of BSS: information theory and high order statistics. In this paper, the authors used two evolutionary algorithms, GA and PSO, for BSS, and the novel fitness function is based on the mutual information and high order statistics.²

In another paper the authors present a novel GA-ICA method which converges to the optimum.⁹ The new method uses GA to find the separating matrices, which are based on the contrast function to minimize a cumulant. In reference 10 the authors used the kurtosis of the mixed signal to the target function, by modifying PSO to replace the steepest gradient descent method. In reference 11 the learning rate of the BSS method is selected adaptively by using PSO. In reference 12 the authors introduce the evolution speed and the aggregation degree to update the dynamic inertia weight in PSO. In refer-

ence 13, for blind deconvolution and the deblurring of images, the method is based on a non-Gaussian measure of ICA along with the GA for optimization in the frequency domain.

In this paper, the BSS approach for linear mixed signals is studied to get the coefficients of the separating matrix by using evolutionary algorithms (PSO and GA). The operation of these algorithms principally depends on the fitness function by using the kurtosis and the feature distance, which will be defined later. We first constructed two mixed signals using two spoken word signals. The objective is to separate the signals from the mixed ones and this is a typical BSS problem. Then we used evolutionary algorithms to separate the mixed matrix. The simulation results showed that a good result can be obtained by using the feature distance combined with kurtosis as the fitness function. Kurtosis is a simple and necessary criterion for estimation dependency among signals. The proposed method not only uses the mathematical way to find the optimal matrix, but it also takes into consideration the signals' own characteristics, as can be seen in the feature distance definition. When the feature distance and the independence of estimated signals are at a maximum, the two signals are separated well. Other simulation results also showed that the proposed method is valid and can be used in the similar field.

2. BLIND SOURCE SEPARATION AND EVOLUTIONARY ALGORITHMS

2.1. BSS Problem Description

A series of observed signals is given, and BSS aims at recovering the underlying sources by using the assumption of their mutual independence. BSS can be classified as linear or nonlinear based on the type of mixing of the sources.

The BSS model considered in this paper is a linear simultaneous mixture in Eq. (1).

$$\mathbf{x} = \mathbf{A}\mathbf{s}; \tag{1}$$

where $\mathbf{x} = [x_1, x_2, \dots, x_m]^T \in R$ is a vector containing measured signals x_i , $\mathbf{s} = [s_1, s_2, \dots, s_n]^T \in R^n$ is a vector containing original sources ($m \geq n$), and $\mathbf{A} \in R^{m \times n}$ is an unknown mixing matrix with full column rank.¹ The linear model can also be expressed as in Eq. (2):

$$x_j(t) = a_{j1}s_1 + a_{j2}s_2 + \dots + a_{jn}s_n \quad \forall j = 1 \dots n. \tag{2}$$

Assume that the number of sources n is equal to that of mixtures m . For simplicity, the discussion here is restricted to the case of $m = n = 2$. In the experiment we will construct two mixed signals using two original spoken signals. Certain assumptions about sources are also needed in the BSS problem. The most general ones are:¹

1. Sources are mutually independent;
2. Sources are non-Gaussian or one Gaussian signal at most;
3. The mixing matrix is a full unknown column rank.

With the above assumptions, the BSS result has two inherent ambiguities:¹

1. The order of the estimated sources cannot be decided;
2. Original variances (energies) of sources are unknown.

Therefore, all the sources are generally assumed to have unit variances.¹

The matrix W (the separating matrix) whose output can be an estimate of the sources $s(t)$ is given in Eq. (3):

$$\mathbf{y} = \mathbf{W}\mathbf{x} \tag{3}$$

In ICA, a solution that maximizes the non-Gaussianity of the recovered signals is needed. Therefore, some ways to measure the non-Gaussianity are also required including negentropy and kurtosis.

Negentropy is used as a measure of distance to normality in information theory. The entropy of a discrete signal is equal to the negative sum of the products of the probability of each event and the log of those probabilities. Kurtosis is a classical method of measuring non-Gaussianity which is equal to the fourth moment of the data if the data is pre-processed with unit variance. In an intuitive sense, kurtosis is used to measure the "spikiness" of a distribution or the size of the tails. It is extremely simple to calculate but sensitive to outliers in the data set at the same time.¹³ Mathematically kurtosis, is defined in Eq. (4):¹³

$$Kurt(y) = E\{y^4\} - 3(E\{y^2\})^2. \tag{4}$$

If y has unit variance, we can obtain $Kurt(y) = E\{y^4\} - 3$. If x_1 and x_2 are random variables, $Kurt(x_1 + x_2) = Kurt(x_1) + Kurt(x_2)$ and $Kurt(ax) = a^4Kurt(x)$ are satisfied.

2.2. Particle Swarm Optimization (PSO)

The PSO method was developed by Eberhart and Kennedy in 1995.¹⁴ It simulates social behaviour to a promising position in order to achieve precise objectives in a multi-dimensional space. The PSO method has been applied in a wide variety of highly complicated optimizations in real-world problems. Like other evolutionary algorithms, PSO performs searches using a population (called a swarm) of individuals (called particles) that are updated from iteration to iteration. Each particle changes its search direction based on two factors to discover the optimal solution. The first one is its own best previous experience and the other one is the best experience of all other members.¹⁴⁻¹⁶

The basic process of the PSO algorithm is initialization, fitness, update, construction, and termination. The process of PSO is finished if the termination condition is satisfied. The details are given as follows:¹⁶

1. Generate initial particles randomly;
2. Measure the fitness of each particle in the population;
3. Compute the velocity of each particle;
4. Move to the next position for each particle;

5. Stop the algorithm if the termination criterion is satisfied; otherwise, return to Step 2.

The position vector and the velocity vector of i th particle in an m -dimensional search space can be represented as $x_i(i = 1, 2, \dots, N)$ and $v_i(i = 1, 2, \dots, N)$ respectively; N represents the number of particles.

In the PSO algorithm, the new velocities of other particles are updated by Eqs. (5) and (6).

$$v_i(t + 1) = \omega v_i(t) + c_1 r_1 (p_i(t) - x_i(t)) + c_2 r_2 (p_g(t) - x_i(t)); \quad (5)$$

$$x_i(t + 1) = x_i(t) + v_i(t + 1); \quad (6)$$

where v_i is the velocity of the i th particle of the swarm, x_i is the position in the search space. p_i is the best position of the i th particle, p_g is the global best particle, ω is the inertia weight of velocity, c_1 and c_2 are the acceleration coefficients, and r_1 and r_2 are two different, uniformly distributed random numbers in the range of $[0, 1]$. The potential of the solution is measured by the fitness function in our paper. More details about the PSO algorithm can be seen in the reference section.^{8,17-19}

2.3. Genetic Algorithm (GA)

The GA is one of the most popular stochastic optimization techniques nowadays. The GA method is inspired by the natural genetics and biological evolutionary process. Three basic operators are used to manipulate the genetic composition of a population: reproduction, crossover and mutation. The GA evaluates a population and generates a new one iteratively with each successive population (generation).⁶

The goal is to solve the optimization problem. Here, the chromosome is written as an array with an n -dimensional optimization problem and can be seen in Eq. (7).²⁰

$$chromosome = [p_1, p_2, p_3, \dots, p_n]. \quad (7)$$

Each chromosome has a cost found by evaluating the fitness function f at the variables $p_1, p_2, p_3, \dots, p_n$.

$$f(chromosome) = f(p_1, p_2, p_3, \dots, p_n) \quad (8)$$

The GA algorithm is characterized as follows:⁶

1. Encodes solutions to a problem in the form of a chromosome;
2. Initializes the population for the chromosomes procedure;
3. Evaluates fitness function;
4. Manipulates the composition of the population using genetic operators;
5. Provides the initial settings of the population size and probabilities employed by the genetic operators.

3. EXPERIMENTS

In the experiment, two spoken word signals (*kiss1* and *love1*) were used as the individual signals.²¹ Suppose that $y1$ is the name of the *kiss1* signal and $y2$ is the name of the *love1* signal. We know that two spoken word signals do not have the same length most of time. Therefore, we add several zero values at the end of the short signal to make their length same. Then two mix signals were constructed, which are $mix1 = 0.3 * y1 + 0.5 * y2$ and $mix2 = 0.4 * y1 + 0.3 * y2$. The mixed signals are the weighted sums of the original spoken signals; the weights depend upon the distances between the source signals and the microphones. Here the mixing matrix was chosen randomly. The unknown matrix is square, and the mixing can be characterized by a linear scenario. The objective is to separate the individual signals from the mixed ones, and this is a typical BSS problem. The recovered signals are called $ys1$ and $ys2$ in this paper.

3.1. Fitness Evaluation-Kurtosis

Kurtosis is used to measure the degree of the non-Gaussian property of the signals. The common evolutionary algorithm in the BSS problem is based on the kurtosis calculation. Pre-processing of the BSS data is needed before using kurtosis as the fitness function which contains two steps: centring and whitening.²

The fitness function is defined as follows in Eq. (9):

$$F(ys) = |kurt(ys1)| + |kurt(ys2)|$$

$$fitness = -F(ys) \quad (9)$$

The kurtosis of a distribution in MATLAB 7.0 is defined in Eq. (10):

$$k = \frac{E(x - \mu)^4}{\sigma^4} \quad (10)$$

where μ is the mean of x , σ is the standard deviation of x , and $E(t)$ represents the expected value of the quantity t .

3.2. Fitness Evaluation- Feature Distance

As signal has its own characteristic and features vectors that can help distinguish speech signals. There is more than one way to choose the feature vectors. For the spoken signals, DFT coefficients were used as features.² Other popular alternatives include the parameters from an AR modelling of the speech segment and the cepstral coefficients (the inverse DFT of the logarithm of the magnitude of the DFT coefficients). In the experiment, the AR modelling method was selected as the feature. When the feature distance of two recovered signals is at its maximum, the two signals are separated well by the algorithm.

The feature distance is defined in Eq. (11):

$$F(ys) = \sum_{j=1}^m (|f(ys1)| - |f(ys2)|); \quad (11)$$

where f is the feature function, and m is the number of the feature vectors. The fitness function is defined in Eq. (12).

$$fitness = -F(ys) \quad (12)$$

3.3. Fitness Evaluation– kurtosis and feature distance

With the advantage of kurtosis and feature distance as the fitness function, the separated signal can have both physical significance and the independence property. Therefore, we proposed a new fitness function combined with kurtosis and feature distance to improve the algorithm; it is defined in Eq. (13):

$$F(ys) = |k(ys_1)| + |k(ys_2)| + \sum_{j=1}^m (|f(ys_1)| - |f(ys_2)|)$$

$$fitness = -F(ys); \tag{13}$$

where f is the feature function and m is the number of the feature vectors.

3.4. Simulation Result

We individually used Particle Swarm Optimization (PSO) and the Generic Algorithm (GA) to settle the BSS problem.

In the PSO method, the particles were used in the separating matrix. Here we chose the learning factor synchronization of the PSO algorithm to separate the mixed spoken signals in the experiment. Three fitness functions were used to test the algorithm. The waveforms of the source signals and the recovered signals can be seen from Fig. 1 to Fig. 3.

Kurtosis(y1)=26.9992

Kurtosis(y2)=30.4246

Kurtosis(ys1)=30.4824

Kurtosis(ys2)= 27.0729

Fitness function value= -57.4238 (expected value)

Fitness function value= -57.5553 (experimental value)

Fitness function value = -6.6461 (expected value)

Fitness function value = -6.6728 (experimental value)

Fitness function value = -64.0699(expected value)

Fitness function value = -64.1792 (experimental value)

In the GA method, the program was written with the Genetic Algorithm Tool in MATLAB. The population size was 40, the variable number which used in the separating matrix was 4 and the other parameters were by default. Three fitness functions were also used to test the algorithm we proposed in the paper.

Kurtosis(y1)= 26.9992

Kurtosis(y2)= 30.4246

Kurtosis(ys1)= 27.0767

Kurtosis(ys2)= 30.4782

Fitness function value = -57.4238 (expected value)

Fitness function value = -57.5548 (experimental value)

Fitness function value = -6.6461(expected value)

Fitness function value = -6.6439 (experimental value)

Fitness function value = -64.0699(expected value)

Fitness function value = -64.1792 (experimental value)

The recovered signals ys_1 and ys_2 were obtained by using the optimal separating matrix, whose figures can be seen in Figs. 4 to 6. Compared with the classical ICA algorithm 2 (FastICA, Hyvarinen’s fixed-point algorithm). The signals can be seen in Fig. 7.

In order to evaluate and compare the performance of BSS, the correlation analysis and the source to distortion ratio (SDR)

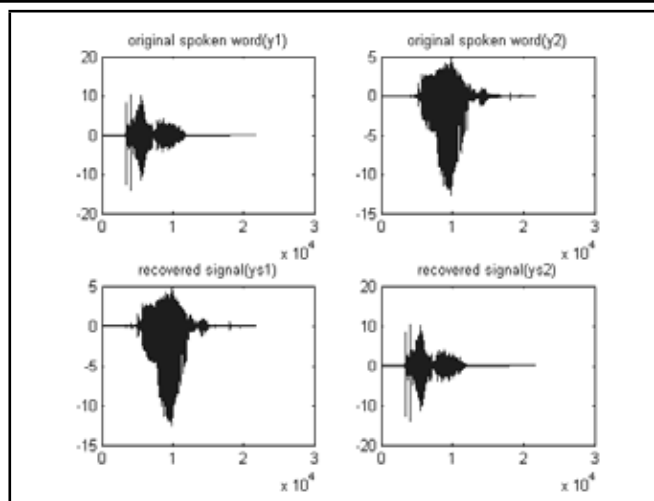


Figure 1. PSO-kurtosis

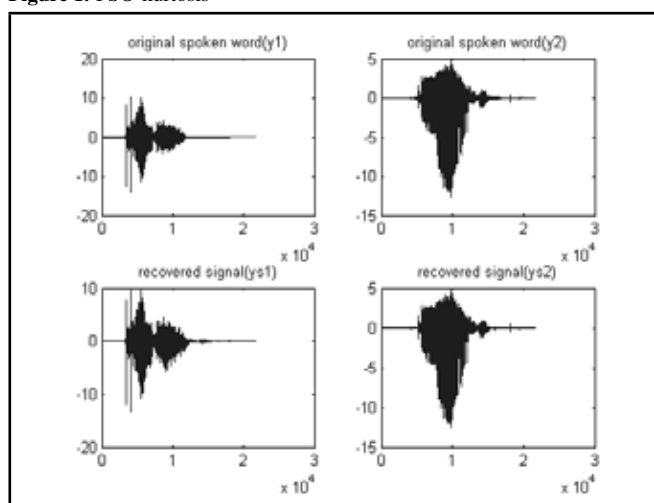


Figure 2. PSO-feature distance

were used to verify the similarity between the source signals y_i and separated signals ys_i with N samples. SDR is defined as in Eq. (14).

$$SDR(y_i, y_{si}) = 10 \log \left(\frac{\sum_{t=1}^N [y_i(t)]^2}{\sum_{t=1}^N [y_{si}(t) - y_i(t)]^2} \right); \tag{14}$$

where the larger the SDR is, the better the effect of separated signals is.

The experimental results of the PSO, GA, and FastICA method were given for comparison in Table 1.

From Table 1 we can see that, the proposed algorithm with the fitness of kurtosis and the feature distance has good results that are similar with FastICA. The key point in the performance of the evolutionary algorithm is the definition of the fitness function. The separated method in the paper uses not only the mathematical way to find the optimal matrix, but also takes into consideration the signals’ own characteristics. After doing the similarsimulation, the simulation result of the proposed method is still effective.

Table 1. Result analysis between the signals recovered and the source signals

Signals Recovered	Source Signals		SDR	algorithm
	y1	y2		
ys1	0.0259	0.9998	SDR(y1,ys2)= 31.7390	PSO
ys2	0.9997	0.0209	SDR(y2,ys1)= 33.6021	f: kurtosis
ys1	0.9592	0.3271	SDR(y1,ys2)= 10.8874	PSO
ys2	0.0447	1.0000	SDR(y2,ys1)= 53.7254	f: feature distance
ys1	0.0369	1.0000	SDR(y1,ys1)= 28.6550	PSO
ys2	0.9993	0.0099	SDR(y2,ys2)= 40.1285	f: feature distance& kurtosis
ys1	-0.9996	-0.0185	SDR(y1,ys2)= 30.9869	GA
ys2	0.0282	0.9998	SDR(y2,ys1)= 34.6346	f: kurtosis
ys1	0.0576	0.9999	SDR(y1,ys1)= 9.0815	GA
ys2	-0.9382	-0.3895	SDR(y2,ys2)= 39.2657	f: feature distance
ys1	0.0364	0.9999	SDR(y1,ys1)= 28.7721	GA
ys2	0.9993	0.0103	SDR(y2,ys2)= 39.7033	f: feature distance& kurtosis
ys1	0.0094	0.9993	SDR(y1,ys2)= 40.5799	FastICA
ys2	1.0000	0.0374	SDR(y2,ys1)= 28.5384	

Note: f means fitness function.

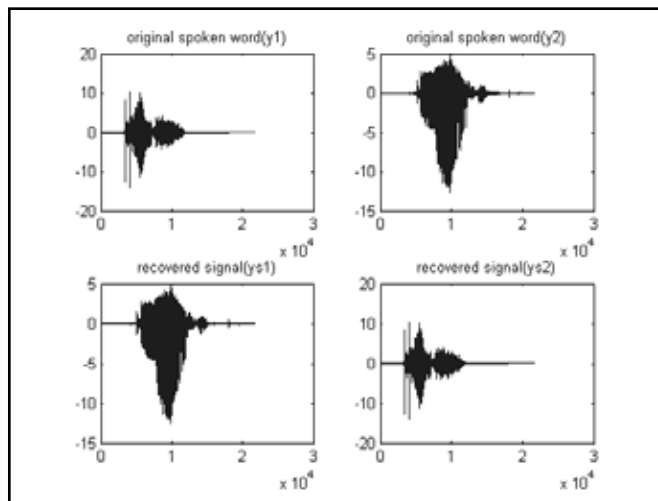


Figure 3. PSO-kurtosis and feature distance

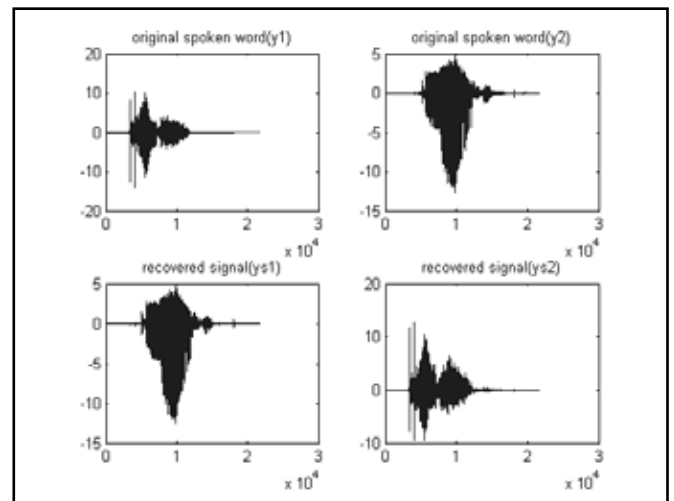


Figure 5. GA-feature distance

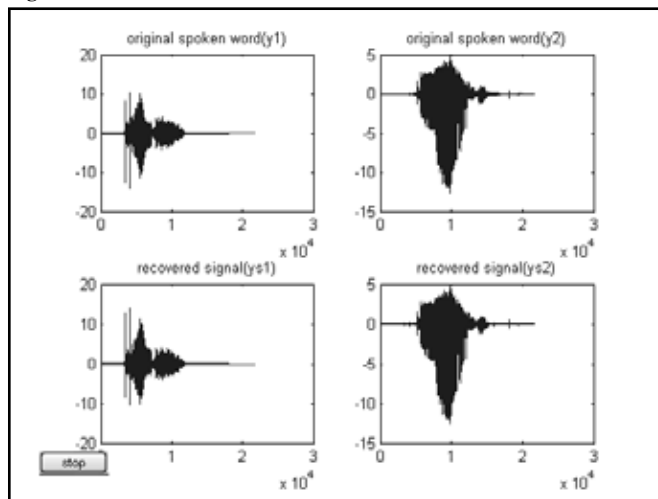


Figure 4. GA-kurtosis

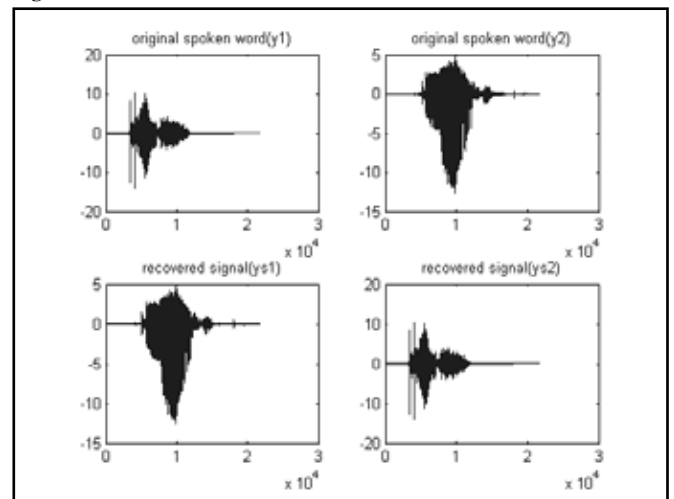


Figure 6. GA-kurtosis and feature distance

4. CONCLUSION

BSS is a good method for dealing with mixed signals. Individual source signals can be obtained if the separating assumptions are satisfied. By introducing the evolutionary method with the feature distance and kurtosis as the fitness function in the experiment, the separated signals can have both physical significance and the independence property. It can be widely used in the BSS problem, evolution algorithm, signal process-

ing, and similar research. Our further study will be the evolutionary algorithm on the nonlinear mixing models in the BSS problem.

ACKNOWLEDGEMENT

The authors thank the support of Education Department of Liaoning Province, China. The project number is L2010006.

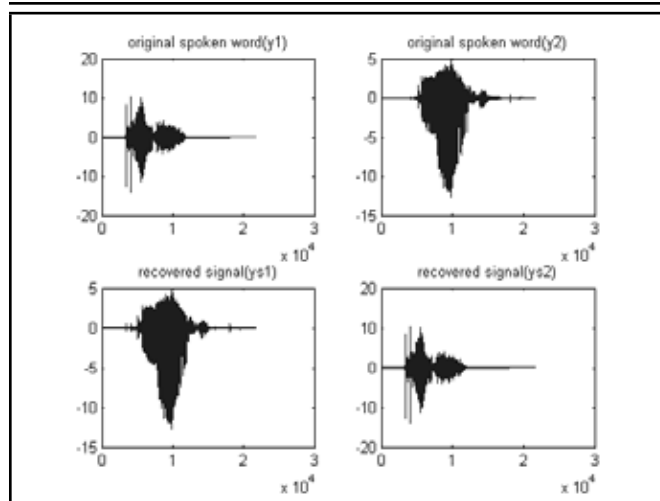


Figure 7. Fast-ICA

REFERENCES

- 1 Zhou, W. L. and Chelidze, D. Blind source separation based vibration mode identification, *Mechanical Systems and Signal Processing*, **21**(8), 3072–3087, (2007).
- 2 Mavaddaty, S. and Ebrahimzadeh, A. Research of Blind Signals Separation with Genetic Algorithm and Particle Swarm Optimization Based on Mutual Information, *Journal of Computer Engineering*, **1**, 77–88, (2009).
- 3 Yang, F. S. and Hong, B. The theory and application of Individual Component Analysis, *Tsinghua University Press*, (2006).
- 4 Hyvärinen, A., Karhunen, J. and Oja, E. Independent component analysis, John Wiley & Sons, Inc, (2001).
- 5 Puntonet, C. G., Górriz, J. M. and Moisés, S. et al. Theoretical Method for Solving BSS-ICA Using SVM, *Fifth International Conference, ICA 2004*, Granada, Spain, (2004).
- 6 Rojas, F., Puntonet, C. G. and Álvarez, M. R. et al. Evolutionary Algorithm Using Mutual Information for Independent Component Analysis, *7th International Work-Conference on Artificial and Natural Neural Networks*, Maó, Menorca, Spain, (2003).
- 7 Vosough, M. Using mean field approach independent component analysis to fatty acid characterization with overlapped GCMS signals, *Analytica Chimica Acta*, **598**, 219–226, (2007).
- 8 Liu, C. C., Sun, T. Y. and Hsieh, S. T. et al. A Hybrid Blind Signal Separation Algorithm: Particle Swarm Optimization on Feed-Forward Neural Network, *International Conference on Neural Information Processing*, Hong Kong, China, (2006).
- 9 Górriz, J. M., Puntonet, C. G. and Morales, J. D. et al. Simulated Annealing Based-GA Using Injective Contrast Functions for BSS, *Proceedings of the 5th International Conference on Computational Science*, Atlanta, GA, USA, (2005).
- 10 Zhang, W. A., Liu, J. H. Blind Source Separation Based on Particle Swarm Optimization, *Journal of Taiyuan University of Technology*, **37**(2), 169–172, (2006).
- 11 Sathyapriya, N., Balaji, N. and Lokesh, T. L. et al. Blind Source Separation Using Improved PSO For Adaptive Adjustment Of Learning Rate, *Conference Proceedings RTCSP'09*, (2009).
- 12 Li, M., Li, W. J., and Wang, Y. et al. Blind Source Separation Based on Improved Particle Swarm Optimization, *Artificial Intelligence and Computational Intelligence*, Shanghai, China, (2009).
- 13 Yin, H.J., Hussain, I. ICA and Genetic Algorithms for Blind Signal and Image Deconvolution and Deblurring, *Intelligent Data Engineering and Automated Learning 2006*, Burgos, Spain, (2006).
- 14 Kennedy, J. and Eberhart, R. Particle swarm optimization, *Proc IEEE International Conference on Neural Networks*, Nagoya, (1995).
- 15 Paul, R. C., Asokan, P. and Prabhakar, V. I. A solution to the facility layout problem having passages and inner structure walls using particle swarm optimization, *Int J Adv Manuf Technol*, **29**, 766–771, (2006).
- 16 Lin, S.W., Chen, S.C. and Wu, W. J. et al. Parameter determination and feature selection for back-propagation network, *Knowl Inf Syst*, **21**, 249–266, (2009).
- 17 Gao, Y., Li, Z. H. and Zheng, H. et al. Extended Particle Swarm Optimiser with Adaptive Acceleration Coefficients and Its Application in Nonlinear Blind Source Separation, *International Conference on Neural Information Processing*, Hong Kong, China, (2006).
- 18 Fernandez-Martinez, J.L. and Garcia-Gonzalo, E. Stochastic Stability Analysis of the Linear Continuous and Discrete PSO Models, *IEEE Transactions on Evolutionary Computation*, **15**(3), 405–423, (2011).
- 19 Song, K., Ding, M. L. and Wang, Q. et al. Blind Source Separation in Post-nonlinear Mixtures Using Natural Gradient Descent and Particle Swarm Optimization Algorithm, *4th International Symposium on Neural Networks*, Nanjing, China, (2007).
- 20 Haupt, R. L. and Haupt, S. E. Practical Genetic Algorithms, John Wiley & Sons, Inc., Hoboken, New Jersey, (2004). Second edition.
- 21 Theodoridis, S. and Koutroumbas, K. Pattern Recognition, China Machine Press, Beijing, (2006). Third edition.

Boundary Condition Identification of a Plate on Elastic Support

Hamid Ahmadian and Morteza Esfandiar

Center of Excellence in Experimental Solid Mechanics and Dynamics, Iran University of Science and Technology, Narmak, Tehran 16848, Iran

Hassan Jalali

Department of Mechanical Engineering, Arak University of Technology, Arak 38135-1177, Iran

(Received 29 December 2012; revised 27 March 2013; accepted: 26 February 2014)

The behaviour of mechanical structures in low frequencies is strongly affected by the existence of the boundary conditions. It is not usually possible to provide ideal boundary conditions, i.e. simply supported or clamped, for structures. Therefore the real structures are mostly constrained by elastic supports. Constructing an accurate mathematical or numerical model for a structure requires the knowledge of the support parameters. In this paper, a new method is proposed for the parameter identification of a rectangular plate constrained by elastic support. The method relies on the free vibration solution of the plate dynamics subjected to elastic boundary conditions and employs the optimization toolbox of MATLAB.

1. INTRODUCTION

The supports, or boundary conditions, play an important role in a structure's dynamic behaviour and must be considered carefully when constructing mathematical or numerical models. In reality, the supports of structures are not rigid enough, and they show flexibility to some degree. The flexibility of the supports can be modelled as elastic boundary conditions. In order to have an accurate model of a structure, the knowledge of the support parameters is essential. The support parameters can be identified by using experimental results.

The sensitivity method is one of the most widely used approaches in determining boundary condition parameters.¹ In this method the difference between model predictions and test observations is defined as an objective function. An iterative process is then adopted, and the objective function is minimized by using the sensitivity approach. It should be noted that the sensitivity of higher natural frequencies to support parameters is low, which results in convergence problems in the optimization procedure.²

In the characteristic equation method the boundary support parameters are identified by solving the nonlinear characteristic equations. In this method, which was adopted by Ahmadian et al., the number of characteristic equations formed is equal to the number of measured natural frequencies. The boundary condition parameters are then identified by simultaneously solving the characteristic equations.³

Waters et al. and Wang and Yang adopted the static flexibility measurements and identified the boundary conditions of a tapered beam.^{4,5} They modelled the beam as a uniform rigid beam that was constrained by collocated equivalent trans-

lational and rotational springs. The boundary conditions are identified by quasi-static stiffness measurements obtained from impact tests.

This paper deals with the support parameter identification of a rectangular plate constrained in its edges by an elastic boundary condition. The boundary condition contains structural damping. The solution method proposed by Li et al. is adopted to analyse the free vibration of the beam.⁶ The analysis leads to obtaining the natural frequencies and damping ratios of the plate. An identification approach is proposed based on the solution presented by Li et al. and by using the measured modal properties (i.e. natural frequencies and damping ratios).⁶ The proposed method is verified by using simulated and experimental results. The next section considers the free vibration analysis of an elastically supported plate.

2. PLATE DYNAMICS ON ELASTIC SUPPORT⁶

Figure 1 shows an elastically supported rectangular plate, which is constrained by lateral and torsional springs. It is considered that the elastic boundary condition contains structural damping.

The governing differential equation for the free vibration of the rectangular plate is expressed in Eq. (1):

$$D\nabla^4 w(x, y) - \rho h \omega^2 w(x, y) = 0; \quad (1)$$

where $\nabla^4 = \partial^4/\partial x^4 + 2\partial^4/\partial x^2\partial y^2 + \partial^4/\partial y^4$, and $w(x, y)$ is the lateral displacement function, ω is the angular frequency and ρ , h and D are mass density, thickness, and bending rigidity of the plate, respectively. The above governing equation is

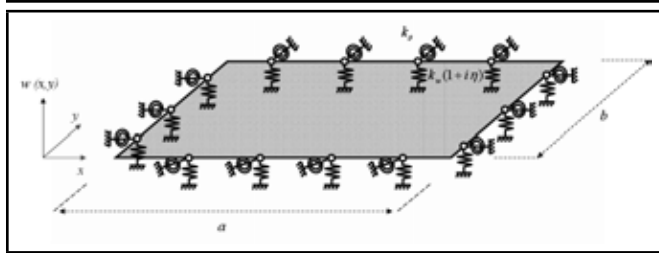


Figure 1. Rectangular plate with elastic boundary condition in all edges

subjected to the following boundary conditions, at $x = 0$ and $x = a$:

$$\bar{k}_w w(x, y) = -D(w_{xxx} + (2 - \nu)w_{xyy}); \quad (2)$$

$$k_\theta w_x = (-1)^{x/a} D(w_{xx} + \nu w_{yy}); \quad (3)$$

at $y = 0$ and $y = b$:

$$\bar{k}_w w(x, y) = -D(w_{yyy} + (2 - \nu)w_{yxx}); \quad (4)$$

$$k_\theta w_y = (-1)^{y/b} D(w_{yy} + \nu w_{xx}); \quad (5)$$

where $k_w = k_w(1 + i\eta)$. k_w and k_θ are respectively the lateral and torsional stiffness coefficients of the boundary condition and η is the structural damping coefficient. The above boundary conditions represent the shear forces and bending moments introduced at the plate edges by its movements. By considering a displacement field for the free vibration of the plate, substituting it into the governing equation and boundary condition relations, i.e. Eqs. (1)-(5), the resulting equation can be expressed as:⁶

$$\left([K] - \frac{\rho h \omega^2}{D} [M] \right) \{a\} = 0. \quad (6)$$

Equation (6) can be used for obtaining the natural frequencies of an elastically supported rectangular plate, provided that the parameters of the elastic boundary condition are known. The natural frequencies are calculated by solving the characteristic equation, i.e. $[K - (\rho h \omega^2 / D)M] = 0$. Since k_w is complex the calculated natural frequencies are a complex conjugate and of the form $\omega_n = -\zeta_n \omega_n \pm i \omega_n$, $n = 1, 2, \dots$. The real part represents the damping ratio, and the imaginary part is a measure of the free oscillation frequency of each mode.

Equation (6) can also be effectively used for parameter identification of the plate boundary support when the natural frequencies and damping ratios are known from experimental or simulated results. The parameter identification method is discussed in the next section.

3. PARAMETER IDENTIFICATION METHOD

Consider that N natural frequencies and damping ratios of an elastically restrained plate are known,

$$\{\Omega_e\} = [\bar{\omega}_1^e \bar{\omega}_2^e \dots \bar{\omega}_N^e]^T; \quad (7)$$

$$\{Z_e\} = [\zeta_1^e \zeta_2^e \dots \zeta_N^e]^T; \quad (8)$$

where $\{\Omega_e\}$ and $\{Z_e\}$ are the vectors of measured or simulated natural frequencies and damping ratios, respectively. The aim of this section is to identify the support parameters, i.e. k_w , k_θ and η by using the known vectors of modal properties introduced in Eq. (7) and Eq.(8). The support parameters are estimated by minimizing the differences between known and predicted modal characteristics as is described in the following. The predicted modal parameters are calculated by using the numerical method presented in the previous section.

In order to start the optimization algorithm, first a set of initial values for the support parameters are considered, i.e. k_w^0 , k_θ^0 and η^0 . The initial values are updated in subsequent iterations until the optimum support parameters are obtained. By substituting the initial parameters into Eq. (6) and solving the characteristic equation a set of predicted natural frequencies and damping ratios are obtained,

$$\{\Omega_a\} = [\bar{\omega}_1^a \bar{\omega}_2^a \dots \bar{\omega}_N^a]^T; \quad (9)$$

$$\{Z_a\} = [\zeta_1^a \zeta_2^a \dots \zeta_N^a]^T; \quad (10)$$

where $\{\Omega_a\}$ and $\{Z_a\}$ are the vectors of the predicted natural frequencies and damping ratios, respectively. The optimum set of the support parameters can be obtained by minimizing the following objective function:

$$OBJ = \|1 - \frac{\{\Omega_a\}}{\{\Omega_e\}}\| + \|1 - \frac{\{Z_a\}}{\{Z_e\}}\| \quad (11)$$

In Eq. (11) OBJ represents the sum of the norm of the differences between the known and predicted natural frequencies and damping ratios. Different optimization algorithms can be used to minimize the objective function of Eq. (11) and hence estimate the optimum support parameters. In sensitivity based approaches, the optimization problem in each iteration is cast in the following first order sensitivity equation: $[S]\{\Delta\} = \{\varepsilon\}$. Here, $[S]$ is the sensitivity matrix, $\{\Delta\} = [\delta k_w, \delta k_\theta, \delta \eta]^T$ is the vector of updating parameters and $\{\varepsilon\}$ is the vector of differences between the known and predicted modal parameters. By solving for $\{\Delta\}$, the updated support parameters in iteration i^{th} are obtained as,

$$k_w^i = k_w^{i-1} + \delta k_w; \quad (12)$$

$$k_\theta^i = k_\theta^{i-1} + \delta k_\theta; \quad (13)$$

$$\eta^i = \eta^{i-1} + \delta \eta. \quad (14)$$

Parameter updating based on equations (12)-(14) is terminated when $\|\varepsilon\|$ reaches a small value, i.e. $\|\varepsilon\| \ll 1$. $[S]$ is a matrix compose of the sensitivity of different modal parameters to the support parameters. Since the sensitivity matrix is not known for the problem considered in this paper, identification is performed by using gradient based methods in the optimization toolbox of MATLAB, e.g *fmincon*, *fminsearch*, \dots . In the following section a numerical example is presented to show the accuracy of the proposed method.

Table 1. Mechanical properties of the square plate

ν	$E(\text{Gpa})$	$\rho (\frac{\text{kg}}{\text{m}^3})$
0.33	200	7800

Table 2. Simulated natural frequencies and damping ratios.

Mode number	$\omega(\text{Hz})$	$\zeta(\%)$
1	115.41	2.04
2	135.43	1.97
3	166.77	1.92
4	217.41	1.71
5	219.97	1.60

4. NUMERICAL EXAMPLE

A square plate of dimensions $a = b = 2 \text{ m}$ and $h = 0.0025 \text{ m}$ is considered which is supported by an elastic boundary condition. The parameters of the boundary condition are considered as $k_w = 1000 \frac{\text{N}}{\text{m}}$, $k_\theta = 100 \frac{\text{Nm}}{\text{rad}}$ and $\eta = 0.0005$. The material properties of the plate are given in Table 1,

Having the plate dimensions, its material properties, and the boundary support parameters, the natural frequencies and damping ratios can be calculated by using Eq. (6). Table 2 shows five natural frequencies of the plate and their corresponding damping ratios:

Next, the modal properties presented in Table 2 are considered as experimental results, and the parameters of the boundary condition are identified by minimizing the objective function defined in Eq. (11). Minimization is done by using the Optimization Toolbox of MATLAB. Since the objective function is a nonlinear and complex function, the employed optimization algorithm strongly affects the identified results. The efficiency of different optimization algorithms was studied, and finally it was concluded that the *fmincon* function is the most appropriate function for the minimization of the objective function defined in this paper. In Table 3 the elapsed time and the final value of the objective function for different unconstraint (i.e. *fminsearch* and *fminunc*) and constraint (i.e. *fmincon* and *patternsearch*) optimization algorithms are compared. In obtaining the results presented in Table 3 the initial values shown in Table 4 for support parameters were used. Also, in constraint optimization algorithms, it was considered that the support parameters are positive, i.e. $k_w > 0$, $k_\theta > 0$ and $\eta > 0$.

Results presented in Table 3 indicate that the *fmincon* algorithm is more effective in obtaining the plate support parameters. In Fig. 2 the change in the objective function and, in Table 4, the initial and final support parameters are presented for the *fmincon* algorithm.

Figure 2 shows that the identification algorithm succeeds in finding the optimum support parameters after 40 iterations. The results presented in Fig. 2 and Table 4 indicates that the proposed method identifies the support parameters with an acceptable accuracy. The next section considers two experimental case studies.

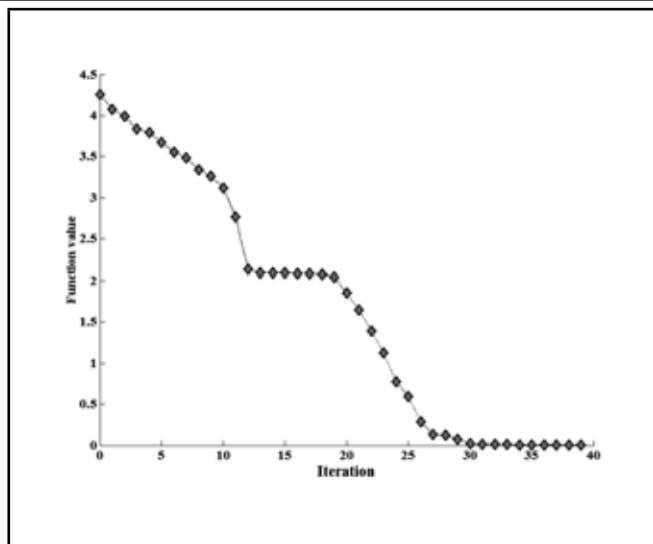


Figure 2. Change in objective function.

Table 4. Initial and identified support parameters.

	$k_w (\frac{\text{N}}{\text{m}})$	$k_\theta (\frac{\text{Nm}}{\text{rad}})$	η
Initial	0.1	0.0001	0
<i>Numerical example</i>			
Identified	1000.18945	97.0673	0.00049925
<i>Aluminum plate</i>			
Identified	65.104	0.126	0.00028
<i>Steel plate</i>			
Identified	3194.161	850.725	0.01849

5. EXPERIMENTAL VALIDATION

In this section, the proposed method is applied to two experimental case studies, and the parameters of their boundary conditions are identified.

5.1. Aluminium rectangular plate

In this section the experimental results of a rectangular aluminium plate considered by Amabili is used, and its boundary support parameters are identified.⁷ The material properties and geometrical dimensions of the aluminium plate are presented in Table 5.

The plate was placed between rectangular frames made of thick steel. The frame prevents the edges of the plate to move in a perpendicular direction, but they can rotate. Therefore the boundary condition was very similar to the simply supported boundary condition. It should be noted that the identified lateral stiffness coefficient should be much larger than the identified torsional stiffness coefficient. Modal testing was performed on the plate, and its natural frequencies and damping ratios were extracted. The plate was excited by means of an electromagnetic shaker, model LDS V406. The transmit-

Table 5. Dimensions and mechanical properties of the aluminum plate.⁷

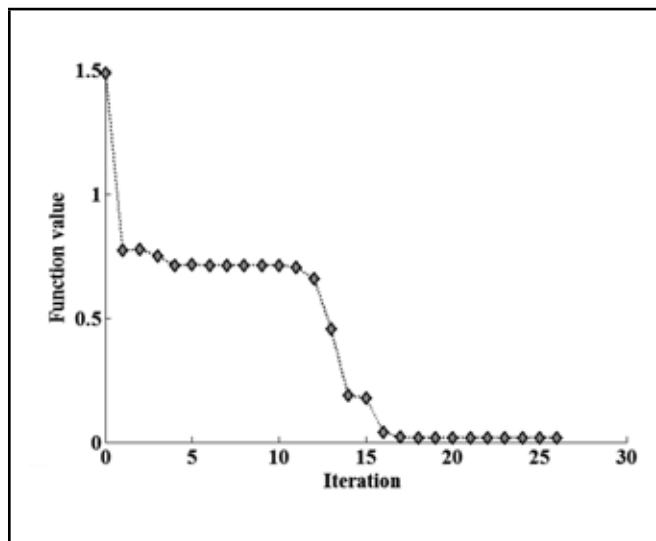
ν	$E(\text{Gpa})$	$\rho (\frac{\text{kg}}{\text{m}^3})$	$h(\text{m})$	$b(\text{m})$	$a(\text{m})$
0.33	69.10	2700	0.0003	0.184	0.515

Table 3. The efficiency of different optimization algorithms.

	<i>fminsearch</i>	<i>fminunc</i>	<i>fmincon</i>	<i>patternsearch</i>
elapsed time (s)	12423.50	736.33	450.73	18663.19
final objective function	2.08×10^{-9}	27.304	2.93×10^{-18}	1.53×10^{-8}

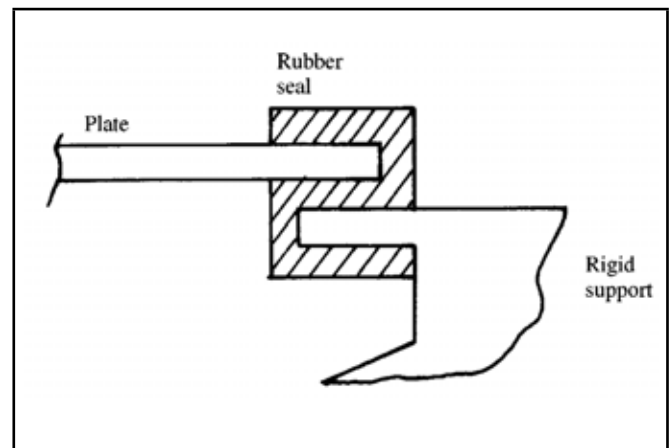
Table 6. Comparison of experimental and predicted modal properties (aluminum plate).

Mode number	Natural frequency ω (Hz)			Damping ratio ζ (%)		
	Exp.	Predicted	Error (%)	Exp.	Predicted	Error (%)
1	26.87	26.99	-0.47	2.06	2.06	0.0
2	39.37	38.97	1.01	1.51	1.50	0.54
3	55.20	55.60	-0.74	1.88	1.90	-1.13
4	75.72	74.32	1.84	1.34	1.31	2.04
5	93.56	95.10	-1.65	1.12	1.13	-1.72

**Figure 3.** Variation of the objective function (aluminium plate).

ted value was measured by using a piezoelectric force transducer, model PCB M209C11, placed between the stinger and the plate. An accelerometer, model Endevco 22, was glued to the centre of the plate in order to measure the plate response. A low level burst-random excitation force was employed, and the plate frequency response functions (FRFs) were measured. The plate modal characteristics were extracted by analysing the experimental FRFs. The experimental results are presented in Table 6:

The measured modal properties presented in Table (6) are used, and the parameters of the plate boundary support are identified. Identification is done by following the procedure presented in previous sections. It is worth mentioning that only three first natural frequencies are used in the identification procedure. The remaining two natural frequencies are used for the verification of the identified parameters. The variation of the objective function in the identification procedure is shown in Fig. 3. The initial and identified support parameters are tabulated in Table 4. In Table 6 experimental and identified modal properties are compared. The results presented in Table 6 show the accuracy of the proposed method.

**Figure 4.** The steel plate supported by rubber seal.

5.2. Steel plate supported by rubber seal

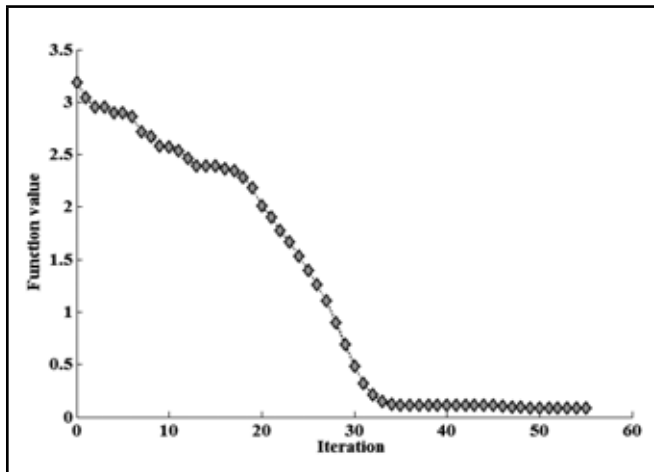
In this section, the boundary condition of the steel plate considered by Ahmadian et. al. is identified.³ The plate, having the dimensions of $0.5 \text{ m} \times 0.8 \text{ m} \times 0.0025 \text{ m}$, is attached to the ground by the rubber seal. A schematic of the elastic supported plate is depicted in Fig. 4. The plate has the following material properties: $\nu = 0.33$ as Poisson's ratio, $E = 207 \text{ GPa}$ as Young's modulus, and $\rho = 7800 \frac{\text{kg}}{\text{m}^3}$ as mass density.

Modal testing was performed on the plate in order to measure its dynamic properties, i.e. natural frequencies and damping ratios. The plate was excited by using a modal hammer, and its response was measured by means of accelerometers. By transferring the recorded force and response signals into a digital analyser, the frequency response functions (FRFs) were calculated. FRFs were then curve fitted, and the modal parameters of the steel plate were extracted. The experimental natural frequencies and damping ratios are given in Table 7. As in the aluminium plate case, the elastic support parameters are identified by employing the method presented in this paper and by using the first three measured natural frequencies and damping ratios. The variation of the objective function in the identification procedure is shown in Fig. 5. Table 4 reports the identified support parameters for the steel plate.

The experimental and predicted modal properties are compared in Table 7. It is worth mentioning that the last two sets of

Table 7. Comparison of the experimental and predicted modal properties.

Mode number	Natural frequency ω (Hz)			Damping ratio ζ (%)		
	Exp.	Predicted	Error (%)	Exp.	Predicted	Error (%)
1	29.60	29.89	-1.00	1.58	1.57	0.32
2	60.40	59.93	0.77	0.84	0.85	-1.23
3	98.90	97.80	1.11	0.91	0.92	-1.56
4	106.20	104.50	1.53	0.87	0.85	1.43
5	120.10	122.90	-2.41	1.36	1.39	-2.72

**Figure 5.** Variation of the objective function in identification procedure (steel plate).

modal characteristics are used for verification of the identified model. The results presented in Table 7 show the accuracy of the identified support model for the steel plate.

6. CONCLUSION

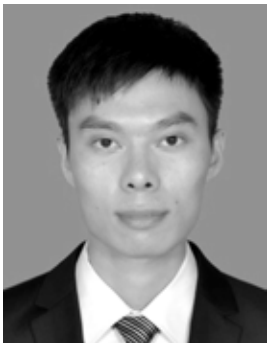
Identification of the boundary condition parameters of a rectangular plate restrained in edges by an elastic support was considered. The boundary support was considered to contain structural damping. In order to identify the support parameters, first a numerical solution developed in⁶ was presented for free vibration of elastic supported plate. The solution permitted the calculation of the plate's natural frequencies and damping ratios. The support parameters were identified by minimizing the differences between experimental and predicted modal properties by employing the MATLAB optimization toolbox. The identification procedure was verified by using simulated and experimental results presented by Amabili⁷ and Ahmadian et al.³

REFERENCES

- ¹ Gandhi, R. Structural optimization with frequency constraint-a review, *American Institute of Aeronautics and Astronautics Journal*, **31**, 2296–3203, (1993).
- ² Courant R., and Hilbert D. *Methods of Mathematical Physics*. New York: Interscience Publishers Inc (1953).
- ³ Ahmadian H., Mottershead J. E., and Friswell M. I. Boundary condition identification by solving characteristic equations, *Journal of Sound and Vibration*, **247**, 755–763, (2001).
- ⁴ Waters T. P., Brennan M. J., and Sasananan S. Identifying the foundation stiffness of a partially embedded post from vibration measurements, *Journal of Sound and Vibration*, **274**, 137–161, (2004).
- ⁵ Wang L., and Yang Z. Identification of boundary conditions of tapered beam-like Structures using static flexibility measurements, *Mechanical Systems and Signal Processing*, **25**, 2484–2500, (2011).
- ⁶ Li W. L., Zhang X., Du J., and Liu Z. An exact series solution for the transverse vibration of rectangular plates with general elastic boundary supports, *Journal of Sound and Vibration*, **321**, 254–269, (2009).
- ⁷ Amabili M. Nonlinear vibrations of rectangular plates with different boundary conditions: theory and experiments, *Journal of Computers and Structures*, **24**, 2587–2605.

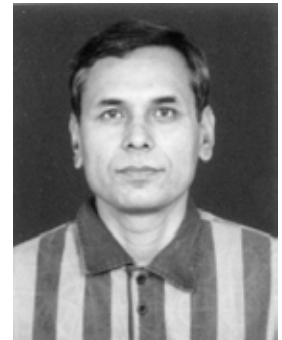
Zhi-cheng Qiu is a professor at South China University of Technology (SCUT). He received his BA in mechanical design and manufacturing and his master's degree in fluid power transmission and control from Harbin Institute of Technology, Harbin, in 1995 and 1997, respectively. In 2000, he received his engineering PhD in mechatronic engineering from the Shenyang Institute of Automation, Chinese Academy of Sciences. Afterwards, he did post-doctoral research in control theory and control engineering at the Beijing Institute of Control Engineering, Beijing.

He has been employed by South China University of Technology since 2003 and is engaged in teaching and scientific research work. He was named associate professor in 2004, professor in 2009, and he was authorized as a doctoral supervisor in 2010. His current research field is active vibration control of flexible structures and flexible robots control.



Biao Ma received his BA degree in mechanical design manufacturing and automation from Shandong University of Technology, Zibo, in 2011. He is now a master's degree candidate in mechatronic engineering at the South China University of Technology, Guangzhou. His current research interests include finite element modeling and flutter and vibration active control of piezoelectric flexible structures.

Gokarna Bahadur Motra received both his BS and MS degrees in civil engineering from Yerevan Architectural Engineering Institute in Armenia. He received his PhD in civil engineering from IIT Bombay. He is a reader in Civil Engineering at the Institute of Engineering, Pulchowk Campus, Tribhuvan University, Nepal. His PhD is in optimal control of seismically excited buildings connected by magnetorheological dampers. His current research includes vibration control of structures using passive/semi-active devices and seismic resistant design of structures. He teaches undergraduate and graduate courses in structural engineering.



Naresh K. Chandiramani received his BT. in civil engineering from IIT Delhi and his MS and PhD degrees in engineering mechanics from Virginia Tech. He is a professor of civil engineering at the Indian Institute of Technology Bombay. His current research is on active control of structures using MR dampers and variable stiffness devices for framed structures, piezoelectric sensing/actuation for rotating thin-walled composite blades, and shunted piezoelectrics. His previous work includes nonlinear dynamics of self-excited systems involving aerodynamic flutter, tool chatter, and also friction damped systems. He teaches undergraduate and graduate courses in structural engineering and applied mechanics.

About the Authors



Nowrouz M. Nouri is currently an associate professor of mechanical engineering at the Iran University of Science and Technology (IUST). He was educated in mechanical engineering and graduated from the University of Zahedan with an emphasis in fluid mechanics. He later continued his graduate studies in cole Polytechnique in France where he received his PhD working on vortex phenomena in 1993. Dr. Nouri has completed many industrial and scientific projects and has served as department chair and associate dean at IUST.

Ali Valipour is a PhD candidate at the School of Mechanical Engineering at Iran University of Science and Technology (IUST). Ali received his BS degree from Azad University of Ahwaz back in 2005 and his MS degree in mechanical engineering from IUST. His research activities include acoustics, finite element simulation, offshore structures, nondestructive testing, and noise measurement.



Mohammad Riahi is currently an associate professor of mechanical engineering at the Iran University of Science and Technology (IUST). He has served as department chair and associate dean for research. Mohammad received his BS (1981) and MS (1986) in mechanics in Illinois, USA and he received his PhD in manufacturing in Iowa, USA (1991). Dr. Riahi's research activities include nondestructive testing, acoustics and acoustic emission, and measurements and condition monitoring in industrial maintenance.

Ricardo Oscar Grossi was born in Bahía Blanca, Argentina. He received a degree in electrical engineering from Universidad Tecnológica Nacional in 1973. He received his PhD in engineering from Universidad Nacional del Sur in Argentina in 1985. He currently teaches applied mathematics, and he primarily studies the vibrations of structural elements.



Javier Leandro Raffo was born in Buenos Aires, Argentina. In 2000, he received a degree in aeronautic engineering from Universidad Nacional de La Plata in Buenos Aires, Argentina. He is an associate professor in the Department of Mechanical Engineering at the Universidad Tecnologica Nacional, Facultad Regional Delta in Campana, Buenos Aires, Argentina, where he directs the Computational Mechanics and Experimental Mechanics Lab. He is finishing his doctoral degree in engineering and mathematical sciences at Universidad Nacional de Salta, Argentina. His current research focuses on applied mathematics, computational mechanics, and experimental mechanics. His principal activity is the study of vibrations of cracked structural elements.



V. Vijayan earned his BE in mechanical engineering at Madurai Kamaraj University, Madurai in 2004 and his ME in engineering design at Anna University, Chennai, Tamil Nadu, India in 2006. He has nine years of teaching and administrative experience, and he is currently working as assistant professor in the Mechanical Engineering Department at K.Ramakrishnan College of Engineering, Trichy, Tamilnadu, India. He has published seven international and four national journals/conference proceedings in the area of compliant mechanism. He is presently doing research in design compliant mechanism for passive vibration isolation. Mr. Vijayan is a lifetime member of the Indian Society for Technical Education (ISTE).

T. Karthikeyan completed his BE in mechanical engineering at Bharadidhasan University, Trichy in 1989, and he received his ME in manufacturing technology at Regional Engineering College, Trichy, India in 1995. He earned his PhD at National Institute of Technology (formerly Regional Engineering College), Trichy in 2005. He is currently working as principal at Arulmurugan College of Engineering in Karur, Tamil Nadu, India. He has published 15 international and 23 national journals/conference proceedings in the area of flexible manufacturing systems. He is currently working with the scheduling of FMS and the reliability study of manufacturing systems. Dr. Karthikeyan is a fellow member of the Institution of Engineers India and a lifetime member of the Indian Society for Technical Education (ISTE). He is also a lifetime member of the Indian Institution of Production Engineers (IIPE). He has 20 years of teaching and administrative experience. He is also the organizer of a number of programmes associated with funding agencies for the betterment of the student and teaching community.



M. Udayakumar completed his BE in mechanical engineering at Anna University, Chennai, Tamil Nadu, India in 2010. He received his ME in engineering design at Anna University, Chennai, Tamil Nadu, India in 2012. He has seven years of teaching and administrative experience. He currently works as assistant professor in the Mechanical Engineering Department at K.Ramakrishnan College of Engineering, Trichy, Tamilnadu, India. He has published three international and two national journals/conference proceedings in the area of composite materials and vibration analysis. Mr. M. Udayakumar is a board member of the International Journal of Engineering Trends and Technology (IJETT).

About the Authors

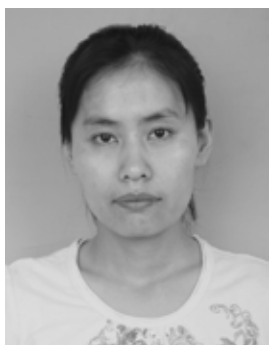


K. Chellamuthu completed his BE in mechanical engineering at Anna University, Chennai, Tamil Nadu, India in 2009, and his ME in CAD / CAM at Anna University of Technology, Tirunelveli, Tamil Nadu, India in 2011. He has three years of teaching and administrative experience, and he currently works as assistant professor in the Mechanical Engineering Department at K.Ramakrishnan College of Engineering, Trichy, Tamilnadu, India.

He has published one international and four national journals/conference proceedings in the area of composite materials and design analysis.

Mr. K. Chellamuthu is a lifetime member of Indian Society for Technical Education (ISTE).

Yang Yang received her bachelor's degree in electronic information science and technology and her master's degree in circuits and systems from Northeast Normal University, Changchun, Jilin Province, China, in 2006 and 2009, respectively. After graduation, she has worked in the Department of Electronic Information and the College of Engineering, Bohai University, Jinzhou, Liaoning Province, China. Since September 2012, she has been a lecturer with the College of Engineering. She has published more than 10 papers in international journals and conferences about signal processing and related fields. Her current research interests include acoustical and speech signal processing, blind source separation, artificial intelligence, and pattern recognition.



Xiuqin Wang received her bachelor's degree in computer science and technology, from Qufu Normal University, Qufu, Shandong Province, China, in 2002 and her master's degree in computer software and theory in 2005. She received her PhD in computer application technology from Harbin Engineering University, Harbin, Heilongjiang Province, China, in 2009. She is currently a lecturer with the Department of Computers, College of Information Science and Technology, Bohai University, Jinzhou, Liaoning Province, China. She is also a member of the China Computer Federation (CCF) in China. Her current research interests include VLSI design automation technology, artificial intelligence, signal processing, and EDA algorithms.

Di Zhang received his double bachelor's degree in mechanical design manufacturing and automation and thermal power plant power engineering from Northeast Dianli University (NEDU), JinlinJilin Province, China, in 2007. After graduation, he has worked in the Liaoning Datang international Jinzhou power generation Co.,Ltd, Jinzhou, Liaoning Province, China. He is currently an engineer with the Department of Electricity Generation and is responsible for one operating team. He is the author or a coauthor of nearly 10 papers in journals and conference proceedings both at home and abroad. His current research interests include signal processing, data analysis in thermal power plants, and data mining.



Hamid Ahmadian received his BS, MS, and PhD degrees in mechanical engineering from Iran University of Science and Technology in 1986, Amirkabir University of Technology in 1988, and the University of Waterloo in 1994, respectively. He worked as a research associate from 1994 to 1996 in the faculty of Engineering at Liverpool University. Hamid joined Iran University of Science and Technology in late 1996 as an assistant professor in mechanical engineering. He was promoted to associate professor in 2001 and professor in 2007. He has successfully supervised over 40 PhD and MS theses and published over 70 papers in refereed journals. His research interests include inverse eigenvalue problems, nonlinear structural dynamics, rotating machinery, and machine tool dynamics. Prof. Ahmadian is a senior member of the ISAV.



Hassan Jalali is an assistant professor at Arak University of Technology. He received his PhD degree from Iran University of Science and Technology in 2007. His main area of research is in the modelling and identification of nonlinear mechanical systems with a focus on mechanical joints and interfaces.



Mostafa Esfandiar obtained his BS degree in mechanical engineering from Shahid Bahonar University in 2006 and his MS degree from IUST in 2008. He has experiences in modal testing, FE model updating, and linear and nonlinear vibration of beams and plates.



Book Reviews

Waves and Structures in Nonlinear Nondispersive Media

by S.N. Gurbatov, O.V. Rudenko & A. Saichev

Jointly published by Higher Education Press and Springer

2012, 500p. 175 illus., 5 illus. in colour, Hardcover

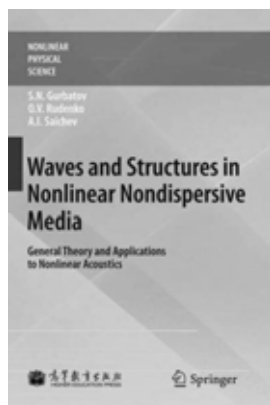
ISBN: 978-3-642-23616-7

Price: US \$219

The authors of this volume are well known for their work on nonlinear acoustics, and those who have read their earlier books will find that they have maintained similar standards of quality over an evolving range of topics.

As the subtitle “General Theory and Applications to Nonlinear Acoustics” indicates, the book is divided into two parts: theory and application. Part one concerns the general theory of nonlinear waves. This part not only illustrates hydrodynamic problems, but it also illustrates other applications that lead to similar or related equations such as the advances of a flame front in a forest fire and the gravitational collapse of an expanding universe. Part two applies similar methods to a number of problems in nonlinear acoustics.

A common feature of both parts one and two is the frequent reference to the Lagrangian coordinates co-moving with a particle or flow in addition to the Eulerian coordinates relative to a fixed reference frame. The use of Lagrangian-to-Eulerian coordinate transformations starts at the beginning of chapter one. This chapter deals with simple waves described by Riemann’s equation. Chapter two continues with a detailed analysis of the solutions to the nonlinear first-order wave equation of the Riemann type before proceeding to the second-order wave equations of Burgers and the related types in chapters three through five.



The Burgers’ equation is solved directly by applying the Cole-Hopf transformation to the heat equation in chapters three and four. These chapters include a variety of cases from N-waves to fractal signals. Burgers initially envisaged the equation named after him as the one-dimensional Navier-Stokes equation without the pressure gradient term as a model of turbulence. It has been used mostly to describe the coupling of inertial nonlinearity with diffusion, and it has been applied to nonlinear waves with linear damping. In chapter five, the Burgers’ equation is used as a model of turbulence by assuming a random initial velocity field and following its statistical evolution. Chapter six extends the theory to the multidimensional Burgers’ equation, completing part one on wave theory.

Part two focuses on the applications to nonlinear acoustics and consists of chapters seven to eleven. Chapter seven starts with general equations and their solutions, including both the Burgers’ equation and several extensions of this equation. Chapter eight concerns acoustic nonlinearities that are relevant to the ultrasonic methods of the inspection of materials. Chapter nine deals with N-waves that are best known for their role in the sonic booms of supersonic aircrafts. Chapter ten concerns the self-action of nonlinear waves, including the focusing and self-refraction of nonlinear beams, and acoustic streaming (the flow field induced by nonlinear waves). The final chapter, chapter eleven, addresses nonlinear resonant standing waves, including several classes of nonlinear media.

The book includes an appendix with some of the properties of the generalized functions (Heaviside unit step and Dirac unit impulse) that are used in the text. This volume is a useful addition to the literature on nonlinear waves and nonlinear acoustics as it provides a cohesive and clear account of some of the recent progress in the research of these areas.

L. M. B. C. Campos

Instituto Superior Tecnico